# Quantitative modelling of bacterial growth physiology, cell size and shape control

**By**

**Diana Maria Serbanescu**

*A thesis submitted to*

University College London

*for the degree of*

Doctor of Philosophy

Department of Physics and Astronomy

University College London

September 23, 2022

I, Diana Maria Serbanescu confirm that the work presented in this thesis is my own. Where information has been derived from other sources, I confirm that this has been indicated in the thesis.

Signed ..... Date .....

## Abstract

Bacteria are highly adaptive microorganisms that proliferate in a wide range of environmental conditions via changes in cell size, shape and molecular composition. How bacterial cell size, shapes and physiological properties are regulated in diverse environmental conditions are questions of longstanding interest. Regulation of cell size and shape imply cellular control mechanisms that couple bacterial growth and division processes to their cellular environment and molecular composition. Studies in the past decades have revealed many fundamental principles of bacterial growth physiology, in particular the relationship between cellular growth rate, proteome composition and the nutrient environment. However, the quantitative relations defining the interdependence of cell growth and morphology, together with the molecular mechanisms underlying the control of bacterial cell morphology remain poorly understood. In this thesis I develop quantitative theory and models for bacterial growth dynamics that link cellular proteome with cell size and division control (Chapter 2), cell shape control (Chapter 3), regulation of bacterial growth and morphology in the presence of antibiotic stress (Chapter 4), and energy allocation strategies for cellular growth and shape control (Chapter 5). My work reveals that cell size maintenance under nutrient perturbations requires a balanced trade-off between ribosomes and division protein synthesis. Deviations from this trade-off relationship are predicted under translation inhibition, leading to distinct modes of cell morphological changes, in agreement with single-cell data on *Escherichia coli* growth and cell morphology. Using the particular example of ribosome-targeting antibiotics, I present a systems-level model for the regulation of cell shape and growth physiology under antibiotic stress, and uncover various feedback mechanisms that bacteria can harness to increase their fitness in the presence of antibiotics.

# Impact Statement

Cell size maintenance is crucial for regulating bacterial growth physiology, cell function, and fitness. Maintaining a characteristic cell size requires a balance between the rates of cell growth and division. How this balance is regulated in different growth conditions has been an outstanding question in the field of bacterial physiology. In this thesis, I develop a whole-cell model for bacterial growth dynamics that connects cell size and division control in bacteria to the regulation of protein synthesis. My work reveals that cell size is controlled by a trade-off between the allocation of cellular resources toward ribosomal and division protein synthesis. This principle quantitatively determines bacterial cell morphology and growth rates under nutrient shifts or translational perturbations, resolving a long-standing question in the field.

Using the quantitative model developed in this thesis, I investigate the relationship between cell morphology, nutrient quality, and bacterial growth rate under antibiotic treatments. In particular, I predict that round cells are most resistant to translation-inhibitory antibiotics, and that drug resistance increases with increasing nutrient quality. By analyzing cell growth and morphological data of different bacterial model organism under antibiotic stress, I characterize the effect of antibiotics on bacterial growth and morphology to test and validate theoretical predictions. In particular, we propose a antibiotic resistance mechanism that bacteria employ to increase fitness by reducing the influx of antibiotics via changes in cell surface-to-volume ratio. Shape changes therefore make bacteria more adaptive to surviving antibiotics, suggesting that cell shape regulators may serve as potent targets for preventing antibiotic resistance.

The proposed morphological changes that promote bacterial fitness have major implications in healthcare, where a new mechanism of action can be employed to prevent bacterial growth and infections. We can identify new modes of antibiotic action by examining the shapes of the cells. The model I developed can be applied to various types of perturbations of bacterial physiology, such as osmotic shocks, mechanical stress, starvation, and antibiotics targeting the cell membrane and the cell-wall. The versatility of the model allows it to be used in antibacterial drug design to prevent bacterial growth but also in designing bacterial growth experiments due to its predictive power.

# List of Publications

1. N Ojkic, D Serbanescu, and S Banerjee, "Surface-to-volume scaling and aspect ratio preservation in rod-shaped bacteria". *eLife*, *8*, e47033 (2019).

2. D Serbanescu, N Ojkic, and S Banerjee, "Nutrient-dependent trade-offs between ribosomes and division protein synthesis control bacterial cell size and growth". *Cell Reports*, *32*(12), p.108183 (2020).

3. D Serbanescu, N Ojkic, and S Banerjee, "Cellular resource allocation strategies for cell size and shape control in bacteria". *The FEBS Journal*, doi:10.1111/febs.16234 (2021).

4. N Ojkic, D Serbanescu, and S Banerjee, "Antibiotic resistance via bacterial cell shape-shifting", *mBio*, doi:10.1128/mbio.00659-22 (2022).

5. D Serbanescu and S Banerjee, "Energy allocation theory for bacterial growth control and cell shape maintenance", *in preparation* (2022).

6. TW Ng, D Serbanescu, N Ojkic, and S Banerjee, "Differential cell growth maintains asymmetric division control in *Caulobacter Crescentus*", *in preparation* (2022).

# Acknowledgments

First and foremost, I would like to thank my supervisor, Shiladitya Banerjee who supported and guided me through the ups and downs of a PhD. Shila kept me on track with interesting projects and more importantly helped me become a better communicator, both in writing and in expressing ideas.

I must also thank Nikola Ojkic for his help with the shape analysis and simulations in Chapters 3 and 4. Working with Nikola and Shila has been a pleasure and they are the best team one can ask for. I would also like to thank the rest of the Banerjee group for their useful feedback and support and to Andela Saric for letting me take part in her group meetings and keeping me connected to the amazing people in her group.

I met wonderful people and made great friends during my studies at UCL. In particular I am grateful for having met Nikita who put up with me as a flatmate for four years and is the best friend one can ask for. I would also like to thank the "Cappuccino Express" group: Victoria, Tom, Pete, Carlo, you guys are amazing, and I have never felt more welcome in a group. Thank you to the chess squad: Ionut, Ferran, Lawrence, Stefan - you always make me laugh and your competitiveness keeps me motivated. Special thanks to Petra for always taking the time to listen to me and to Tibi for encouraging me to apply for a PhD in the first place and always believing in me. I am especially grateful to all the love and friendship Mike has offered me, making my life beautiful.

Finally, I would like to thank my parents who have supported me unconditionally from day one and who constantly try to understand what it is exactly I do. Their urge to continuously better themselves inspired me over the years and the respect and admiration I have for them make me want to be or at least try to be the best at anything I do.

# Contents

# List of Figures

# Chapter 1

# Introduction

Bacteria are highly adaptive microorganisms that thrive in a wide range of growth conditions via changes in cell morphologies and macromolecular composition. How bacterial cell size, shape and growth rates are regulated in diverse environmental conditions are longstanding questions. Cell morphology is a fundamental physiological trait that is crucial for cellular growth, nutrient uptake, and environmental adaptation. Bacterial cells need to maintain appropriate sizes to optimize their fitness and regulate cell physiology [35]. Regulation of cell size and shape implies cellular control mechanisms that couple growth and division to cellular environment and macromolecular composition. In the past decade, simple quantitative laws have emerged that connect cell growth to proteomic composition and the nutrient availability. However, the relationships between cell size, shape and growth physiology remain poorly understood and unifying models are lacking. The goal of this thesis is to develop regulatory models of cell size control that reveal the connections between bacterial cell size, shape and growth physiology. In this chapter, I review the existing literature on bacterial growth physiology, focusing on the literature models for bacterial growth control and cell size regulation. The timeline in

Part of this chapter is published in Serbanescu, D., Ojkic, N., & Banerjee, S. (2021). Cellular resource allocation strategies for cell size and shape control in bacteria. *The FEBS Journal*. [34]

Figure 1.1 is based on the main results discussed in this chapter and shows discoveries related to the physiology of bacteria.

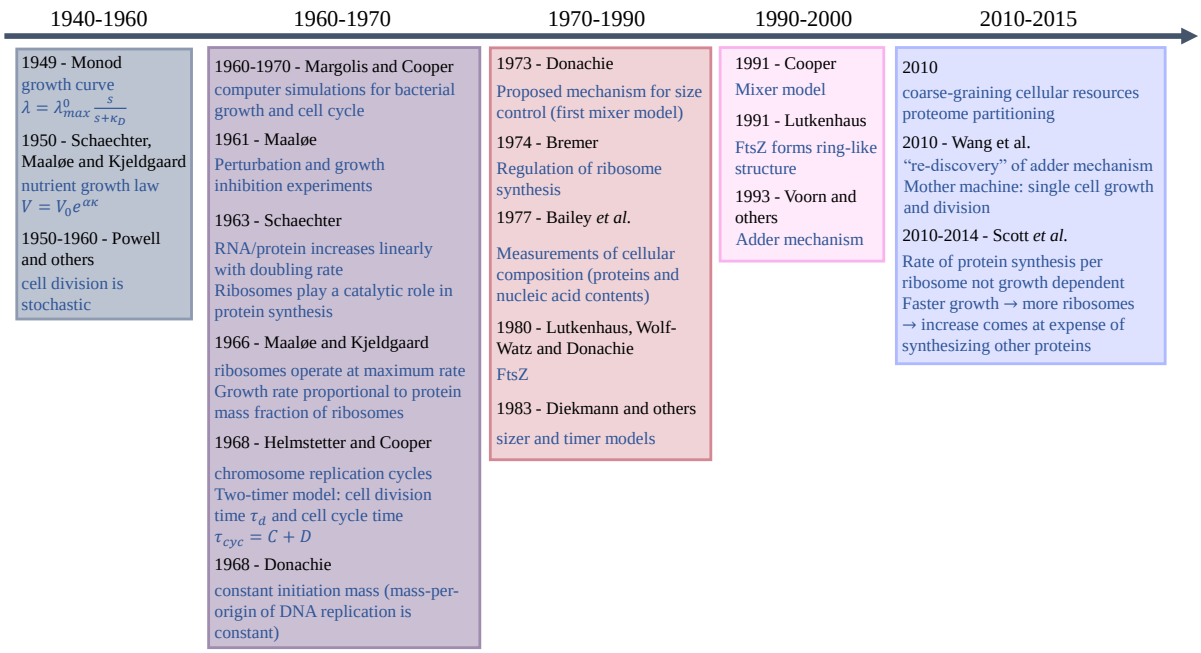


Figure 1.1: **Timeline showing the important discoveries in the field in the past sixty years [1].** The timeline was based on the main points discussed in Chapter 1.

## 1.1 Determinants of bacterial growth rate

The physiological state of a cell is characterized by its size, shape, macromolecular composition, and the rate of growth. Their interdependence is one of the key questions in bacterial growth physiology. The pioneering work of Monod in the 1940s on bacterial physiology revealed the dependence of cellular growth rate on the extracellular nutrient concentration. In his work [36], Monod observed that the growth rate of *Escherichia coli* cells increases with increasing glucose concentration up to a maximum and defined the empirical hyperbolic dependence as:

$$\kappa_{\text{specific}} = \kappa_0 \frac{[n]}{[n] + n^*} \tag{1.1}$$

where $\kappa_{\text{specific}}$ is the nutrient-specific growth rate, $[n]$ is the concentration of the nutrients, $n^*$ is the nutrient concentration at half-maximum growth rate, and $\kappa_0$ is the maximum growth rate that the bacteria can achieve in a given nutrient medium. When the concentration of nutrients inside the cells reaches maximum, the growth rate $\kappa$ of the bacteria becomes equal to $\kappa_{\text{specific}}$.

However, to understand how cells achieve a nutrient-specific growth rate, a mechanistic link has to be established between the rates of nutrient import, energy production, protein synthesis and cell envelope biogenesis. Protein synthesis is essential for bacteria to proliferate. At the core of protein synthesis is the ribosome machinery which synthesizes new proteins through the process of translation. In recent work [37], Belliveau *et al.* used proteomics data across a large number of growth conditions to examine the possible candidates that limit the growth rate of bacteria. It is found that bacterial cell growth is not limited by transporter expression for nutrient import, biosynthesis of cell envelope components, or by ATP synthesis. Instead, the translation machinery plays a crucial role, such that the synthesis of ribosomes is the rate limiting process for bacterial growth Figure 1.2 **A**.

## 1.2 Bacterial growth laws

In *E. coli* ribosomes contain approximately 85% of the RNA [3]. Therefore the ratio of RNA to protein mass can be approximated as the ribosome mass fraction $\phi_R$ in a cell. Earlier works by Neinhardt, Magasanik and Harvey [38, 39] uncovered a positive linear relationship between ribosome mass fraction and nutrient specific growth rate in moderate to fast growth conditions. Scott *et al.* [4] formalized this into a quantitative growth law of ribosome synthesis (Figure 1.2 **B** and Figure 1.4 **B** red shading) - *growth law under nutrient perturbations*:

$$\phi_R = \phi_R^{\min} + \frac{\kappa}{\kappa_t} \tag{1.2}$$

where $\phi_R^{\min}$ is the mass fraction of inactive ribosomes and $\kappa_t$ is the translational capacity, defined as the average rate for amino acid chain elongation per ribosomes. Eq. 1.2 is not

unique to bacterial cells as a linear scaling between the growth rate and ribosome mass fraction was also found in the eukaryotic buddying yeast and fission yeast [40, 41].

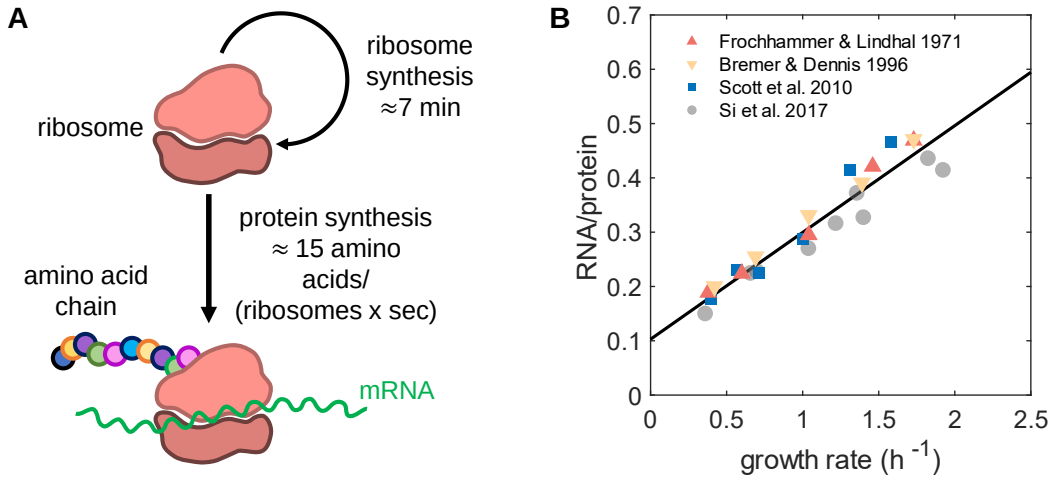


Figure 1.2: **Growth rate regulation in bacteria. A.** Schematic showing translation and ribosomal protein synthesis, which constitute the limiting factors for bacterial cell growth. **B.** Ribosomal mass fraction in *E. coli*, approximated by the ratio of RNA to protein mass, increases linearly with the growth rate of the cell modulated by nutrients. Data taken from refs. [2, 3, 4, 5].

When the growth rate is altered by inhibiting translation (e.g. by adding ribosome-targeting antibiotics), ribosome mass fraction decreases linearly with growth rate (Figure 1.4 **B** green shading - *growth law under translation inhibition* [4]:

$$\phi_R = \phi_R^{\max} - \frac{\kappa}{\kappa_n} , \tag{1.3}$$

where $\phi_R^{\max}$ is the maximum mass fraction of ribosomal proteins, and $\kappa_n$ is the nutritional capacity of the medium that has a positive correlation with the nutrient-specific growth rate. The observation that the maximum mass fraction of ribosomal proteins $\phi_R^{\max} \approx 0.55$ is much below 1, suggests a coarse-grained model of proteome partitioning into three components: ribosome-affiliated proteins (R-sector) of mass fraction $\phi_R$, housekeeping proteins (Q-sector) of mass fraction $\phi_Q$ that are not affected by translation inhibition,

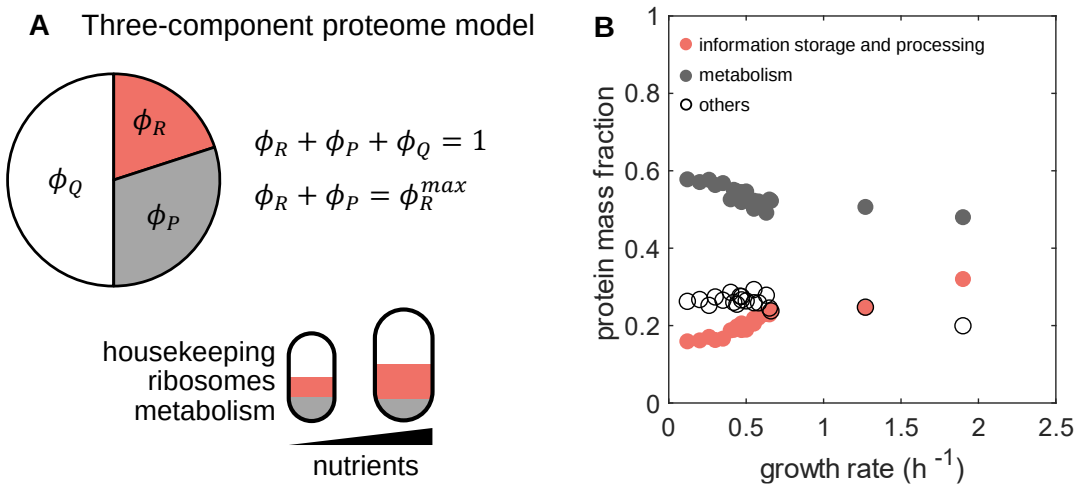


Figure 1.3: **Three component proteome model. A.** The three-component proteome partitioning model [4], consisting of the Q-sector that is invariant under translational perturbations, the R-sector of ribosomal proteins that increase in mass fraction with increasing growth rate, and the P-sector of non-ribosomal proteins that is constrained by the relation: $\phi_P + \phi_R = \phi_R^{\max} = 1 - \phi_Q \approx 0.55$. **B.** Proteomic data [6] show a decrease in the mass fraction of metabolic sector proteins with growth rate, at the cost of an increase in mass fraction of ribosomal sector proteins (information storage and processing), consistent with the three-component proteome allocation model.

and the remaining non-ribosomal proteins (P-sector) whose mass fraction $\phi_P \to 0$ as $\phi_R \to \phi_R^{\max}$ (Figure 1.3 **A-B**). Given the invariance of $\phi_Q$ with translational perturbations, the $R$- and $P$- sectors add up to a constant such that $\phi_R + \phi_P = \phi_R^{\max} = 1 - \phi_Q$.

During steady-state exponential growth, the rate of amino acid supply by the $P$-sector proteins must be balanced by the rate of amino acid consumption by the $R$-sector proteins, such that there is no net change in the amino acid pool. If the amino acid pool increases such that the supply exceeds demand, then $\phi_R$ increases to meet the demand of protein biosynthesis and simultaneously decrease supply due to the constraint $\phi_P = \phi_R^{\max} - \phi_R$ [8]. This strategy underlies flux balance and maximization of the growth rate. The partitioning of the proteome into three main components is supported by

mass spectrometry data [6] (Figure 1.3 **B**) where clustering the proteins based on their function reveals similar behaviour to the proposed model components. More precisely, the category identified as "information storage and processing", which contains ribosome-affiliated proteins, increases with growth rate, while the "metabolism" cluster decreases with growth rate, equivalent to the non-ribosomal proteins in the $P$-sector. This leaves the mass fraction of the rest of the proteins to be independent of growth rate, akin to the housekeeping $Q$-sector.

## 1.3 Proteome allocation strategies for bacterial growth control

The proteome partitioning model [4] generates constraints on cellular resource strategies linking cell growth, nutrient uptake, metabolism and protein synthesis. This framework provides a theoretical basis for explaining the empirical growth laws (Eq. 1.2 and 1.3). The positive linear relationship between growth rate and ribosome mass fraction follows from exponential growth of total protein mass $M$ at steady-state: $\mathrm{d}M/\mathrm{d}t = \kappa M$. The rate of accumulation of protein mass is balanced by the rate of protein synthesis by active ribosomes:

$$\kappa M = \kappa_t (M_R - M_R^{\min}) \tag{1.4}$$

where $M_R^{\min}$ is the mass of inactive ribosomes, leading to the first empirical growth law in Eq. (1.2). The second growth law (Eq. 1.3) follows from the constraint on amino acid flux to meet the demand of protein synthesis during exponential growth [42, 4, 8] Fig. 1E. The rate of change of amino acid concentration ($A$) in a cell is given by:

$$\frac{\mathrm{d}A}{\mathrm{d}t} = \kappa_n(A)\phi_P - \kappa_t(A)(\phi_R - \phi_R^{\min}) \ , \tag{1.5}$$

where $\phi_P = \phi_R^{\max} - \phi_R$ and both the translational capacity ($\kappa_t$) and the nutritional capacity ($\kappa_n$) are functions of the amino acid concentration $A$. In particular, $\kappa_t$ increases and then saturates with $A$ [43, 8], whereas there is a negative feedback control of $\kappa_n$ to limit the concentration of amino acids [44]. At steady-state, there is no net accumulation of amino acids in the cell: the nutrient import needs to meet the demands of synthesizing new proteins [4, 8, 45], resulting in the growth law: $\kappa = \kappa_t(\phi_R - \phi_R^{\min}) = \kappa_n(\phi_R^{\max} -$

$\phi_R$). The flux balance condition then determines the relationship between steady-state ribosome mass fraction and amino acid concentration:

$$\phi_R = \frac{\kappa_n(A)\phi_R^{\max} + \kappa_t(A)\phi_R^{\min}}{\kappa_n + \kappa_t} \ . \tag{1.6}$$

As a result the steady-state value of $\phi_R$ decreases with $A$, but there is no unique value of ribosome mass fraction that satisfies the amino acid flux in a given growth condition. How do then bacterial cells regulate the ribosomal mass fraction $\phi_R$? The optimum value of ribosome mass fraction is set by the maximum achievable growth rate [42, 8], which exhibits a unique maximum as a function of $\phi_R$ (Fig. 1.4 **B**). In a given growth environment the maximum growth rate is reached when both the translational and nutrient capacities are at their maximal value, and increases with increasing $\kappa_n$. In similar spirit, other mechanistic models of growth rate optimization and ribosome regulation have been developed [46, 47, 48, 49].

Taking further the idea of compartmentalizing the proteome, Pandey and Jain [7] developed a *precursor-transporter-ribosome* model, where they considered the coupled dynamics of transporters ($P$) that import nutrients from the extracellular medium and convert them into amino acid precursors ($A$). The amino acids are then converted into transporters and ribosomal proteins ($R$) (Figure 1.4 **A**). The ribosomes in turn catalyze the production of both transporters and ribosomes, while the transporters catalyze the production of more precursors [7]. The coupled dynamics of transporters (mass $M_P$) and ribosomal proteins (mass $M_R$) are given by

$$\frac{\mathrm{d}M_P}{\mathrm{d}t} = \kappa_t f_P(M_R - M_R^{\min}) - d_P M_P \tag{1.7}$$

$$\frac{\mathrm{d}M_R}{\mathrm{d}t} = \kappa_t f_R(M_R - M_R^{\min}) - d_R M_R \tag{1.8}$$

where $d_P$ and $d_R$ are the degradation rates for the transporters and the ribosomes, respectively, $f_R$ is the fraction of ribosomes engaged in the production of ribosomal proteins, and $f_P$ is the fraction of ribosomes catalyzing the production of transporters. The parameters $f_R$ and $f_P$ are subjected to the constraint: $f_P + f_R = \phi_R^{\max}$, where the choice of

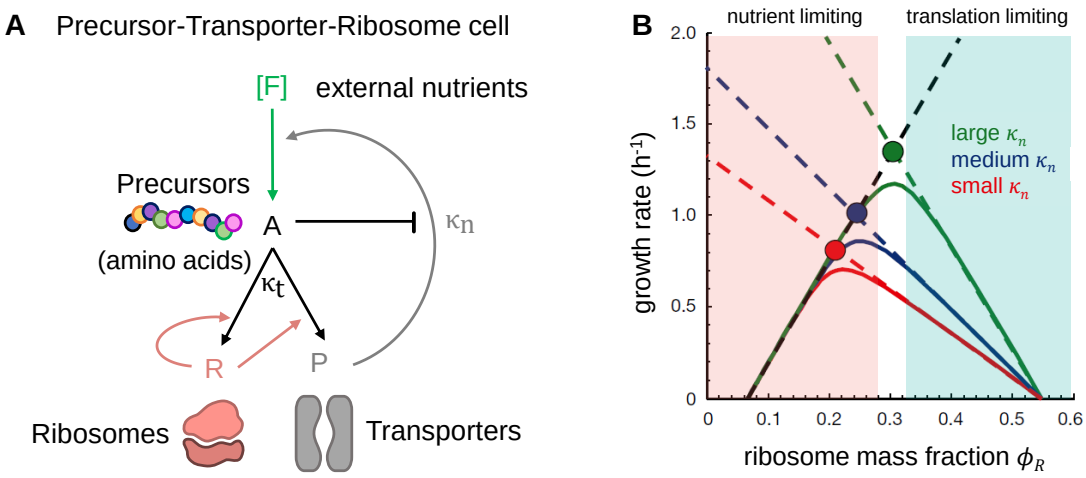


Figure 1.4: **Minimal model for nutrient import, amino acid production and protein production in a bacterial cell. A.** Schematic of the Precursor-Transporter-Ribosome model of a minimal cell [7]. Precursor molecules (amino acids, A) are produced by the action of transporters (P) on the external nutrients. Transporters (P) and ribosomal proteins (R) are synthesized from the precursors by the ribosomes R. **B.** The optimum value of the ribosomal protein mass fraction $\phi_R$ depends on the growth environment (poor nutrient - red line, moderate nutrients - blue, rich nutrient - green). Dashed lines correspond to the equation: $\kappa = \kappa_t(\phi_R - \phi_R^{\min})$ and $\kappa = \kappa_n(\phi_R^{\max} - \phi_R)$. For each nutrient condition the growth rate exhibits a maximum (solid circle) corresponding to an optimal allocation of $\phi_R$. The upper bound on the growth rate maximization occurs when the translation efficiency $\kappa_t$ and the nutritional efficiency $\kappa_n$ are both maximum for a given nutrient environment. Figure adapted from Ref. [8].

$f_R$ can be determined by the regulatory condition of growth rate maximization [42]. In a given growth environment with other cellular parameters fixed, the regulation adjusts the value of $f_R$ such that the growth rate is maximized (Figure 1.4 **B**). The optimized steady-state of the precursor-transporter-ribosome model then reproduces the empirical growth laws (Eq. 1.2 and 1.3) [7]. Thus the proteome allocation theory provides a promising framework to understand the relationships between the growth rate and macromolecular

composition of the bacterial cell.

## 1.4 Cell size control and homeostasis in bacteria

How cell size adapts to changes in growth conditions is a fundamental question in bacterial growth physiology. Soon after Monod's growth law was formulated, Schaechter *et al.* revealed how bacteria modulate cell sizes in response to changes in nutrient conditions. By studying the growth and morphologies of *Salmonella enterica* cells in different nutrient conditions, Schaechter *et al.* discovered the *nutrient growth law* – the average cell size of a bacterial population ($V^{pop}$) increases exponentially with the population growth rate ($\kappa^{pop}$) [50]:

$$V^{pop} \propto e^{\alpha \kappa^{pop}}, \tag{1.9}$$

where $V^{pop}$ is usually measured as optical density, $\kappa^{pop}$ is measured as doublings of culture volume per hour and $\alpha$ is a constant. For a better size characterisation, the length and diameter of cells can be measured at the single cell level. Trueba and Woldringh [51] found that the diameter of *E. coli* cells negatively correlate to the length during the cell cycle in a systematic way. Under different growth conditions, they find that cells grown in rich nutrients are larger than cells grown in poor nutrients, consistent with the nutrient growth law.

Recent studies have confirmed the result in Eq. 1.9 for evolutionary divergent bacterial species such as *E. coli*, *Bacillus subtilis* and *Sinorhizobium meliloti* [32, 52, 5, 53, 54], suggesting shared strategies for cell size control in bacteria. However, deviations from the nutrient growth law have been reported in studies perturbing cellular growth rate and translation via antibiotics [15, 5]. Thus the relationship between cell size and growth rate does not simply follow from the nutrient growth law and requires a deeper systems-level understanding of cellular growth physiology at single-cell level.

At single-cell level, control of cell size emerges from a temporal coupling between growth and division. There are three main mechanisms: *sizer*, *timer* and *adder* as shown in Figure 1.5 **A**. The *sizer* model assumes that cells divide after reaching a threshold size

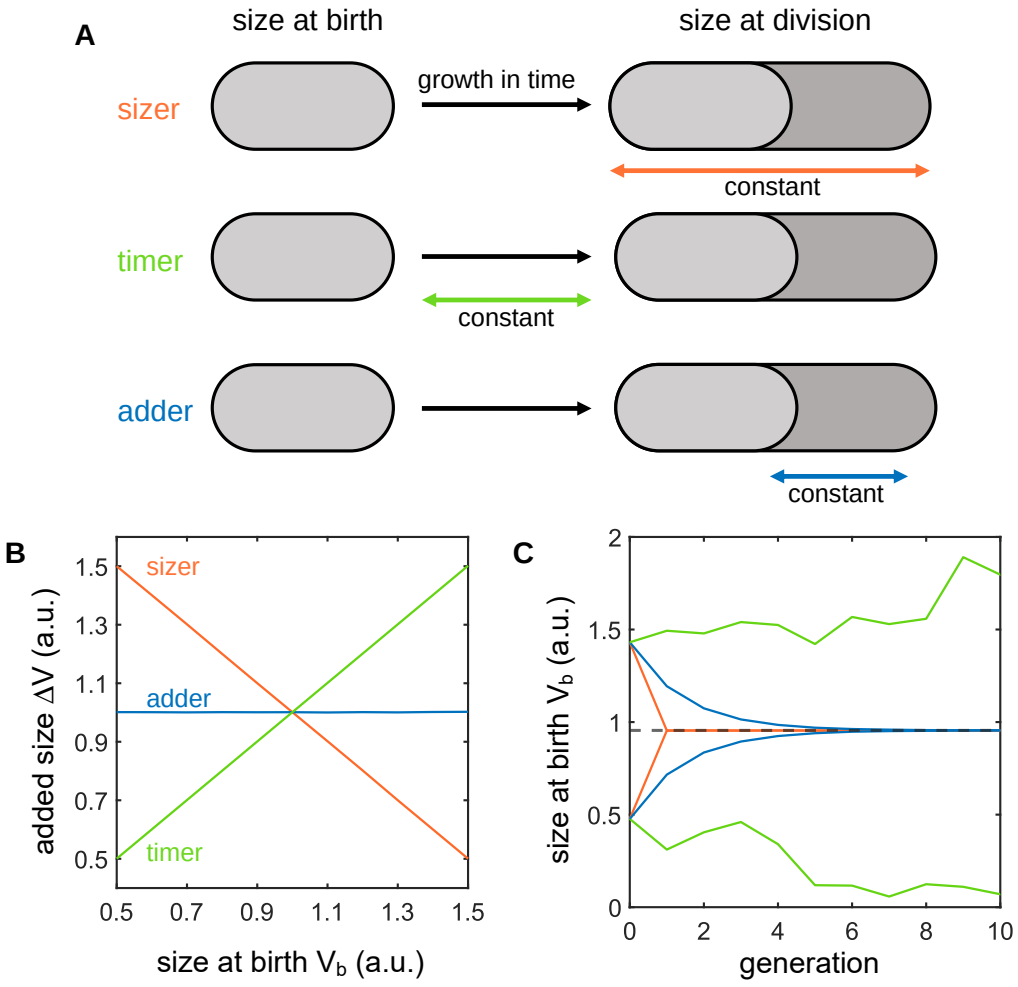


Figure 1.5: **Mechanisms for cell size homeostasis in bacteria. A.** Schematic showing the three main mechanisms for cell size control: sizer – the size at birth is constant $V_b = const.$, timer – the growth time/cycle duration is constant $\tau_{cyc} = const.$ and adder – the added size is constant $\Delta V = const.$ **B.** Added size as a function of size at birth for each mechanism with slopes $-1$, 0 and 1 for sizer, adder and timer respectively. **C.** Corrections of long and short cell sizes across several subsequent generations, where the dashed line indicates the target cell size. The size at birth $V_b$ diverges from the target size for the timer mechanism in the presence of noise in growth and division ratio.

drawn from a probability distribution that depends on growth conditions: $V_d = const.$ where $V_d$ is the cell size at division. In the *timer* model cells divide after a constant time has elapsed since birth. In other words, the duration of the cell cycle ($\tau_{cyc}$) is constant for exponentially growing cells: $\tau_{cyc} = const.$ And lastly, the *adder* mechanism proposes that cells divide upon adding a constant size ($\Delta V$) between consecutive division events: $\Delta V = V_d - V_b = const.$, where $V_b$ is the cell size at birth. Each model shows a characteristic slope when plotting the added cell size between birth and division against the size at birth: $-1$, 0 and 1 for sizer, adder and timer respectively Figure 1.5 **B**. While the sizer and adder model ensure cell size homeostasis, there is little to no cell size correction in the timer morel (Figure 1.5 **C**).

Individual cells achieve size homeostasis via a negative feedback between the cell size at birth and inter-division times [55, 56, 32, 57, 58]. A particular manifestation of this principle is the adder model [55, 59, 25, 60, 32]. By virtue of this adder mechanism, larger cells divide in less time than smaller cells, such that cells deviating from the homeostasis cell size quickly converge to the average cell size in a few generations (Figure 1.5 **C**). While this strategy for cell size homeostasis is followed by a wide range of bacterial species including *E. coli*, *B. subtilis*, and *Pseudomonas aeruginosa* [59, 25, 60, 61, 32]), the adder model does not readily reveal neither a molecular basis for cell size control nor any connections between cell size and growth physiology.

In recent years, regulatory models have emerged that provide a molecular-level understanding of cell size control and the coupling between cell growth and division in bacteria. First is the *replication-initiation-centric* model [62, 57, 63], where cell size is determined by the time period of chromosome replication ($C$-period) and the interval between the end of chromosome replication and cell division ($D$-period). In this model, the cell divides after a fixed time interval ($C + D$ period) since the initiation of chromosome replication. Second is the *division-centric* model for cell size control [25, 12, 64, 17, 65, 66], where cell division is triggered by accumulation of a threshold amount of division proteins [25, 12, 64, 65, 67] or cell envelope precursors [17]. However, how the synthesis of

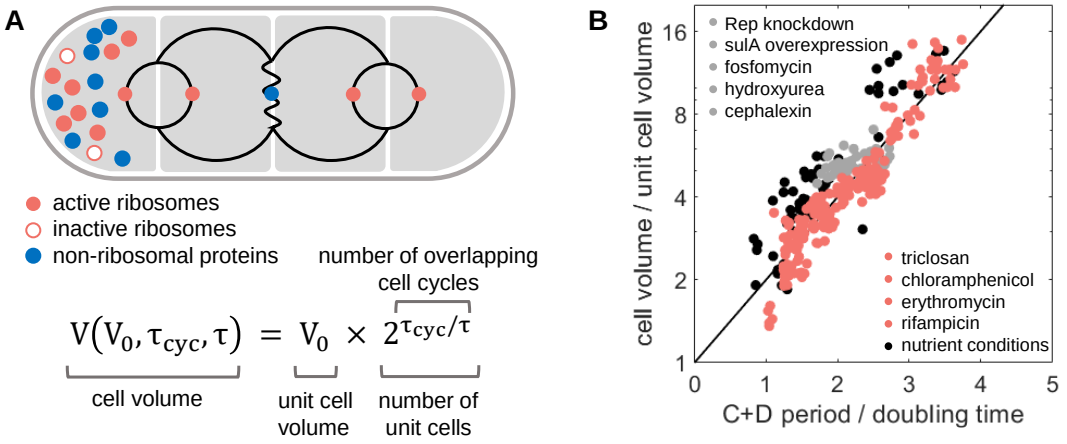


Figure 1.6: **General cell-size law in bacteria A.** Schematic adapted from Si *et al.* [5] showing the general cell size law, where the cell volume $V$ is related to the volume $V_0$ of unit cells as $V(V_0, \tau_{cyc}, \tau) = V_0 2^{\tau_{cyc}/\tau}$, where $\tau_{cyc}$ is the cell cycle duration ($C + D$ period) and $\tau$ is the cell doubling time. Each unit cell contains sufficient resources for self-replication (active ribosomes, inactive ribosomes, and nonribosomal proteins). the number of unit cells correlates with the number of overlapping cell cycles such that fast-growing cells that initiate multiple rounds of DNA replication have more unit cells. **B.** Experimental validation of the general growth law. After rescaling the cell volume by unit cell volume $V_0$ and the growth rate by $\tau_{cyc}^{-1}$, all data obtained for translation perturbations and other types of perturbation (see legend) collapse onto the master curve $V/V_0 = 2^{\tau_{cyc}/\tau}$. Data taken from [5].

division initiator proteins and the $C + D$ period is controlled by the bacterial cells in different growth conditions is not well understood, leaving open the relationship between cell size, growth rate and division timing.

## 1.5 Bacterial cell size law

In recent work, Si *et al.* [5] established a general *cell size law* for bacteria that is able to predict bacterial cell size for a wide range of genetic, antibiotic and nutrient perturbations.

Using turbidostat in combination with high-throughput image analysis, Si *et al.* measured the relationship between cell size and growth rate under perturbations to translation, transcription, DNA replication, cell division and cell wall synthesis for a range of nutrient limitations. Their findings experimentally confirmed the phenomenological relationship between cell volume $V$, cell cycle duration $\tau_{cyc}$ ($= C + D$ period) and the cell doubling time $\tau$ originally proposed by [62] (Figure 1.6):

$$V = V_0 2^{\tau_{cyc}/\tau} , \tag{1.10}$$

where $V_0$ is the cell size at initiation or size of a *unit cell*, which remains constant ($V_0 \approx 0.27 \mu m^3$) under growth perturbations. Each unit cell contains all the necessary components for self-replication [5] such that the cell size at division is the sum of all the unit cells. Interestingly, the volume of a unit cell coincides with a *B. subtilis* bacterial spore volume (0.2 - 0.3 $\mu m^3$) – the smallest self-sufficient bacterial compartment [27, 31]. The general growth law for cell size accounts for cell cycles longer than the average doubling time ($\tau_{cyc} > \tau$) where the chromosome contains multiple replication forks (Figure 1.6 **A**). After rescaling cell size with the initiation size and growth rate with the inverse of the $C + D$ period, all the available data collapse on the curve predicted by the general growth law (Figure 1.6 **B**). The invariance of initiation mass with elongation rate and birth size is consistent with the threshold initiation model – the molecular origin of the adder model for cell size control (Chapter 2), but its mechanistic origin remains unknown. Si *et al.* [5] discuss that the threshold initiation model alone is not sufficient to explain the invariance of the unit cell. In addition, the initiator concentration must also be independent of the growth conditions and growth inhibition. Furthermore, they predicted the existence of a specific protein sector that is constant under physiological perturbations that alter the ribosome fraction of the proteome.

## 1.6 Outline of the thesis

In Chapter 2, I focus on quantitative models of cell size control, introducing the threshold initiation model for cell size homeostasis and an extended resource allocation model for

understanding how bacterial cells optimize their macromolecular resources to control cell sizes in response to nutrient conditions. I show how a nutrient-dependent trade-off between resources allocated to growth and division leads to cell sizes in agreement with experimental observations. The models suggest a possible molecular origin of the phenomenological nutrient-growth law, connecting the gap between the single-cell growth and division behaviour in *E. coli cells* (i.e. the *adder* model) and the population average cell size scaling with the growth rate imposed by the growth medium.

The theory presented in Chapter 2 can also capture the divergence from the nutrient growth law under translation inhibition. While under nutrient perturbations the allocation of resources is balanced between growth and division, under translation inhibition the balance is broken leading to three distinct cell volume behaviour. Bacteria can increase, decrease or keep their sizes constant under chloramphenicol treatment suggesting distinct adaptive mechanisms based on the surface-to-volume changes for nutrient influx promotion or decreased influx of antibiotics.

In Chapter 3, I investigate the shape of the cells in preparation of testing the results for the three distinct behaviours of the cell size and therefore surface-to-volume ratio under translation inhibition. I start by introducing a model for bacterial shape regulation which leads to a universal scaling law between cell surface area and volume in bacterial cells. This allows us to explain how the cell shape is regulated under nutrient perturbations, therefore gaining a complete physiological description of the bacterial cells' behaviour in different growing media.

In Chapter 4, I study how the cell size and shape are altered by antibiotics and investigate how cell shape changes promote bacterial fitness to counter the growth inhibitory action of antibiotics. I compare the theoretical predictions from Chapter 2 to experimental data by simulating the dynamics between translation inhibition antibiotics and ribosomes. Knowing the size and shape dependency on ribosomes from previous chapters, we can also look at the dynamics of size and shape and compare their nutrient-dependent response to different antibiotic concentrations to experimental data.

In Chapter 5, I present a theoretical model for how bacteria allocate the intake energy for the main physiological functions in the cell, such as metabolism, growth, division and maintenance. The model proposed links the proteomic resource allocation strategies proposed in Chapter 2 to the mechanical components of the cell.

Chapter 6 is the conclusion chapter, where I summarise the main findings of the thesis and propose ideas for future work.

# Chapter 2

# Theory of cell size control in bacteria

Cell size control emerges from a regulated balance between the rates of cell growth and division. In bacteria, simple quantitative laws connect cellular growth rate to ribosome abundance. However, it remains poorly understood how the molecular components control the cell size. In this Chapter I show how cell size maintenance under nutrient perturbations emerges from a balanced trade-off between ribosomes and division protein synthesis. Deviations from this trade-off relationship are predicted under translational perturbations, leading to distinct modes of cell morphological changes, in agreement with single-cell experimental data on *Escherichia coli*.

Part of this chapter is published in Serbanescu, D., Ojkic, N., & Banerjee, S. (2020). Nutrient-dependent trade-offs between ribosomes and division protein synthesis control bacterial cell size and growth. *Cell reports*, 32(12), 108183. [65]

Cell size maintenance is essential for regulating cell physiology, function and fitness [35]. Maintaining a characteristic cell size necessitates an intricate balance between cell growth and division rates. How this balance is achieved in different growth conditions remains an outstanding question. As discussed in Chapter 1, bacteria modulate their growth rate in response to changes in nutrient conditions – the *nutrient growth law* (Eq.1.9), while at the single-cell level, cell size homeostasis is achieved via the *adder* mechanism, whereby cells add a constant volume between consecutive division events, irrespective of the cell size at birth [57, 68, 69, 70]. However neither the phenomenological population level size scaling with nutrient-imposed growth rate nor the single cell size homeostasis achieved via the adder model reveal a molecular-level understanding of the mechanism for size control.

Two distinct types of regulatory models have been proposed in recent years for the control of bacterial cell size – (1) replication-initiation-centric model: cell size control is set by the time period of chromosome replication and the subsequent cell division ($C + D$ period) [62, 63, 57], and (2) division-centric model: cell size is regulated by the accumulation of a threshold amount of cell envelope precursors [71] or division proteins (e.g. FtsZ) [12, 67]. In replication-initiation-centric models, cell size at division is determined by the $C + D$ period, but it remains poorly understood how $C$ and $D$ periods are modulated by growth perturbations targeting translation or protein expression. Recent studies have challenged the replication-initiation-centric models for cell size control [72, 73, 74, 12], suggesting concurrence of replication initiation and division processes [73]. In particular, experiments have demonstrated that replication initiation and cell division are independently controlled in *E. coli* and *B. subtilis* [12], and data support a model that cell division is triggered by the accumulation of a threshold amount of division proteins [25, 64]. However, it remains unknown how the synthesis of division proteins is altered by nutrients or translational perturbations in order to regulate cell size.

A key component in understanding cell size regulation is the interdependence be-

tween growth rate and the macromolecular composition of the cell. The nutritional content of the growth medium sets the specific growth rate [11, 8], which in turn regulates the macromolecular composition of cells [75, 76]. For exponentially growing *E.coli* cells, RNA and ribosome abundance increases linearly with increasing the specific growth rate [77, 78, 79, 80, 81, 39]. This implies an upregulation in translation leading to increased protein production for growth [81, 82, 83] and cell size inflation. While this model is in agreement with experimental observations for cell size increase with increasing nutrient concentrations, it fails to explain cell size changes under translation inhibition [81, 9]. In particular, it remains unclear whether translation inhibition would lead to an increase in cell size such that there is a positive correlation between cell size and ribosome abundance, or a decrease in cell size with growth rate reduction. Both these behaviors are observed in experiments [9]. To explain how translation and nutrient quality regulates cell morphologies, we develop a whole-cell coarse-grained theory that links ribosomes with cell geometry, division control and the extracellular environment.

The proposed theoretical framework combines a mechanistic model of cell shape and division with an extended ribosomal resource allocation model, allowing us to quantitatively predict cell size changes under nutrient shifts and translational perturbations (Chapter 4. We use ribosome abundance as the one of the key regulatory variables as approximately 85% of cellular RNA encodes for rRNA that is folded in ribosomes [4, 3]. We also assume that all the nutrients transported from the extracellular medium into the cell are used in the production of ribosomes and other proteins. This is because over 80% of cell's energy budget for biomass is spent on rRNA and protein synthesis [84]. Using this framework, we uncover a model for balanced allocation of ribosomal resources towards cell growth and division. We find that a balanced trade-off between the rates of cell growth and synthesis of division proteins sets bacterial size under nutrient shifts. As a result, in nutrient rich media, cells produce division proteins slower than the rate of cell elongation leading to larger cell sizes.

## 2.1 Cell size control emerges from nutrient-dependent trade-off between rates of cellular growth and division protein synthesis

To understand how bacterial cell size changes with the nutrient specific growth rate, we develop a model for the allocation of ribosomal resources towards cell growth and division protein synthesis. During each cell cycle, cells elongate exponentially in volume ($V$) at a rate $\kappa$. At steady-state, $\kappa$ depends linearly on the ribosomal mass fraction $\phi_R$ ($\approx$ RNA/protein ratio), such that

$$\frac{\mathrm{d}V}{\mathrm{d}t} = \kappa(\phi_R)V(t) \ , \tag{2.1}$$

where $\kappa(\phi_R) = \kappa_t(\phi_R - \phi_R^{\min})$ [4] (Eq. 1.2). Here, $\kappa_t$ can be interpreted as the translational capacity of the cell, which correlates with the speed of translational elongation [85], and $\phi_R^{\min}$ is the minimum mass fraction of ribosomes needed for growth (Figure 2.1 **C** inset). The value for $\phi_R^{\min}$ is obtained from the intercept of $\kappa$ as a function of $\phi_R$ from experimental data [10, 9].

We combine this model for growth with a model for the control of cell division (Figure 2.1 **A**). The division proteins, $X$, are synthesised at a rate proportional to the cell volume and degraded at a rate $\mu$:

$$\frac{\mathrm{d}X}{\mathrm{d}t} = k_p(\phi_R)V(t) - \mu X(t) \ , \tag{2.2}$$

where $k_p(\phi_R)$ is the rate of synthesis of division proteins that is assumed to be a function of the ribosome mass fraction $\phi_R$. Cell division is triggered when a threshold copy number of division proteins, $X_0$, is accumulated at the mid-plane of the cell (Figure 2.1 **B**). While various proteins could be potential candidates for division initiation [86, 87, 88, 89], a recent study identifies FtsZ as the key initiator protein that assembles a ring-like structure in the mid-cell region to trigger septation [90]. We therefore suggest that $X$ represents FtsZ copy number, and assume that its turnover rate in the ring-bound state is much faster than its rate of synthesis [91]. As a result, all the newly synthesised FtsZ in the cytoplasm are assumed to be recruited in the ring. We note that the degradation of $X$ is consistent with reports of active degradation of FtsZ by ClpXP [92, 93, 90].

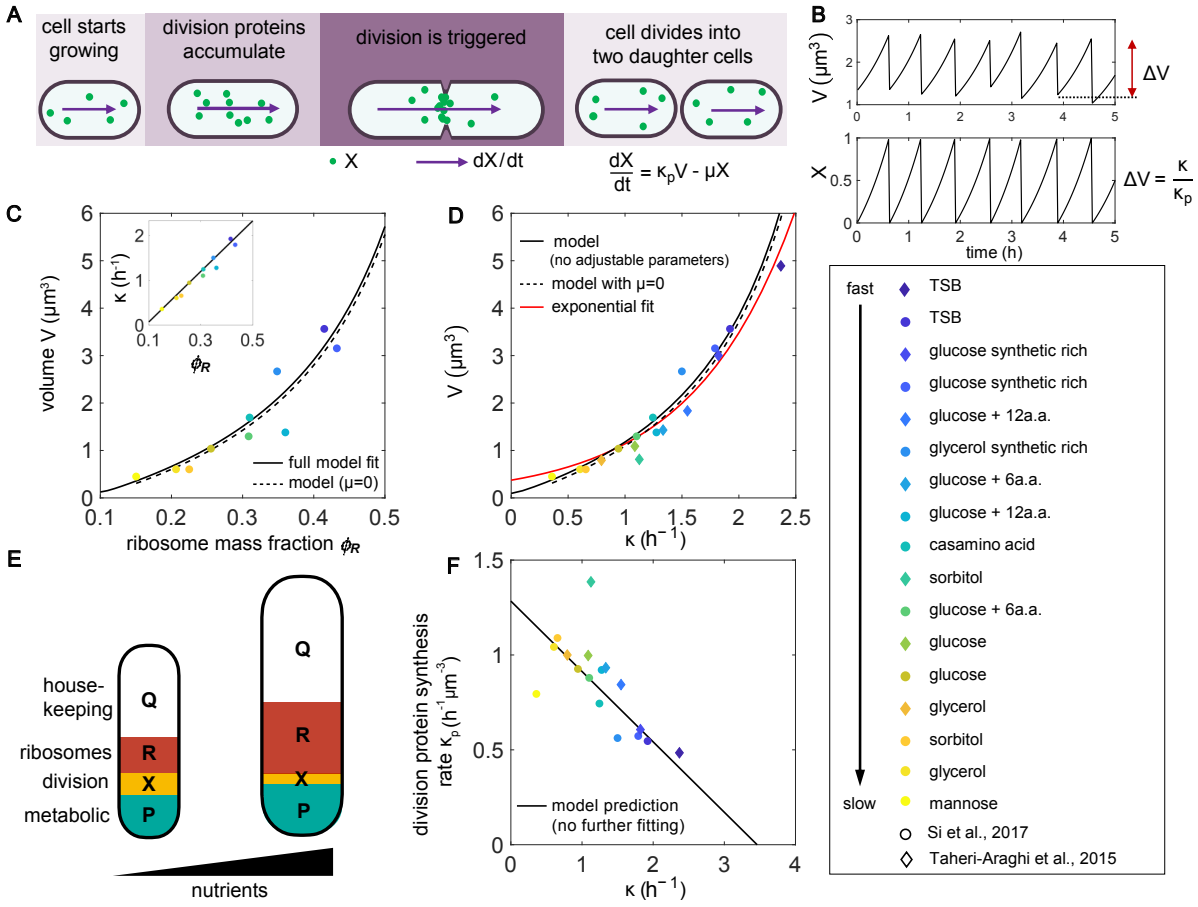


Figure 2.1: **Cell size control under nutrient perturbations. A.** Schematic of the threshold initiation model. Once a threshold amount of division proteins, $X$, is accumulated, cell division is triggered. Division proteins are synthesized at a rate $\kappa_p$ per unit volume. **B.** Dynamics of cell volume and fraction of division proteins show that the average added volume between consecutive division events is constant, consistent with the phenomenological adder model [9]. **C.** Fitted model for average cell volume as a function of ribosome mass fraction. Solid line: Full model fit with X protein degradation, Dashed line: Approximate model with no X degradation ($\mu = 0$). Inset: fitted linear relationship $\kappa = \kappa_t(\phi_R - \phi_R^{\min})$ [10]. **D.** Model prediction for the relationship between the average volume and growth rate compared against an exponential fit as predicted by the nutrient growth law [11].

Figure 2.1: Continued caption. **E.** Schematic representation of the proteome allocation model, showing ribsomal tradeoff between cell growth and division protein synthesis for cells growing in poor and rich nutrient media. **F.** Negative correlation between the rate of division protein synthesis and growth rate, as predicted by the model. Experimental data are obtained from Si *et al.* [9] and Taheri-Araghi *et al.* [70]. In the experimental data $\kappa_p$ is estimated from the ratio $\kappa/\langle V\rangle$. See Table 7.2 for a complete list of parameter values. Note: We introduce noise in the division ratio $D_R$ such that $V_{i+1}(t=0) = D_R V_i(t=\tau_i)$, where $V_{i+1}(t=0)$ is the volume of the cell in generation $i+1$ at birth, $V_i(t=\tau_i)$ is the volume of the cell in generation $i$ at division, $\tau_i$ is the division time and $D_R$ is a Gaussian random variable with mean 0.5 and standard deviation 0.05.

Solving Eq. (2.1) and Eq. (2.2), we obtain:

$$X_0 = (V_\mathrm{d} - V_\mathrm{b} 2^{-\mu/\kappa}) k_p/(\kappa+\mu)\ , \tag{2.3}$$

where $V_\mathrm{b}$ and $V_\mathrm{d}$ are the cell volumes at birth and division, respectively. In the limit $\kappa \gg \mu$, we get $X_0 = \Delta V k_p/\kappa$, where $\Delta V = V_\mathrm{d} - V_\mathrm{b}$ is the added volume per generation. As $X_0$, $k_p$ and $\kappa$ are constant for a given growth medium, cells add a constant volume $\Delta V$ in each growth generation, consistent with the phenomenological adder model. Conversely, in the limit $k \ll \mu$, $V_\mathrm{d} \approx X_0\mu/k_p$, consistent with data that *E. coli* deviates from an adder in slow growing media [57, 90]. Furthermore, for symmetrically dividing bacterium, the average newborn cell volume, $\langle V_\mathrm{b}\rangle$, asymptotes to $\Delta V$ [94]. Therefore, average cell volume $\langle V\rangle$ in a given growth medium is given by:

$$\langle V\rangle = \frac{\kappa+\mu}{\kappa_p(2-2^{-\mu/\kappa})}\ , \tag{2.4}$$

where $\kappa_p = k_p/(2X_0 \ln 2)$, is the normalized rate of division protein synthesis. Thus, cell volume can be modulated by perturbations in translation, as both $\kappa$ and $\kappa_p$ are functions of the ribosomal mass fraction.

A key proposition for the model is a tradeoff between the ribosomes allocated for

synthesizing growth and division proteins such that:

$$\kappa_P(\phi_R) = \kappa_P^0 \left(\phi_R^{max^*} - \phi_R\right) \ , \tag{2.5}$$

where $\kappa_P^0 = \frac{m_x \kappa_t}{\rho_c \rho}(\phi_R^{\max} - \phi_R^{\min})$ and $\phi_R^{max^*} = \frac{\kappa_n \phi_R^{\max} + \kappa_t \phi_R^{\min}}{(\kappa_n + \kappa_t)}$. We interpret $\kappa_P^0$ as the rate of production of FtsZ per ribosomes, and $\phi_R^{max^*}$ as the ribosome mass fraction when growth rate is maximum. Note that the parameter $\kappa_P^0$ can be perturbed by translation, whereas $\phi_R^{max^*}$ is regulated by both translational and nutritional capacities of the cell.

By combining the expressions for growth rate and division proteins synthesis rate, we find:

$$\langle V \rangle = \frac{\kappa_t(\phi_R - \phi_R^{min}) + \mu}{\kappa_p^0(\phi_R^{max^*} - \phi_R)(2 - 2^{-\mu/\kappa(\phi_R)})} \ , \tag{2.6}$$

such that average cell size increases with increasing ribosome abundance. We fit the expression in Eq. (2.6) to experimental data [9] in order to determine the parameters $\kappa_p^0$, $\mu$, and $r^*_{\max}$ (Figure 2.1 **C**, solid line). Importantly, we find that $\mu = 0.24$ h$^{-1}$, allowing us to approximate the average volume as the ratio of growth rate to the rate of division protein synthesis: $\langle V \rangle \approx \kappa/\kappa_p = \frac{\kappa_t(r - r_{\min})}{\kappa_p^0(r^*_{\max} - r)}$ (Figure 2.1 **C**, dashed line). Thus $\kappa_p$ can be indirectly measured from $\kappa/\langle V \rangle$ data across different growth conditions. Direct measurement of $\kappa_p$ would necessitate measuring the rate of change in FtsZ fluorescence intensity per unit cell volume during cell division cycles.

We can then express the average cell volume as a function of nutrient specific growth rate, recapitulating Schaecter et al.'s *nutrient growth law* [11] (Eq. 1.9) that cell size increases monotonically with increasing growth rate:

$$\langle V \rangle = \frac{\kappa}{\kappa_p^0(\phi_R^{max^*} - \phi_R^{min}) - \frac{\kappa_p^0}{\kappa_t}\kappa} \ . \tag{2.7}$$

With no further fitting, we directly compare the prediction in Eq. (2.7) with experimental data for *E. coli* cell volume under nutrient perturbations (Figure 2.1 **D**). The result in Eq. (2.7) deviates from the phenomenological model of exponential dependence between cell size and growth rate, and predicts a maximum growth rate, $\kappa_{\max} = \kappa_t(r^*_{\max} - r_{\min}) \approx 3.1\text{h}^{-1}$, when all ribosomal resources are allocated towards

growth. Our model captures the departure from an exponential relationship between cell size and growth rate for $\kappa < 0.7$ h$^{-1}$, as recently reported by Zheng et al [13] (Figure 2.2 **A**). We also find that a linear relationship between cell size and growth rate does not accurately capture the cell size data for the range of growth rates studied in this work.

## 2.2 Mechanistic origin of ribosomal tradeoff between growth and division.

To understand the mechanistic origin of the ribosomal tradeoff between growth and division protein synthesis (Eq. 2.5), we develop a model for allocation of ribosomal resources, extending the framework of Scott et al [10]. The total protein content of the cell can be decomposed into four classes (Figure 2.1): ribosome-affiliated proteins (R, mass fraction $\phi_R$), house-keeping proteins not affected by translation (Q, mass fraction $\phi_Q$), division proteins (X, mass fraction $\phi_X$), and the rest non-ribosomal proteins that constitute the metabolic sector (P, mass fraction $\phi_P$). The mass fractions are constrained by the equation: $\phi_R + \phi_X + \phi_P = 1 - \phi_Q = \phi_R^{\max} = \text{constant}$. For different combinations of the nutritional and translation capacities of the cell, efficient resource allocation requires that the abundance of P- and R-class proteins be adjusted so that the rate of nutrient influx by P matches the rate of protein synthesis achievable by R: $\kappa_n \phi_P = \kappa_t(\phi_R - \phi_R^{\min})$, where $\kappa_n$ is the nutritional capacity of the cell. This results in the following relation between the mass fractions of ribosomes and division proteins:

$$\frac{\phi_R - \phi_R^{\min}}{\phi_R^{\max} - \phi_R - \phi_X} = \frac{\kappa_n}{\kappa_t} \,, \tag{2.8}$$

predicting a negative correlation between $\phi_X$ and $\phi_R$ under nutrient or translational perturbations (Figure 2.2 **C**). Using a dynamic proteome sector model we can derive that the rate of production of division proteins, $\kappa_p$, is proportional to $\phi_X$ during steady-state growth.

## 2.3 Dynamic proteome sector model for the rate of production of division proteins

The total mass of division proteins, $M_X$, increases at a rate proportional to the amount of actively translating ribosomes, $N_R^{\text{active}}$,

$$\frac{dM_X}{dt} = af_X k_t N_R^{\text{active}} \ , \tag{2.9}$$

where $N_R^{\text{active}} = N_R - N_R^{\text{min}}$, $N_R$ is the total number of ribosomes, $N_R^{\text{min}}$ is the number of ribosomes not participating in protein synthesis, $k_t$ is the rate of translation per ribosome, $f_X$ is the fraction of ribosomes devoted to synthesizing $X$, and $a$ is the concentration of amino acids. Similarly, $dM_R/dt = af_R k_t N_R^{\text{active}}$, $dM_P/dt = af_P k_t N_R^{\text{active}}$, and $dM_Q/dt = af_Q k_t N_R^{\text{active}}$, where $M_R$, $M_P$ and $M_Q$ are masses of R, P and Q sector proteins, $f_P$, $f_R$, and $f_Q = 1 - f_R - f_X - f_P$ are the fractions of ribosomes devoted to synthesizing each of these sectors. Therefore, the total dry mass of the cell, $M = M_P + M_X + M_R + M_Q$, increases at a rate proportional to the number of active ribosomes,

$$\frac{dM}{dt} = ak_t N_R^{\text{active}} \ . \tag{2.10}$$

If $m_R$ is the mass of individual ribosomes, we get,

$$\frac{dM_X}{dt} = af_X k_t (M_R - M_R^{\text{min}})/m_R \ . \tag{2.11}$$

The instantaneous mass fraction of $X$, $\phi_X(t) = M_X(t)/M(t)$, then satisfies:

$$\frac{d\phi_X}{dt} + \kappa\phi_X = \frac{f_X k_t}{m_R} a(\phi_R - \phi_R^{\text{min}}) \ , \tag{2.12}$$

where $\phi_R$ is the mass of fraction of ribosomes. At steady-state $\phi_X = f_X$, using the relation: $\kappa = k_t a(\phi_R - \phi_R^{\text{min}})/m_R$. We can rewrite the above equation in terms of the concentration of $X$, $c_X = \phi_X \rho_c / m_x$, where $\rho_c$ is the mass density of the cell, and $m_x$ is the mass of an individual $X$ molecule. This gives us,

$$\frac{dc_X}{dt} + \kappa c_X = \frac{f_X k_t m_x}{m_R \rho_c} a(\phi_R - \phi_R^{\text{min}}) \ . \tag{2.13}$$

Using $X = c_X V$, where $X$ is total amount of division proteins in the cell, we derive dynamics of division protein accumulation,

$$\frac{dX}{dt} = \frac{f_X k_t m_x}{m_R \rho_c} a(\phi_R - \phi_R^{\min})V \ . \tag{2.14}$$

The above equation allows us to identify the division protein production rate as,

$$k_p = \frac{f_X k_t m_x}{m_R \rho_c} a(\phi_R - \phi_R^{\min}) \ . \tag{2.15}$$

The steady-state concentration of amino acids is determined by the balance between the rate of nutrient influx by transporters and the rate of translation by active ribosomes [8],

$$\frac{da}{dt} = k_n \phi_P - a\kappa_t(\phi_R - \phi_R^{\min}) \ , \tag{2.16}$$

where $\phi_P$ is the mass fraction of P-sector metabolic proteins, and $\kappa_t = k_t a\rho/m_R$. At steady-state, we have $a(\phi_R - \phi_R^{\min}) = k_n\phi_P/\kappa_t$. Using $\phi_X = \phi_R^{\max} - \phi_R - \phi_P$, we obtain

$$\phi_R = \frac{1}{\kappa_n + \kappa_t}\left(\phi_R^{\max}\kappa_n + \kappa_t\phi_R^{\min} - \phi_X\kappa_n\right) \ , \tag{2.17}$$

where $\kappa_n = k_n/a$. Therefore, $k_p \propto \phi_X\phi_P = \phi_X(\phi_R^{\max} - \phi_R - \phi_X) \approx \phi_X(\phi_R^{\max} - (\phi_R^{\max}\kappa_n + \kappa_t\phi_R^{\min})/(\kappa_n + \kappa_t))$, assuming that $\phi_X$ occupies a small fraction of the proteome. We thus get: $k_p \approx \phi_X(\frac{m_x}{\rho_c\rho})\kappa_n\kappa_t(\phi_R^{\max} - \phi_R^{\min})/(\kappa_t + \kappa_n)$. In terms of ribosome mass fraction, the rate of production of division proteins is then given by:

$$k_p = \frac{m_x\kappa_t}{\rho_c\rho}(\phi_R^{\max} - \phi_R^{\min})\left(\frac{\kappa_n\phi_R^{\max} + \kappa_t\phi_R^{\min}}{(\kappa_n + \kappa_t)} - \phi_R\right) \ , \tag{2.18}$$

where we identify $\kappa_p^0 \propto \kappa_t(\phi_R^{\max} - \phi_R^{\min})$ and $\phi_R^{\max^*} = (\kappa_n\phi_R^{\max} + \kappa_t\phi_R^{\min})/\rho(\kappa_n + \kappa_t)$ from Eq. 2.5. Thus the tradeoff between ribosomes, growth and division protein synthesis naturally emerges in an extended proteome allocation model. Growth rate $\kappa$ decreases with increased allocation of resources towards division proteins $\phi_X$ (Figure 2.1 **E-F**, and Figure 2.2 **D**):

$$\kappa = \frac{\kappa_n\kappa_t}{\kappa_n + \kappa_t}(\phi_R^{\max} - \phi_R^{\min} - \phi_X)/\rho \ . \tag{2.19}$$

With all the model parameters inferred from experimental data (Table 1), we can plot the dependency of $\kappa_p$ on $\kappa$ (Figure 2.1 **F**), showing the negative correlation between the division protein synthesis rate and the volumetric growth rate, and directly predict the dependency of cell volume on growth rate (Figure 2.2 **B**). Cells growing in poor nutrient medium allocate a smaller fraction of ribosomes towards growth, resulting in smaller size on average. However, cells growing in rich nutrients inflate their size by allocating a larger fraction of ribosomes towards growth (Figure 2.1 **E**).

## 2.4 Translation inhibition breaks balanced allocation of ribosomal resources

In a given nutrient medium, $\kappa/\kappa_p$ is maintained at a constant value, indicating a balance between growth and division protein synthesis. If $\kappa/\kappa_p$ remains invariant under translation inhibition, we expect cell size to remain unchanged, as previously suggested by Basan *et al.* [81]. However, experimental data [9] show that cell size could either increase, decrease or remain unchanged when *E. coli* cells are subjected to varying concentrations of Chloramphenicol – a ribosome-targeting antibiotic. We therefore hypothesize that translation inhibition breaks balanced allocation of ribosomal resources towards growth and division proteins, by differentially reducing the rates $\kappa$ and $\kappa_p$.

Under translation inhibition, bacteria produce more ribosomes to compensate for the inactive ribosomes that are bound by antibiotics [4]. By measuring bacterial growth rates ($\kappa$) and ribosome mass fractions ($\phi_R$) for increasing concentrations of Chloramphenicol, Scott *et al.* [4] found that $\kappa$ linearly decreases with $\phi_R$. In the presence of a division protein sector, the relationship between $\kappa$ and $\phi_R$ is given by:

$$\kappa = \kappa_n(\phi_R^{\max} - \phi_X - \phi_R) \ , \tag{2.20}$$

where $\kappa_n$ is the nutritional capacity that depends on nutrient quality, $\phi_R^{max}$ is the maximum ribosome fraction that cells can produce under translation inhibition. By combining Eq. (2.5) with Eq. (2.20), we obtain:

$$\kappa_p = \kappa_p^0(\kappa/\kappa_n + \delta r) \tag{2.21}$$

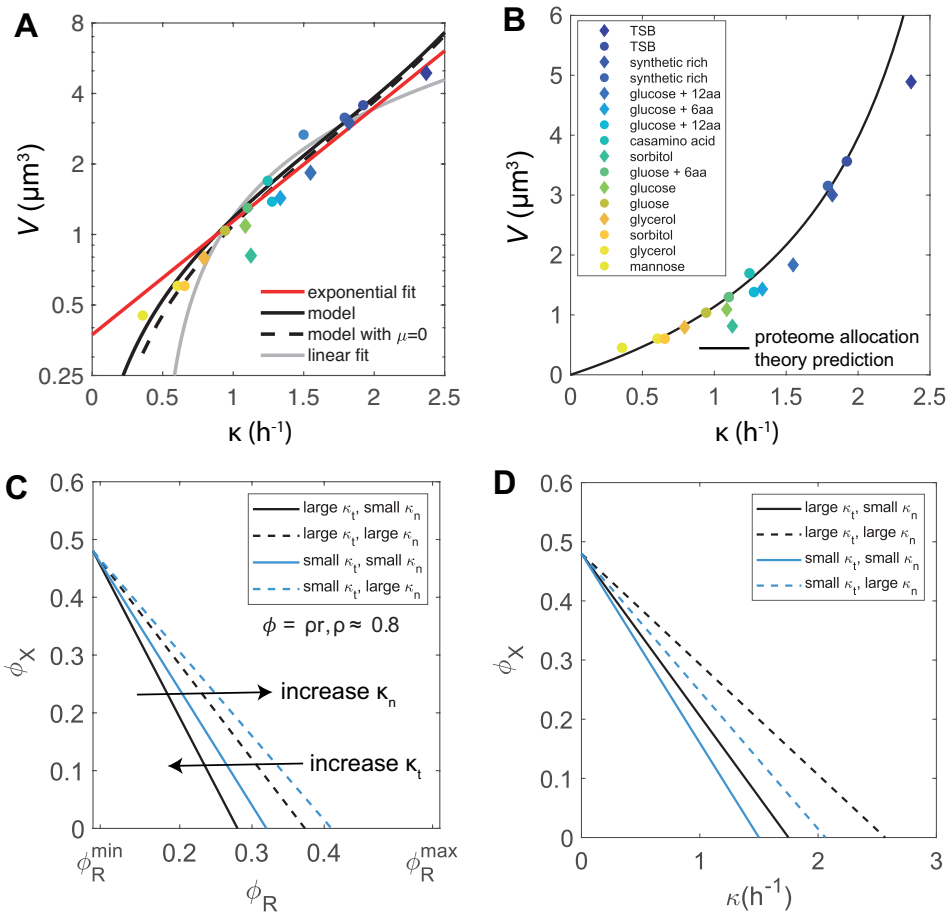


Figure 2.2: **Prediction of the proteome allocation theory. A.** Cell size versus growth rate, plotted in semi-log scale. **B.** Theoretical prediction for cell size using $\langle V \rangle = \kappa/(\kappa_p^0 \left(\phi_R^{max^*} - \phi_R^{min}\right) - \kappa_p^0 \kappa/\kappa_t$, where $\phi_R^{max^*}$ depends on the nutrient specific growth rate: $\phi_R^{max^*} = \left(\kappa_n \phi_R^{max} + \kappa_t \phi_R^{min}\right) / \left(\kappa_n + \kappa_t\right)$ **C.** Dependence of the division protein mass fraction $\phi_X$ on the ribosome mass fraction $\phi_R$. The tradeoff between $\phi_X$ and $\phi_R$ can be modeulated by translational $(\kappa_t))$ or nutritional $(\kappa_n)$ perturbations. $\rho$ is a conversion factor between ribosome mass fraction and ribosome concentration $(r)$: $\rho \approx 0.8$ [4], $\phi_R^{min} = \rho r_{min} \approx 0.08$, $\phi_R^{max} = \rho r_{max} \approx 0.56$. **D.** The same perturbations as in **C.** showing the relationship between $\phi_X$ and growth rate.

where $\delta r = \phi_R^{\max^*} - \phi_R^{max} + \phi_X$ can be interpreted as the excess ribosomal mass fraction allocated to division protein synthesis under translation inhibition. By combining

Eqs. 2.5, 2.8 and 2.20 we obtain a theoretical expression for the excess ribosomal mass fraction as a function of the growth rate: $\delta r = \kappa_n \Delta r/(\kappa_n+\kappa_t) - \kappa(\kappa_n+\kappa_t)/(\kappa_n\kappa_t)$, where $\Delta r = \phi_R^{max} - \phi_R^{min}$. Since $\kappa_n$ increases with $\kappa$ (Figure 2.3 **C**-inset), we predict that $\delta r$ increases monotonically with nutrient specific growth rate (Figure 2.3 **D**, solid line).

Unlike nutrient perturbations, we find that $\kappa_p$ and $\kappa$ are positively correlated under translation inhibition (Figure 2.3 **A**), such that they both decrease with increasing antibiotic concentration. Eq. (2.21) can be combined with Eq. (2.4) to determine how cell volume changes as a function of growth rate under translation inhibition:

$$\langle V \rangle = \frac{\kappa/\kappa_p^0}{\kappa/\kappa_n + \delta r} \, . \tag{2.22}$$

Interestingly, the above expression predicts three distinct behaviors for the cell volume (Figure 2.3 **B**):

$$\begin{cases} \delta r > 0 \rightarrow r^*_{\max} + r_X > r_{\max} : \text{more ribosomes allocated to division, V decreases} \\ \delta r = 0 \rightarrow r^*_{\max} + r_X = r_{\max} : \text{ribosomes equally shared between growth and division} \\ \delta r < 0 \rightarrow r^*_{\max} + r_X < r_{\max} : \text{excess ribosomes allocated to growth, V increases.} \end{cases}$$

We determine the parameters $\delta r$ and $\kappa_n$ for each growth medium, by fitting Eq. (2.21) to the experimental data for $\kappa_p$ vs cell growth rate $\kappa$ under Chloramphenicol perturbations [9] (Figure 2.3 **C**). We find that $\delta r < 0$ in poor media, $\delta r > 0$ in rich growth media, whereas $\delta r \approx 0$ for cells growing with medium growth rates (Figure 2.3 **D**). These data are consistent with our theoretical result that $\delta r$ increases linearly with the nutrient specific growth rate (Figure 2.3 **D**-solid line). We interpret the above result as cells allocating excess ribosomes for growth in poor media, whereas in rich media cells tend to allocate more ribosomal resources for division protein synthesis. With no further adjustable parameters, our theory predicts the cell volume curves for each growth conditions, which are in excellent quantitatively agreement with the trend in the experimental data (Figure 2.3 **E**).

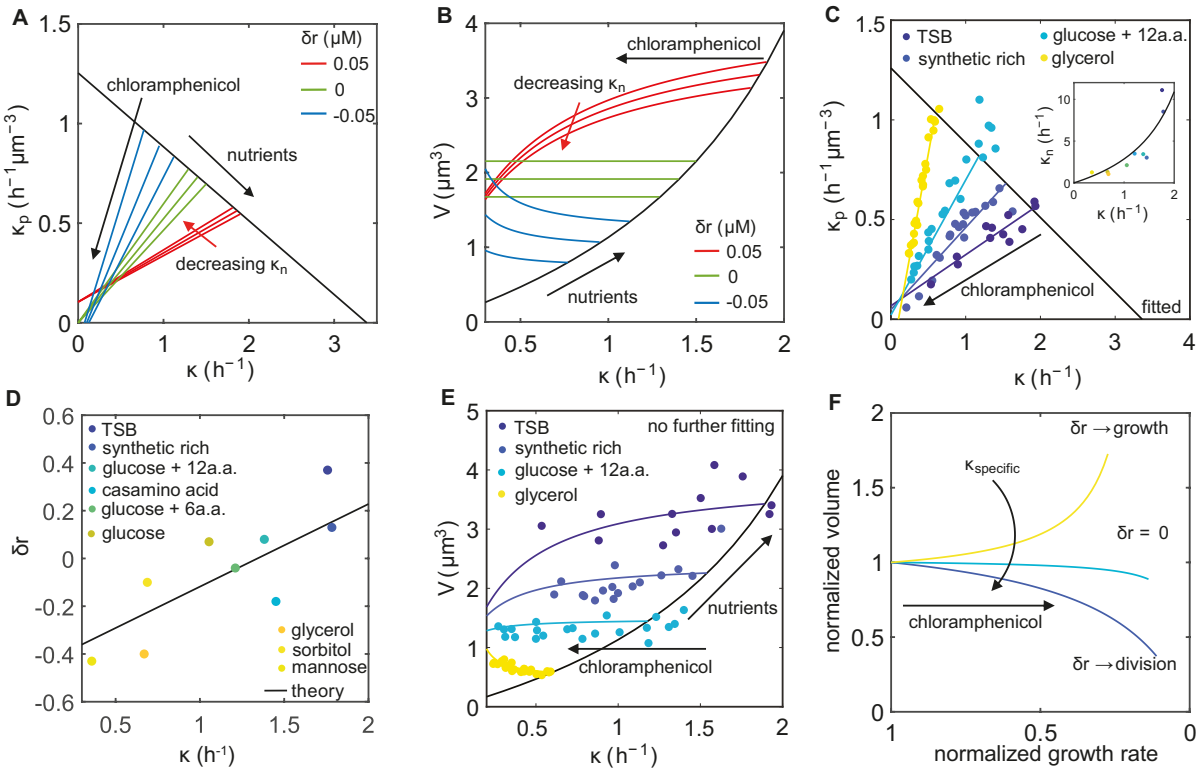


Figure 2.3: **Cell size control under translation inhibition. A.** Model prediction for the dependence of division protein synthesis rate $\kappa_p$ on growth rate $\kappa$ under translation inhibition for three values of $\delta r$. Decreasing $\kappa_n$ corresponds to decreasing the nutrient quality of the growth medium. **B.** Model predictions for cell volume versus growth rate under translation inhibition, capturing three distinct trends in cell size changes depending on the value of $\delta r$. **C.** Model fit to experimental data for $\kappa_p$ in three different nutrient conditions under translation inhibition. Inset: dependence of nutritional capacity $\kappa_n$ on the growth rate, Solid line is a fit of the form $\kappa_n = \kappa_t \kappa / (\kappa_m - \kappa)$, with the fitting parameter $\kappa_m = 2.6$. **D.** Dependence of $\delta r$ on nutrient-specific growth rate. Solid like shows the theoretical prediction for the dependence of $\delta r$ on nutrient-specific growth rate $\delta r = -\frac{\kappa_m}{\kappa} + (\phi_R^{max} - \phi_R^{min}) \frac{\kappa}{\kappa_m}$. **E.** Cell volume as a function of growth rate under translation inhibition.

Figure 2.3: Continued caption. **F.** Three distinct morphological responses to chloramphenicol, depending on the quality of nutrients. Volume and growth rates are normalized by their initial values before chloramphenicol is applied. In nutrient-rich media, cells allocate more ribosomes to division (dark blue line), thus increasing the surface-to-volume ratio to promote nutrient influx, whereas in nutrient-poor media they allocate more ribosome toward growth, inflating the cell size (yellow line) and in turn decrease the surface-to-volume ratio to reduce the antibiotic influx. See Tables 7.1 and 7.2 for a complete list of parameter values.

## 2.5 Discussion

We develop a whole-cell coarse-grained model for bacterial growth dynamics that connects intracellular control of translation, division control and extracellular environment. This provides a promising theoretical framework that quantitatively captures available experimental data for bacterial cell size and shape dynamics under nutrient and translational perturbations. During nutrient shifts, the ribosomal resources are optimally allocated to maintain a balanced trade-off between the rates of cell growth and division protein (FtsZ) synthesis. In rich nutrient media, more ribosomes are used for growth than division protein synthesis, leading to cell size inflation with increasing nutrient quality. Conversely in nutrient-poor media, cells allocate more ribosomal resources for division protein synthesis than growth, leading to a reduction in average cell size. This principle underlies the molecular basis for the celebrated *nutrient growth law* [11, 9], and can be interpreted as an optimization principle for cellular economy. Based on this principle, the resources allocated to a particular proteomic sector are inversely proportional to the efficiency of that sector [95]. In nutrient-rich media, cells invest more ribosomal resources to growth in order to compensate for a lower translational capacity. The latter can arise from an increased dilution rate of ribosomes under fast growth conditions, lowering the efficiency of protein synthesis. In nutrient-poor media, cells have a lower nutritional capacity that they compensate by allocating more resources to metabolism and division

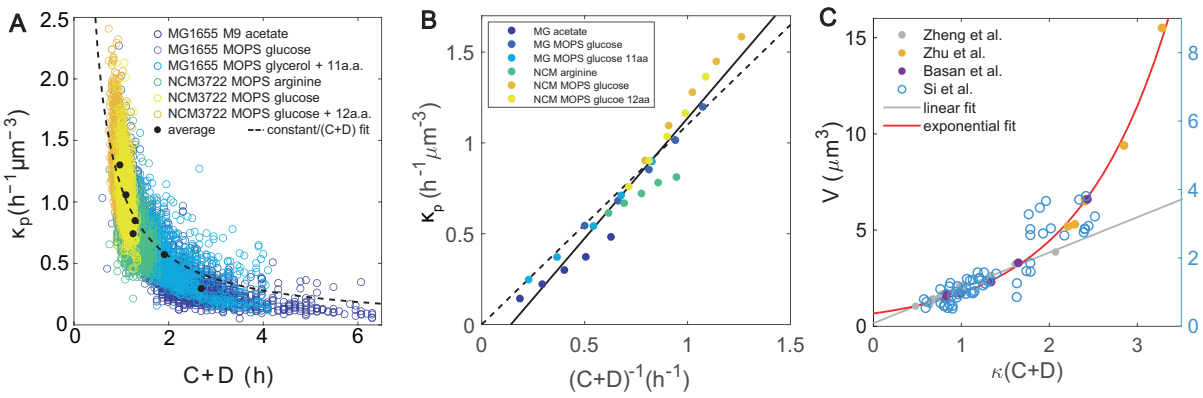


Figure 2.4: **Prediction of the proteome allocation theory. Relationship between cell size, division protein production rate and C+D period**. **A.** Scatter plot showing the negative correlation between kp and C+D, with data taken from [12]. $\kappa_p$ is estimated using the relation $\kappa_p \approx \kappa/V$. Dashed line is the best fit of the predicted relation $kappa_p \propto (C+D)^{-1}$, suggesting that measurements of $C+D$ period could reliably predict the production rate of the division proteins. **B.** Estimating $\kappa_p$ from measurements of the $C+D$ period. Dashed line is a fit through the origin as predicted by [13] and solid line is unconstrained linear fit. For each growth condition we removed the outliers that are more than three standard deviations away from the mean and then binned the data. **C.** Relationship between cell size and $\kappa(C+D)$. The gray line is a linear fit to data from Zheng et al. [13]. The red line is an exponential fit to data from Zheng et al. [13], Zhu et al. [14] and Basan et al. [15]. Data from Si et al. [5] is shown on y-axis to the right. We observe that a linear fit works well for $\kappa(C+D) < 2$.

protein synthesis.

To explain the mechanistic origin of the ribosomal tradeoff between growth and division protein synthesis, we propose a proteome allocation theory, extending the sector model introduced by Scott *et al.* [10]. In particular, we introduce a division protein sector X in the proteome, and derive a constitutive relation that the mass fraction of X, $\phi_X$, is a linearly decreasing function of the mass fraction of ribosomes, $\phi_R$. Existing experimental data support our model, and also falsify other possible models with X in the R-sector or

the Q-sector. In particular, if X is the R or Q sector we would expect cell size to always decrease under translation inhibition, a result that is inconsistent with experimental data [81, 9]. A recent study by Bertaux *et al.* [96] also incorporated division protein sector in a proteome model, extending the minimal Promoters-Transporters-Ribosomes cell model of Pandey and Jain [95]. In contrast to our theory, the authors assumed a phenomenological form for the dependence of $\phi_X$ on $\phi_P$ and $\phi_R$: $\phi_X \propto \phi_P^{\alpha}\phi_R^{\beta}$, where the exponents $\alpha$ and $\beta$ are deduced by fitting experimental data. The findings of Bertaux *et al.* are consistent with our results for cell size control under nutrient perturbations.

Basan *et al.* showed that the cell size increases or decreases with growth rate depending on the type of growth limitation [81]. In particular, when *E. coli* cells synthesize useless proteins, the cell size increases compared to the wild-type cells growing at similar rates. The useless protein over-expression decreases the growth rate by reducing $\phi_R^{max^*}$. Our model can capture the increase in volume if the division protein synthesis rate $\kappa_p$ is reduced more than the growth rate $\kappa$, from Eq. 2.6. However, we do not have experimental data to capture $\kappa_p$ or $\phi_R^{max^*}$ when the useless proteins are over-expressed.

Our model for division control is chromosome agnostic, and is thus inadequate for capturing the single-cell correlation patterns related to DNA replication initiation and segregation periods [73, 74]. However, we find that the rate of production of division proteins, $\kappa_p$, is proportional $(C+D)^{-1}$ (Figure 2.4 **A-B**), where $C$ is the duration from initiation to termination of one round of DNA replication, and $D$ is the time period from replication termination to cell division. This relationship between adder protein synthesis and chromosome dynamics emerges from combining the principle of balanced biosynthesis $\kappa_p \propto \kappa$ [90] with the relation $C + D \propto \kappa^{-1}$ [97]. The proportionality $\kappa_p \propto (C+D)^{-1}$ also emerges from the recent model suggested by Zheng et al that cell size is linearly proportional to $\kappa(C+D)$ [13]. Using $V \propto \kappa(C+D)$ in conjunction with our theory $V \propto \kappa/\kappa_p$ also reveals $\kappa_p \propto (C+D)^{-1}$, consistent with experimental data [90]. However, we note that a linear relationship between cell size and $\kappa(C+D)$ does not accurately describe all available experimental data [81, 98, 9] for cell size (Figure 2.4 **C**).

In this chapter I showed how a balanced trade-off between resources allocated for growth and division captures the cell size and shape dynamics under nutrient perturbations and translation inhibition. Interestingly, we find that under translation inhibition the balance is broken in a nutrient-dependent manner, with more ribosomes allocated to division leading to smaller cells in nutrient rich conditions. Conversely, in nutrient-poor conditions cells allocate more resources to growth thus increasing their size under chloramphenicol perturbations. The distinct mechanisms suggest that the cell shape plays an important role in cellular fitness. Bacteria promote nutrient influx by decreasing the volume or they reduce antibiotic influx by increasing the volume. To explore this idea, I introduce the cell shape in the next chapter and the morphological changes under antibiotic perturbations in Chapter 4.

# Chapter 3

# Control of bacterial cell shape

Rod-shaped bacterial cells can readily adapt their lengths and widths in response to environmental changes. While many recent studies have focused on the mechanisms underlying bacterial cell size control, it remains largely unknown how the coupling between cell length and width results in robust control of rod-like bacterial shapes. We uncover a conserved surface-to-volume scaling relation in *Escherichia coli* and other rod-shaped bacteria, resulting from the preservation of cell aspect ratio. To explain the mechanistic origin of aspect-ratio control, we propose a quantitative model for the coupling between bacterial cell elongation and the accumulation of an essential division protein (FtsZ). This model reveals a mechanism for why bacterial aspect ratio is independent of cell size and growth conditions.

---

Part of this chapter is published in Ojkic, N., Serbanescu, D., & Banerjee, S. (2019). Surface-to-volume scaling and aspect ratio preservation in rod-shaped bacteria. *Elife*, 8, e47033. [67]
Nikola Ojkic did the shape analysis and the simulations in Figure 3.3 and we collaborated on the theory in section 3.2.

Cell morphology is an important adaptive trait that is crucial for bacterial growth, motility, nutrient uptake, and proliferation [35]. When rod-shaped bacteria grow in media with different nutrient availability, both cell length and width increase with growth rate [11, 5]. At the single-cell level, control of cell volume in many rod-shaped cells is achieved via an *adder* mechanism [55, 59, 32, 57, 56] or an *initiator* model as presented in Chapter 2. A recent study has linked the determination of cell size to a condition-dependent regulation of cell surface-to-volume ratio [17]. However, it remains largely unknown how cell length and width are coupled to regulate rod-like bacterial shapes in diverse growth conditions [99, 100, 101, 102].

## 3.1 Surface-to-volume scaling and aspect ratio conservation at population level

Here we investigated the relation between cell surface area ($S$) and cell volume ($V$) for *E. coli* cells grown under different nutrient conditions, challenged with antibiotics, protein overexpression or depletion, and single gene deletions [16, 17, 5, 18, 19]. Collected surface and volume data span two orders of magnitude and exhibit a single power law in this regime: $S = \gamma V^{2/3}$ (Figure. 3.1 **A**). Specifically, during steady-state growth [5], $\gamma = 6.24 \pm 0.04$, suggesting an elegant geometric relation: $S \approx 2\pi V^{2/3}$. This surface-to-volume scaling with a constant prefactor $\gamma$ is a consequence of tight control of cell aspect ratio $\eta = \frac{L}{W}$ (length/width) (Figure 3.1 **D**), whose mechanistic origin has been puzzling for almost half a century [103, 104]. Specifically, for a sphero-cylindrical bacterium, $S = \gamma V^{2/3}$ implies $\gamma = \eta\pi \left(\frac{\eta\pi}{4} - \frac{\pi}{12}\right)^{-2/3}$. A constant $\gamma$ thus defines a constant aspect ratio $\eta = 4.14 \pm 0.17$ (Figure 3.1 **B**-inset), with a coefficient of variation $\approx 14\%$ (Figure 3.1 **B**).

The surface-to-volume relation for steady-state growth, $S \approx 2\pi V^{2/3}$, results in a simple expression for cell surface-to-volume ratio:

$$S/V \approx 2\pi V^{-1/3} \,. \tag{3.1}$$

Using the phenomenological nutrient growth law $V = V_0 e^{\alpha\kappa}$ [11] (Eq. 1.9), where $\kappa$ is

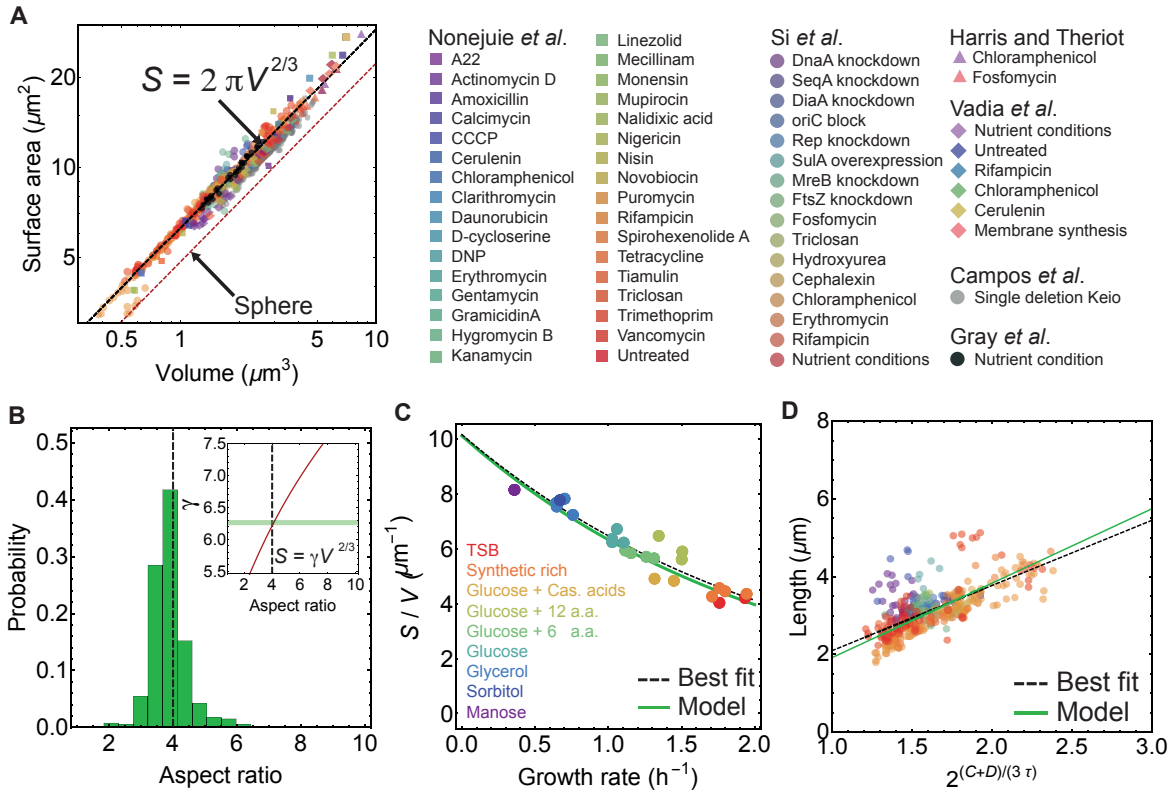


Figure 3.1: **Surface-to-volume scaling in *E. coli* bacteria. A.** *E. coli* cells subjected to different antibiotics, nutrient conditions, protein overexpression/depletion, and single gene deletions [16, 5, 17, 18, 19, 20], follow the scaling relation between population-averaged surface area ($S$) and volume ($V$): $S = \gamma V^{2/3}$ (legend on the right, 5011 data points). Best fit shown in dashed black line for steady-state data from [5] gives $\gamma = 6.24 \pm 0.04$, and a power law exponent $0.671 \pm 0.006$. For single deletion Keio set [19], the best fit curve is $S = 5.79\, V^{2/3}$. **B.** Aspect-ratio distribution for cells growing in steady-state, corresponding to the data in **A** [5]. (Inset) Relationship between $\gamma$ and aspect ratio $\eta$ for a sphero-cylinder (red line). Best fit from **A** shown with horizontal green band gives aspect ratio $4.14 \pm 0.17$. **C.** $S/V$ vs growth rate. Model line uses $S = 2\pi V^{2/3}$ and the nutrient growth law (Eq. 1.9). Data from [5].

Figure 3.1: Continued caption. **D.** Cell length versus $2^{(C+D)/\tau}$. Data used from [5]. Here $C$ is time from initiaton to termination of DNA replication, $D$ is time from termination of DNA replication to cell division, and $\tau$ is doubling time. Green solid line is calculated assuming $S = 2\pi V^{2/3}$ and dashed black line is best fit curve.

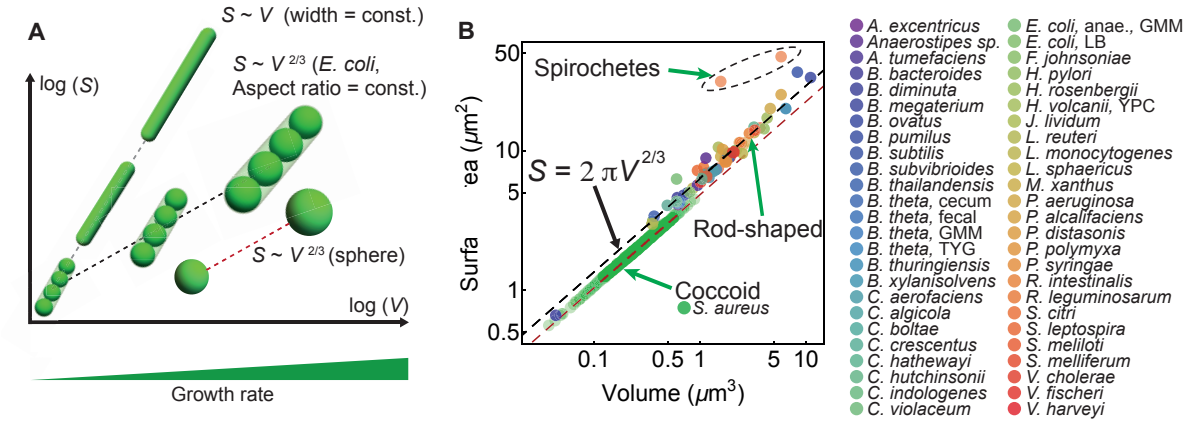


Figure 3.2: **Surface-to-volume scaling in rod-shaped bacteria. A.** $S$-$V$ relation for various bacterial cell shapes. Black dashed line: Small, medium, and large rod-shaped cells with a conserved aspect ratio of 4 follow the relation: $S = 2\pi V^{2/3}$. Gray dashed line: Filamentous cells with constant cell width follow the scaling law: $S \propto V$. Red dashed line: Spheres follow $S \propto V^{2/3}$. **B.** $S$ vs $V$ for 49 different bacterial species [21, 22, 23, 24, 25, 26, 17, 27, 28, 29, 30, 31, 20], and one rod-shaped Archaea (*H. volcanii*). Rod-shaped cells lie on $S = 2\pi V^{2/3}$ line, above the line are Spirochete and below the line are coccoid. For coccoid *S. aureus* exposed to different antibiotics best fit is $S = 4.92\, V^{2/3}$, with preserved aspect ratio $\eta = 1.38 \pm 0.18$. Red dashed line is for spheres.

the population growth rate, a negative correlation emerges between $S/V$ and $\kappa$:

$$S/V \approx 2\pi V_0^{-1/3} \mathrm{e}^{-\alpha\kappa/3}\,, \tag{3.2}$$

with $V_0$ the cell volume at $\kappa = 0$, and $\alpha$ is the relative rate of increase in $V$ with $\kappa$ (Fig. 3.1**C**).

Eq. 3.2 underlies an adaptive feedback response of the cell — at low nutrient conditions, cells increase their surface-to-volume ratio to promote nutrient influx [5, 71]. Prediction from Eq. (3.2) is in excellent agreement with the best fit to the experimental data. Furthermore, a constant aspect ratio of $\approx 4$ implies $V \approx \sqrt{8}W^3$ and $S \approx 4\pi W^2$, where $w$ is the cell width, suggesting stronger geometric constraints than recently proposed [71, 102]. Thus, knowing cell volume as a function of cell cycle parameters [5] we can directly predict cell length under changes in growth media, in agreement with experimental data (Figure 3.1 **D**). We further analysed cell shape data for 48 rod-shaped bacteria, 1 rod-shaped Archaea (*H. vulcanii*), two long spiral Spirochete, and one coccoid bacteria (Fig. 3.2**B**). Collected data for all rod-shaped cells follow closely the relationship $S \approx 2\pi V^{2/3}$, while the long Spirochetes deviate from this curve (Fig. 3.2**A-B**). Coccoid *S. aureus* also follows the universal scaling relation $S = \gamma V^{2/3}$ (with $\gamma = 4.92$), but maintains a much lower aspect ratio $\eta = 1.38 \pm 0.18$ [28] when exposed to different antibiotics (Fig. 3.2**A-B**). Therefore, aspect-ratio preservation likely emerges from a mechanism that is common to diverse rod-shaped and coccoid bacterial species.

### 3.2 Surface-to-volume scaling and aspect ratio conservation in single cells

To investigate how aspect ratio is regulated at the single cell level we analysed the morphologies of *E. coli* cells grown in the mother machine [32] (Fig. 3.3 **A-B**). For five different growth media, mean volume and surface area of newborn cells also follow the relationship $S = 2\pi V^{2/3}$, suggesting that a fixed aspect ratio is maintained on average. In the single-cell data, slight deviation from the 2/3 scaling is a consequence of large fluctuations in newborn cell lengths for a given cell width [67]. Importantly, the probability distribution of aspect ratio is independent of the growth media (Fig. 3.3 **B**), implying that cellular aspect ratio is independent of cell size as well as growth rate.

To explain the origin of aspect ratio homeostasis we developed a quantitative model for cell shape dynamics that accounts for the coupling between cell elongation and the accumulation of cell division proteins FtsZ (Figure 3.3 **C**). The model is thus only applicable to bacteria that divide using the FtsZ machinery. *E. coli* and other rod-like bacteria

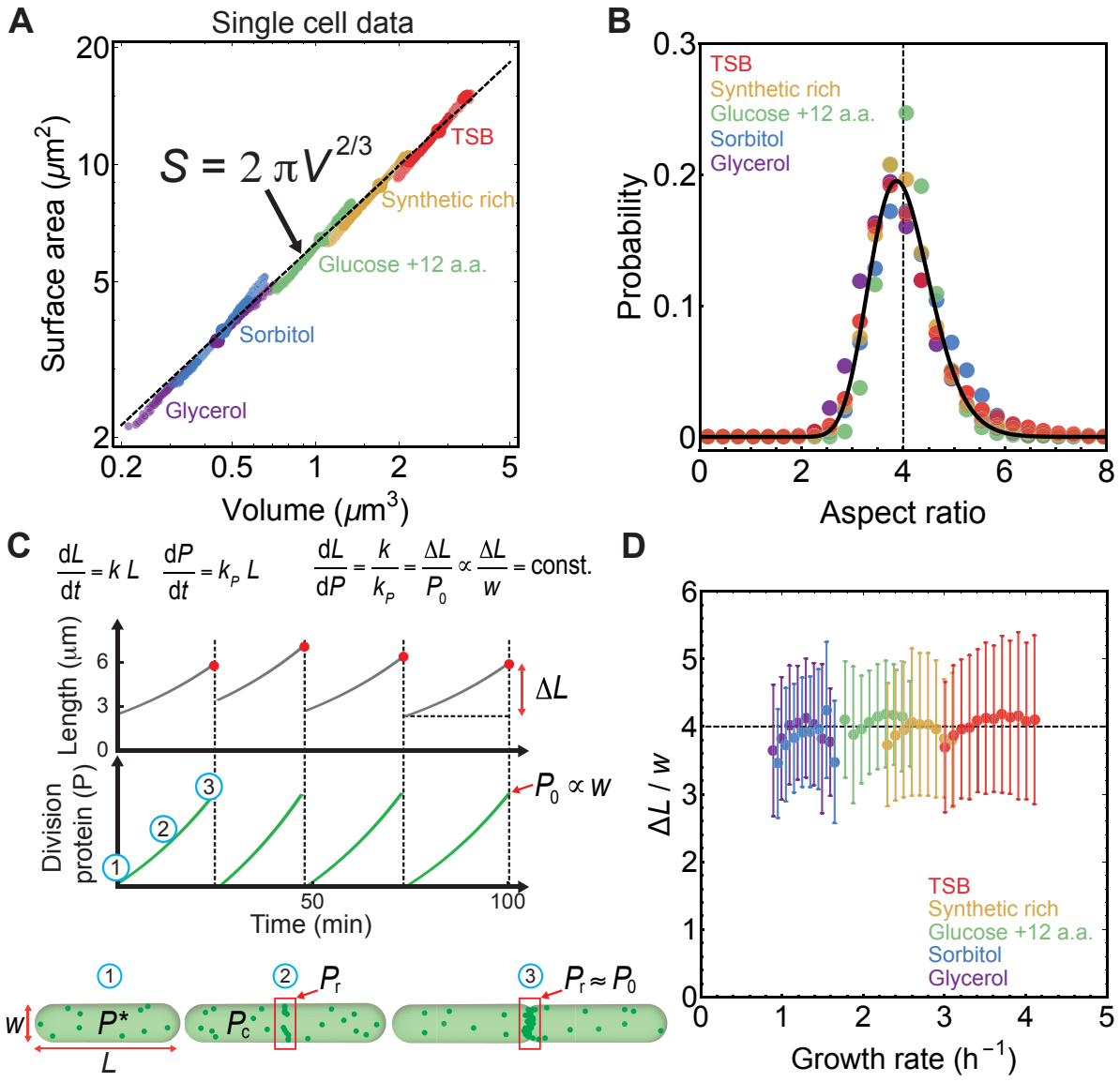


Figure 3.3: **Aspect ratio control in** *E. coli* **at the single cell level. A.** $S$ vs $V$ for newborn *E.coli* cells grown in the mother machine [32]. Single cell data (small circles) binned in volume follow population averages (large circles). **B.** Probability distribution of newborn cell aspect ratio is independent of growth rate, fitted by a log-normal distribution (solid line). **C.** Model schematic. Cell length $L$ increases exponentially during division cycle at rate $k$. Division proteins ($P$) are produced at a rate $k_P$, and assemble a ring in the mid-cell region.

Figure 3.3: Continued caption. At birth, cells contain $P^*$ molecules in the cytoplasm. Amount of FtsZ recruited in the ring is $P_r$. Cells divide when $P_r = P_0 \propto W$, where $W$ is the cell with. $P$ vs time and $L$ vs time are reproduced from model simulations. **D.** Ratio of added length $\Delta L$ and cell width during one cell cycle is constant and independent of growth rate. Error bars $\pm 1$ standard deviation. Note: In simulations, when $P_r$ reaches the threshold $P_0$, the mother cell divides into two daughter cells whose lengths are $0.5 \pm \delta$. Parameter $\delta$ is picked from a Gaussian distribution ($\mu = 0$, $\sigma = 0.05$).

maintain a constant width during their cell cycle while elongating exponentially in length $L$ [105, 32]: $\mathrm{d}L/\mathrm{d}t = kL$, with $k$ the elongation rate. Note that here $k$ is the elongation rate whereas $\kappa$ in Chapter 2 is the volumetric growth rate. Cell division is triggered when a constant length is added per division cycle — a mechanism that is captured by a model for threshold accumulation of division initiator proteins, produced at a rate proportional to cell size [15, 25, 64] - same mechanism as in Chapter 2, with slight variation in the threshold value which will be explained below. While many molecular candidates have been suggested as initiators of division [106], a recent study [12] has identified FtsZ as the key initiator protein that assembles a ring-like structure in the mid-cell region to trigger septation.

Dynamics of division protein accumulation can be described using a two-component model. First, a cytoplasmic component with abundance $P_\mathrm{c}$ grows in proportion to cell size ($\propto L$), as ribosome content increases with cell size [107]. Second, a ring-bound component, $P_\mathrm{r}$, is assembled from the cytoplasmic pool at a constant rate. Dynamics of the cytoplasmic and ring-bound FtsZ are given by:

$$\frac{\mathrm{d}P_\mathrm{c}}{\mathrm{d}t} = -k_\mathrm{b} P_\mathrm{c} + k_\mathrm{d} P_\mathrm{r} + k_P L \ , \tag{3.3}$$

$$\frac{\mathrm{d}P_\mathrm{r}}{\mathrm{d}t} = k_\mathrm{b} P_\mathrm{c} - k_\mathrm{d} P_\mathrm{r} \ , \tag{3.4}$$

where $k_P$ is the constant production rate of cytoplasmic FtsZ, $k_\mathrm{b}$ is the rate of binding of cytoplasmic FtsZ to the Z-ring, and $k_\mathrm{d}$ is the rate of disassembly of Z-ring bound

FtsZ. Note that the division proteins number described by $X$ in Chapter 2 is normalised, therefore varying from 0 to 1 during the cell cycle whereas here the same division proteins are described by non-normalized numbers and therefore called $P$ for distinction, with synthesis rate $k_p$ instead of $\kappa_P$.

At the start of the cell cycle, we have $P_{\rm c} = P^*$ (a constant) and $P_r = 0$. The cell divides when $P_{\rm r}$ reaches a threshold amount, $P_0$, required for the completion of ring assembly. A key ingredient of our model is that $P_0$ scales linearly with the cell circumference, $P_0 = \rho\pi W$, preserving the density $\rho$ of FtsZ in the ring. This is consistent with experimental findings that the total FtsZ scales with the cell width [108]. Accumulation of FtsZ proteins, $P = P_{\rm c} + P_{\rm r} - P^*$, follows the equation: $\mathrm{d}P/\mathrm{d}t = k_P L$, where $k_P$ is the production rate of division proteins, with $P = 0$ at the start of the division cycle. We assume that $k_{\rm b} \gg k_{\rm d}$, such that all the newly synthesized cytoplasmic proteins are recruited to the Z-ring at a rate much faster than growth rate [109]. As a result, cell division occurs when $P = P_0$ (Fig. 3.3**C**). Upon division $P$ is reset to 0 for the two daughter cells. It is reasonable to assume that all the FtsZ proteins are in filamentous form at cell division, as the concentration of FtsZ in an average *E. coli* cell is in the range $4 - 10\mu M$, much higher than the critical concentration $1\mu M$ [110].

From the model it follows that during one division cycle cells grow by adding a length $\Delta L = P_0 k/k_P$, which equals the homeostatic length of newborn cells. Furthermore, recent experiments suggest that the amount of FtsZ synthesised per unit cell length, $\mathrm{d}P/\mathrm{d}L$, is constant [12]. This implies,

$$\frac{\mathrm{d}L}{\mathrm{d}P} = \frac{k}{k_P} = \frac{\Delta L}{P_0} \propto \frac{\Delta L}{W} = const. \tag{3.5}$$

Aspect ratio homeostasis is thus achieved via a balance between the rates of cell elongation and division protein production, consistent with observations that FtsZ overexpression leads to minicells and FtsZ depletion induces elongated phenotypes [111, 112]. Indeed single cell *E. coli* data [32] show that $\Delta L/W$ is constant on average and independent of growth conditions (Figure 3.3 **D**). Furthermore, added length correlates with cell width during one cell cycle implying that the cell width is a good predictor for added

cell length [67].

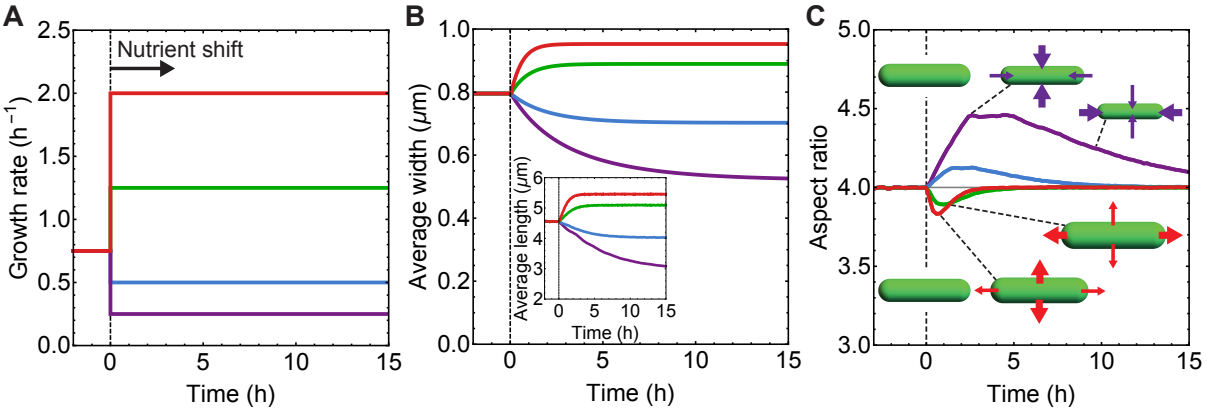


Figure 3.4: **Aspect ratio preservation during nutrient shifts at the single cell level. A-C.** At time $t = 0h$ cells are exposed to nutrient upshift or downshift. Population average of $n = 10^5$ simulated cells. **A.** Growth rate $\kappa$ vs time used as input for simulations. **B.** Population-averaged cell length and width vs time. **C.** Population-averaged aspect ratio of newborn cells vs time. Changes in cell width and length result in a transient increase in aspect ratio during nutrient downshifts, or a transient decrease during nutrient upshifts. Note: When $P_r$ reaches the threshold $P_0$, the mother cell divides into two daughter cells whose lengths are $0.5 \pm \delta$. Parameter $\delta$ is picked from a Gaussian distribution ($\mu = 0$, $\sigma = 0.05$).

### 3.3 Aspect ratio is conserved during nutrient shifts

To predict cell-shape dynamics under perturbations to growth conditions we simulated the single-cell model (Figure 3.4) with an additional equation for cell width derived from a the model proposed by Harris and Theriot [17]: $dS/dt = \beta V$, where $\beta$ is the rate of surface area synthesis relative to the volume. This model leads to an equation for the control of cell width for a sphero-cylinder shaped bacterium, such that $W = 4k/\beta$ at steady-state. It then follows from Eq. 3.5 that the added cell length $\Delta L \propto \frac{k^2}{k_p \beta}$. Note that this model is mechanistically different from the one proposed by Harris and Theriot. In the latter cells accumulate a threshold amount of excess surface area material to

trigger septation, which does not lead to aspect ratio preservation. By contrast, in the model proposed here and in [67] cells divide when they accumulate a threshold amount of division proteins in the Z-ring, proportional to the cell diameter.

We simulated nutrient shift experiments using the coupled equations for cell length, width and division protein production. When simulated cells are exposed to new nutrient conditions, changes in cell width (Figure 3.4 **B**) result in a transient increase in aspect ratio ($\eta = L/W$) during nutrient downshift, or a transient decrease in $\eta$ during nutrient upshift (Figure 3.4 **C**). After nutrient shift, aspect ratio reaches its pre-stimulus homeostatic value over multiple generations. Typical timescale for transition to the new steady-state is controlled by the growth rate of the new medium ($\propto k^{-1}$), such that the cell shape parameters reach a steady state faster in media with higher growth rate. This result is consistent with the experimental observation that newborn aspect ratio reaches equilibrium faster in fast growing media [32].In our model, cell shape changes are controlled by two parameters: the ratio $k/k_p$ that determines the cell aspect ratio and $k/\beta$ that controls the cell width. Nutrient upshifts or downshifts only change the ratio $k/\beta$ while keeping the steady state aspect ratio constant.

### 3.4 Discussion

The conserved surface-to-volume scaling in diverse bacterial species $S \propto V^{2/3}$ is a direct consequence of aspect-ratio homeostasis at the single-cell level. We present a regulatory model (Figure 3.3 **C**) where aspect-ratio control is the consequence of a constant ratio between the rate of cell elongation ($k$) and division protein accumulation ($k_P$). Deviation from the homeostatic aspect ratio is a consequence of altered $k/k_P$, as observed in filamentous cells, FtsZ or MreB depleted cells ([67]).

These results suggests that cell width is an essential shape parameter for determining cell length in *E. coli*. This is to be contrasted with *B. subtilis*, where cell width stays approximately constant across different media, while elongating in length [113]. However, FtsZ recruitment in *B. subtilis* is additionally controlled by effector UgtP, which localises to the division site in a nutrient-dependent manner and prevents Z-ring assembly [114]

[115]. This can be interpreted as a reduction in $k_P$ with increasing $k$, within the framework of our model. As a result, *B. subtilis* aspect ratio ($\propto k/k_P$) is predicted to increase with increasing growth rate.

Aspect ratio control may have several adaptive benefits. For instance, increasing cell surface-to-volume ratio under low nutrient conditions can result in an increased nutrient influx to promote cell growth (Figure 3.3 **C**). Under translation inhibition by ribosome-targeting antibiotics, bacterial cells increase their volume while preserving aspect ratio [17, 5]. This leads to a reduction in surface-to-volume ratio to counter further antibiotic influx - Chapters 4. Furthermore, recent studies have shown that the efficiency of swarming bacteria strongly depends on their aspect ratio [116, 117]. The highest foraging speed has been observed for aspect ratios in the range 4-6 [116], suggesting that the maintenance of an optimal aspect ratio may have evolutionary benefits for cell swarmers.

# Chapter 4

# Control of bacterial growth and cell morphology under antibiotic stress

Bacteria have evolved to develop multiple strategies for antibiotic resistance by effectively reducing intracellular antibiotic concentrations or antibiotic binding affinities, but the role of cell morphology on antibiotic resistance remains poorly characterized. By analyzing cell morphological data of different bacterial species under antibiotic stress, we find that bacterial cells robustly reduce surface-to-volume ratio in response to most types of antibiotics. Using quantitative modelling we show that by reducing surface-to-volume ratio, bacteria can effectively reduce intracellular antibiotic concentration by decreasing antibiotic influx. Using the particular example of ribosome-targeting antibiotics, I present a systems-level model for the regulation of cell shape under antibiotic stress, and discuss feedback mechanisms that bacteria can harness to increase their fitness in the presence of antibiotics.

---

Part of this chapter is published in Serbanescu, D., Ojkic, N., & Banerjee, S. (2020). Nutrient-dependent trade-offs between ribosomes and division protein synthesis control bacterial cell size and growth. *Cell reports*, 32(12), 108183. [65] and in Ojkic, N., Serbanescu, D., & Banerjee, S. (2019). Surface-to-volume scaling and aspect ratio preservation in rod-shaped bacteria. *Elife*, 8, e47033. [67] Nikola Ojkic did the shape analysis in Figure 4.1 and developed the theoretical analysis in section 4.1.

Antibiotic resistance is one of the major threats to human society. It has been estimated that each year 700,000 people die as a consequence of infections caused by resistant bacteria, prompting urgent response in order to prevent devastating global effects within generations [118]. To understand the mechanisms of antibiotic resistance we need to better understand how antibiotics physically penetrate bacterial cells, how antibiotics bind to their targets, what damage antibiotics cause to bacterial physiology and ultimately how this damage leads to cell death [119, 120]. To become antibiotic resistant, bacteria have developed multiple strategies. Resistance is commonly attained via a reduction in the intracellular concentration of the antibiotic or by reducing antibiotic binding affinities to their specific intracellular targets [121]. Various different pathways to antibiotic resistance have been described [122] including decrease in antibiotic influx by reduction in porin expression [123], modulation of membrane lipid composition [124], induction of horizontal gene transfer [125], increase in antibiotic efflux by increasing efflux pump expression [126], SOS response [127], and direct inactivation of antibiotics [128]. However, the role of cell size, shape and growth physiology on antibiotic resistance remains poorly understood.

Recent studies have shown that bacteria undergo a wide variety of cell morphological changes in response to antibiotics [129, 16, 130, 17, 131, 67, 132]. These morphological changes commonly occur via changes in cell size, surface-to-volume ratio or curvature [16, 17, 132]. For instance, Gram-negative *E. coli*, *C. crescentus* and Gram-positive *L. monocytogenes* decrease their surface-to-volume ratio ($S/V$) upon treatment with ribosome-inhibitory and cell-wall targeting antibiotics [17]. It has also been shown that the Gram-negative human pathogen *P. aeruginosa* make a transition from rod-shaped cells to spherical cells upon treatment with $\beta$-lactams [130]. However, it is not clear if these shape changes represent a passive physiological response to biochemical changes caused by the antibiotic, or if these are active shape changes that promote bacterial fitness for surviving antibiotic exposure. While the role of cell shape on bacterial growth, nutrient uptake and motility have been hypothesized [35], the effect of cell shape on an-

tibiotic resistance remains largely unknown. It remains unclear whether different classes of antibiotics that target distinct cellular components and physiological processes would increase or decrease $S/V$.

## 4.1 Antibiotic-induced cell shape changes in rod-shaped bacteria

To understand the effect of antibiotics on bacterial cell shape, we first analysed the morphological data for *E. coli* cells treated with 42 antibiotics belonging to 5 different categories based on their binding targets [16]. Surprisingly, all antibiotics decrease $S/V$ except membrane- and membrane transport-targeting antibiotics that increase $S/V$. Similarly, decrease in $S/V$ was previously observed in cells treated with cell-wall targeting antibiotics (A22, mecillinam, fosfomycin) [137], and increase in $S/V$ for the membrane targeting antibiotic cerulenin [18]. The Gram-negative *A. baumannii* also decreases $S/V$ for most antibiotics, including the membrane targeting antibiotic triclosan (Figure 4.1 **B**). For Gram-positive *B. subtilis* with thick, less plastic cell-envelope [31, 138], $S/V$ decreases for all groups of antibiotics (Figure 4.1 **C**) [136]. To understand the implications of these data, we note that $S/V$ is one of the key physical parameters that regulates nutrient influx and waste efflux [35], as well as the influx/efflux of antibiotics.

To quantitatively understand the role of $S/V$ in regulating antibiotic flux across the cell membrane, we developed a mathematical model of antibiotic transport into a rod-shaped bacterial cell, with binding/unbinding interactions with its specific target [139]. To quantify the effect of $S/V$ reduction on intracellular antibiotic dilution, we introduce the antibiotic dilution factor $\delta$:

$$\delta \equiv \frac{|\Delta a_{in}|}{a_{out}} , \tag{4.1}$$

defined as the absolute change in the intracellular antibiotic concentration ($\Delta a_{in}$) relative to the extracellular concentration, as $S/V$ is varied between a chosen minimum ($(S/V)_{min}$) and a maximum value ($(S/V)_{max}$). The dilution factor is thus dependent on the variation in $S/V$, growth rate $\kappa$, influx permeability $P_{in}$ and outflux permeability $P_{out}$. The maximum dilution is obtained for $P_{out} = 0$, while a lesser dilution is obtained for a

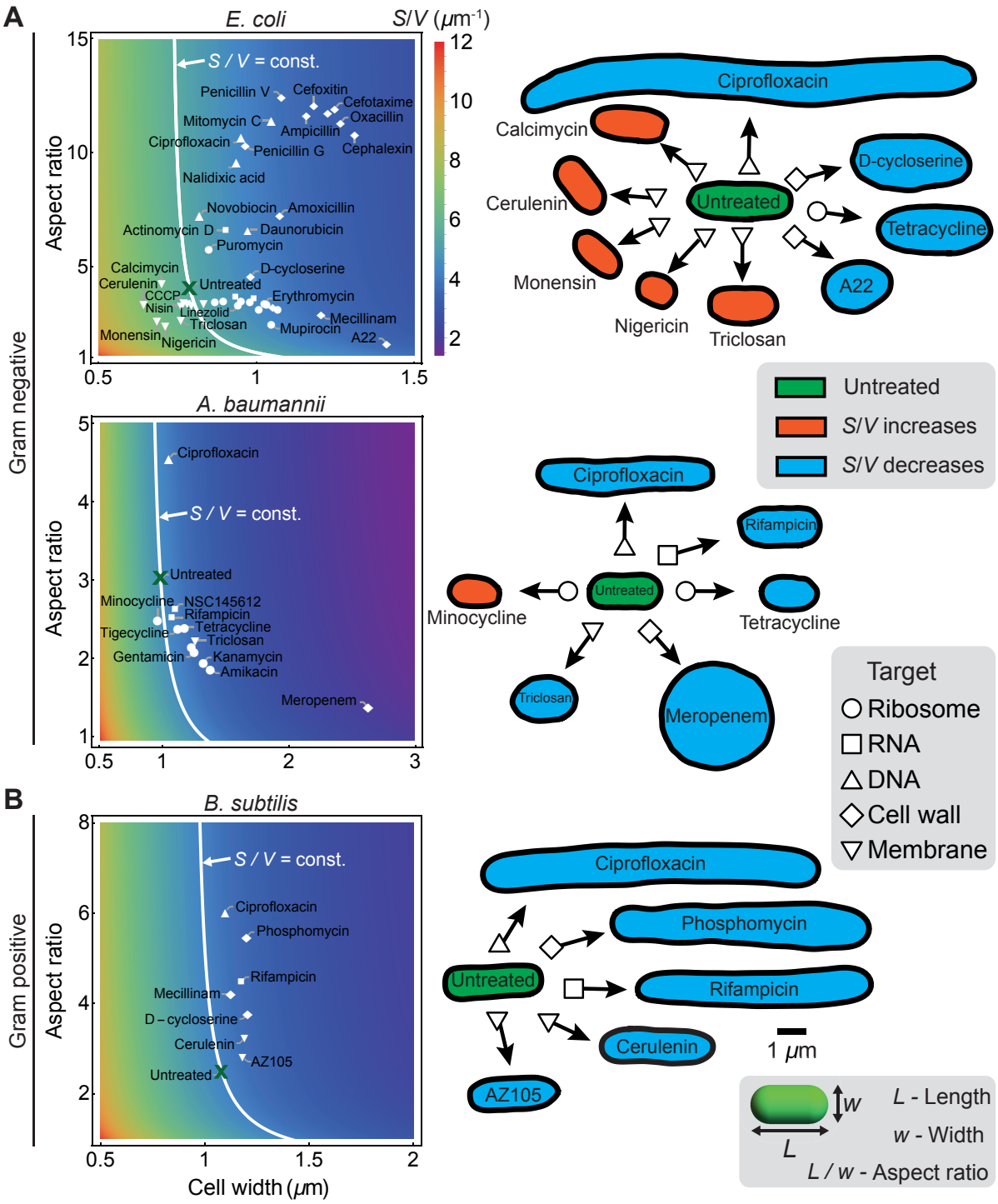


Figure 4.1: **Changes in cell shape and surface-to-volume ratio of rod-shaped bacteria under different antibiotics.**

Figure 4.1: Continued caption. Left: Heatmap of cell surface-to-volume ratio ($S/V$) as a function of cell width and aspect ratio, overlayed with experimental data for population averaged cell shape under antibiotic treatments targeting different cellular components: ribosomes, RNA, DNA, cell wall, and membranes. White lines represent constant $S/V$ corresponding to untreated cells. Right: Typical cell contours for morphological response to antibiotic treatments. $S/V$ increase shown in red, decrease in blue, and untreated cells in green. Data are taken from refs [16, 133, 134]. Cell contours are extracted using ImageJ plugin JFilament [135] . **A.** $S/V$ for Gram-negative *E. coli* and *A. baumannii* as a function of cell width and cell aspect ratio. *E. coli* decrease $S/V$ for all antibiotics apart from membrane targeting ones for which $S/V$ increases. *A. baumannii* decreases $S/V$ for all antibiotics apart for ribosome targeting Minocycline for which $S/V$ slightly increases. **B.** $S/V$ for gram-positive *B. subtilis* decreases for all antibiotics [136].

higher $P_{out}$. To determine the maximum dilution due to shape variations, we optimize $P_{in}$ and $\kappa$ for $P_{out} = 0$:

$$\delta_{max} = \frac{\sqrt{\left(\frac{S}{V}\right)_{max}} - \sqrt{\left(\frac{S}{V}\right)_{min}}}{\sqrt{(SV)_{max}} + \sqrt{(SV)_{min}}} \,. \tag{4.2}$$

Thus, the maximum value of the dilution factor is dependent only on the surface-to-volume ratios before and after antibiotic application. Eq. 4.2 predicts a maximum $\approx 15\%$ dilution in intracellular antibiotic concentration for cephalexin treated *E. coli*, where $(S/V)_{\max}$ and $(S/V)_{\min}$ are taken to be the surface-to-volume ratios for the untreated cell and the antibiotic-treated cell, respectively. Similarly, meropenam treated *A. baumannii* cells undergo a maximum of 22% dilution in intracellular antibiotic concentration. Antibiotic dilution mediated by changes in $S/V$ could provide a significant fitness advantage for antibiotics with steep growth-inhibition curves [115, 140], since a small decrease in antibiotic concentration via shape variation could lead to a significant increase in the bacterial growth rate.

## 4.2 Mechanisms of cell shape changes by antibiotic action

The mechanisms by which antibiotics induce cell shape changes are specific to the type of antibiotic treatment [16]. While DNA-targeting antibiotics induce SOS response that in turn inhibits cell division causing cell filamentation [16, 115], cell-wall targeting antibiotics such as $\beta$-lactams induce various cell shapes and sizes [139] and cell bulging [129]. Ribosome-targeting antibiotics on the other hand induce a less complex variety of shape changes [5, 17, 132]. Here I specifically focus on the case of ribosome-targeting antibiotics, for which the biochemical reactions are well characterized [141], in order to elucidate the dynamic coupling between cell shape, growth rate and antibiotic concentration.

## 4.3 Model for cell growth and shape dynamics under the action of ribosome-targeting antibiotics

Under translation inhibition by ribosome-targeting antibiotics, decrease in cell volume in nutrient-rich media (Chapter 2) is indicative of a higher surface-to-volume ratio that may increase the influx of nutrients and antibiotics. Conversely, in poor media, increase in cell volume may be indicative of a lower surface-to-volume ratio that in turn would reduce antibiotic and nutrient influx (Figure 2.3 **F**). Therefore, surface-to-volume ratio of a cell may play a crucial role in controlling cellular adaptive response to growth perturbations, by modulating the relative contributions of nutrient and antibiotic influx rates. To test the role of surface-to-volume ratio on bacterial growth, we construct a model coupling cell growth and geometry to nutrient and antibiotic transport.

**Nutrient dynamics** – The dynamics of nutrient concentration inside the cell, $[n]$, is given by:

$$\frac{d[n]}{dt} = J_n - \kappa[n] - \kappa_r r_a \tag{4.3}$$

where $J_n = [n_{\text{ext}}]P_{\text{in}}A/V$ is the nutrient influx, $[n_{\text{ext}}]$ is the nutrient concentration in the extracellular medium, $P_{\text{in}}$ is the cell envelope permeability and $\kappa_r$ is the rate at which ribosomes are produced from the nutrients. The model for nutrient transport across the cell membrane is consistent with the one proposed in [95] if we assume that the num-

ber of metabolic proteins (transporters) scales with the surface area of the cell. The interplay between nutrients and ribosome synthesis is schematically represented in Figure 4.2 **A**. The intracellular concentration of nutrients determines the specific growth rate as: $\kappa_{\text{specific}} = \kappa_0[n]/([n] + n^*)$ [142] (Eq.1.1), where $\kappa_0$ is the maximum growth rate characteristic of the medium, and $n^*$ is the value of $[n]$ when $\kappa_{\text{specific}}/\kappa_0 = 0.5$. When the nutrients inside the cell reach saturation, i.e. $\mathrm{d}[n]/\mathrm{d}t = 0$, $\kappa = \kappa_{\text{specific}}$.

**Antibiotic dynamics** – The action of ribosome-targeting antibiotics is illustrated using the diagram in Figure 4.2 **A**, which consists of two key components: the flux of antibiotics $J_a$ entering the cell, and the binding of antibiotics to the active pool of ribosomes, $r_a$. The dynamics are described by the following set of equations, extending the model of Elf *et al.* [143] and Greulich *et al.* [144],

$$\begin{cases} da_{\text{in}}/dt &= -\kappa a_{\text{in}} + f(r_a, r_b, a_{\text{in}}) + J_a(a_{\text{ex}}, a_{\text{in}}, A, V), \\ dr_a/dt &= -\kappa r_a + f(r_a, r_b, a_{\text{in}}) + s, \\ dr_b/dt &= -\kappa r_b - f(r_a, r_b, a_{\text{in}}), \end{cases} \tag{4.4}$$

where $a_{\text{ex}}$ is the extracellular antibiotic concentration, $a_{\text{in}}$ is the intracellular concentration of the antibiotic, $r_a$ is the concentration of the active pool of ribosomes in the cell, $r_b$ is concentration of the pool of ribosomes bound by the antibiotics, and $s$ is the rate of synthesis of ribosomes. Unlike previous models [143, 144], here we account for the dependence of $J_a$ on cell shape as:

$$J_a(a_{\text{ex}}, a_{\text{in}}, S, V) = (P_{\text{in}} a_{\text{ex}} - P_{\text{out}} a_{\text{in}}) \frac{S}{V}, \tag{4.5}$$

where $P_{\text{in}}$ and $P_{\text{out}}$ are the cell envelope permeabilities in the inward and outward directions, respectively. The ribosome-antibiotic interactions are defined by: $f(r_a, r_b, a_{\text{in}}) = -k_{\text{on}} a_{\text{in}}(r_a - r_{\text{min}}) + k_{\text{off}} r_b$, where $k_{\text{on}}$ is the rate of binding of antibiotics to ribosomes, and $k_{\text{off}}$ is the rate of unbinding. These rate constants for Chloramphenicol are known from literature [143, 144]. Furthermore, cells produce more ribosomes to compensate for the inactive ribosomes bound by antibiotics [10]. This is captured by the source term:

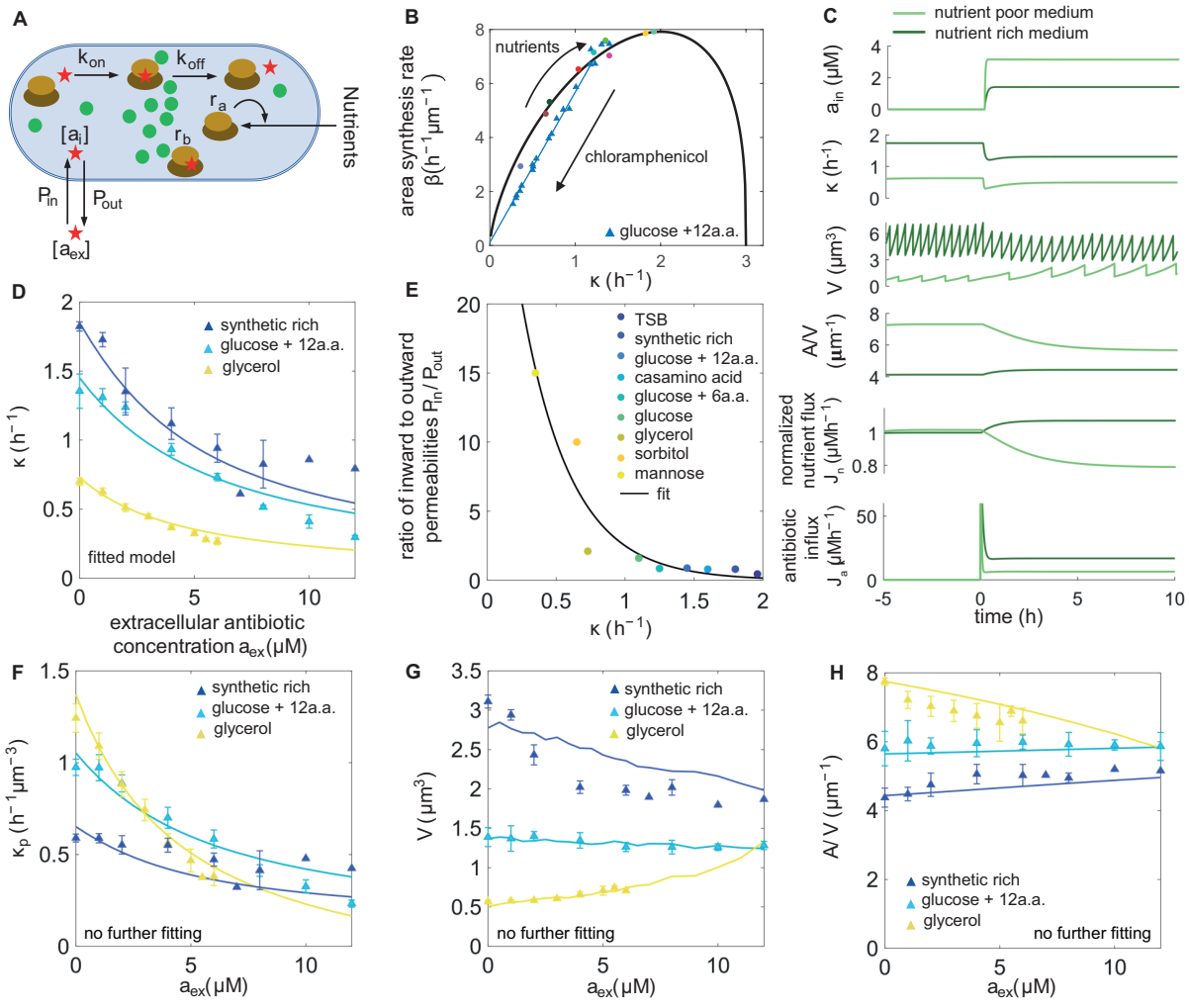


Figure 4.2: **Cell shape control under translational inhibition. A.** Schematic illustrating nutrient and antibiotic transport across cell surface and antibiotic interactions inside the cell. **B.** Model predictions for the surface area synthesis rate ($\beta$) as a function of the growth rate ($\kappa$) for varying nutrient conditions, and its inhibition under Chloramphenicol perturbations. $\beta$ is calculated using $\beta = \kappa A/V$. **C.** Single-cell simulations of growth in response to a step pulse of Chloramphenicol applied at $t = 0$ h in the extracellular medium. Top to bottom: Dynamics of intracellular antibiotic concentration, growth rate, cell volume, surface-to-volume ratio, normalized nutrient and antibiotic flux. Both nutrient and antibiotic fluxes are higher in rich media due to the increase in surface-to-volume ratio.

Figure 4.2: Continued caption. **D.** Model growth inhibition curves fitted to experimental data [9], in order to deduce the ratio of inward to outward cell-surface permeability. Data are represented as mean ± SEM. **E.** $P_{\text{in}}/P_{\text{out}}$ increases with decreasing growth rate (quality of nutrients). We used an exponential fit to calibrate $P_{\text{in}}/P_{\text{out}}$ for different nutrient conditions. **F-H.** Simulation results for the dependence of $\kappa_p$ (F), average cell volume $V$ (G), and average cell surface-to-volume ratio $S/V$ (H) on Chloramphenicol concentration, plotted against experimental data [9] at three different nutrient conditions. Data are represented as mean ± SEM. See Tables 1 and 2 for a complete list of parameter values. Note: We introduce noise in the division ratio $D_R$ such that $V_{i+1}(t=0) = D_R V_i(t=\tau_i)$, where $V_{i+1}(t=0)$ is the volume of the cell in generation $i+1$ at birth, $V_t(t=\tau_i)$ is the volume of the cell in generation $i$ at division, $\tau_i$ is the division time and $D_R$ is a Gaussian random variable with mean 0.5 and standard deviation 0.05.

---

$s = \kappa[r_{\max} - \kappa\Delta r(1/\kappa_{\text{specific}} - 1/\kappa_t\Delta r)]$, where $\Delta r = r_{\max} - r_{\min}$.

**Cell shape dynamics** – Having described the dynamics of cell volume (Eq. 2.1), division control (Eq. 2.2), nutrient and antibiotic transport (Eq. 4.3-4.4), we need to additionally account for cell surface area synthesis to predict cell shape changes. We assume that rate of synthesis cell surface area is proportional to cell volume [145]:

$$\frac{\mathrm{dS}}{\mathrm{d}t} = \beta V(t) \ , \tag{4.6}$$

where $\beta$ is the rate of surface area production, which depends on cell shape, growth rate and division protein synthesis rate. Solving Eq. (2.1) and Eq. (4.6), one obtains $S/V = \beta/\kappa$, at steady-state [145]. In Chapter 3 we show that *E. coli* cells obey the relation: $S = \nu V^{2/3}$, under nutrient and translational perturbations, where $\nu$ is a geometric factor related to the cell aspect ratio $\eta$ as: $\nu = \eta\pi(\frac{\eta\pi}{4} - \frac{\pi}{12})^{-2/3}$. Therefore, surface area production rate varies non-monotonically with growth rate as: $\beta = \nu\kappa(\kappa/\kappa_p)^{-1/3}$ (Figure 4.2 **B**).

Taken together, the model accounts for the key functions of ribosomes in controlling

cell growth rate ($\kappa$), rate of production of division proteins ($\kappa_p$), and the rate of surface area synthesis ($\beta$). Under translation inhibition, both $\kappa$ and $\kappa_p$ decreases as shown in Figures 2.3 **A** and **C**. Surface area production rate is also impacted by translation inhibition, as shown in Figure 4.2 **B**, albeit in a different manner from the growth rate. Differential reduction of $\kappa$ and $\beta$ under translation inhibition is indicative of changes in steady-state cell surface-to-volume ratio ($\propto \beta/\kappa$). To test this quantitatively, we simulated the coupled equations (Appendix in Chapter 7) for single-cell growth (Eq. 2.1, 2.2 and 4.6), nutrient (Eq. 4.3) and ribosome-antibiotic dynamics (Eqs. 4.4) under stresses induced by ribosome-targeting antibiotics (Figure 4.2 **C**). In response to a step pulse of antibiotic in a rich nutrient medium at $t = 0h$, the concentration of antibiotic inside the cell and the influx increase rapidly. This in turn reduce cell elongation rate as a result of antibiotic binding to ribosomes, and leads to longer interdivision times, a decreased (increased) average birth volume and a concomitant increase (decrease) in surface-to-volume ratio for cells growing in rich (poor) nutrients. These results confirm our hypotheses that in poor media, cells reduce their surface-to-volume ratio to inhibit antibiotic influx, while in rich media cells increase their surface-to-volume ratio to import more nutrients.

While all the model parameters can be calibrated from available experimental data (Tables 7.1, 7.2 and 7.3, Methods in Chapter 7), the relative magnitude of the permeabilities, $P_{\text{in}}/P_{\text{out}}$ remains undetermined. To this end, we fit our model to the experimental growth-inhibition curves [9] in differents nutrient conditions (Figure 4.2 **D**), treating $P_{\text{in}}/P_{\text{out}}$ as a fitting parameter. Interestingly, we find that $P_{\text{in}}/P_{\text{out}}$ is nutrient-dependent and decreases with increasing specific growth rate (Figure 4.2 **E**). As a result, $J_n/J_a$ is an increasing function of growth rate, such that nutrient influx dominates over antibiotic influx in nutrient rich media. Incorporating nutrient-dependent regulation of membrane permeability, our model predictions capture the experimental data for the decrease in division protein synthesis rate under Chloramphenicol inhibition (Figure 4.2 **F**) and the changes in cell volume (Figure 4.2 **G**). Consistent with our hypothesis and experimental data, we find that cell surface-to-volume increases in rich nutrient media (synthetic rich

in experiments) (Figure 4.2 **H**). Conversely, in poor nutrient medium (glycerol in experiments), cell surface-to-volume reduces with increasing drug dosage, suggesting that cells are countering the influx of antibiotics if sufficient nutrients are not available.

Nutrient-dependent regulation membrane permeability to antibiotics (Figure 4.2 **E**) can be a result of different metabolic pathways. It has been observed that *E.coli* cells have different metabolic pathways for nutrients depending on the growth conditions [146]. Furthermore, if the cells are subjected to a nutrient downshift, the proteome reallocates such that a larger fraction of proteins is allocated to the sector responsible for carbon catabolism which in turn reduces the available proteome fraction for other sectors [147, 148]. The transition from one metabolic mechanism to another can be justified using a proteome allocation model as suggested by Basan *et al.* [148] and Mori *et al.* [147], or by increasing the glucose uptake rates. The drop in cell envelope permeability that we observe around $\kappa = 0.6\ \mathrm{h}^{-1}$ (Figure 4.2 **E**) matches the maximum growth rate that *E.coli* cells can achieve while staying below the critical limit on energy dissipation [149].

## 4.4 Role of cell shape bacterial growth inhibition by antibiotics

Our theory predicts that bacterial growth response to translation-inhibitory antibiotics is governed by nutrient-dependent cell shape changes (Figures 2.3 and 4.2). To systematically study how bacterial growth inhibition depends on cell shape and nutrient quality, we simultaneously perturbed cell shape and ribosomal translation in varying growth media using our computational model. These simulations can be realised experimentally by simultaneously applying two antibiotics - one that changes cell shapes (e.g. by targeting the cell wall), while the other affects the translational machinery by inhibiting ribosomal activity. The resultant effect can be suppressive, antagonistic, or synergistic depending on what the combined effect of the two drugs is with respect to the individual effect of each [150, 151].

In simulations we simultaneously applied a surface area *modifier* and chloramphenicol to a cell growing at steady-state. To achieve rounder cells, the *modifier* is a surface area synthesis inhibitor that decreases the surface production rate $\beta$, by decreasing the cell's

geometric factor $\nu$ ($= S/V^{2/3}$), which in turn reduces cellular aspect ratio. By contrast, long filamentous cells are obtained when a surface area promoter is added (increasing $\nu$), leading to higher aspect ratio cells.

We investigated the response of growth rate to increasing Chloramphenicol concentrations for cells with varying aspect ratios – ranging from $\eta = 1$ for coccoidal cells to $\eta = 10$ for filamentous cellsFigure 4.3 **A**. The response of $\kappa$ to the concentration of the applied antibiotic can be characterized by a Hill function of the form [152] (Figure 4.3 **A**):

$$\kappa(a_{\text{ex}}) = \frac{\kappa_{\text{specific}}}{1 + (\frac{a_{\text{ex}}}{\text{IC}_{50}})^n} \ , \tag{4.7}$$

where $\text{IC}_{50}$ is the half-inhibitory concentration of the antibiotic, and the Hill coefficient $n$ quantifies the dose-sensitivity of the growth rate to relative changes in drug concentration. We take $\text{IC}_{50}$ as a measure of drug *resistance* [152].

For a range of aspect ratios and nutrient conditions, we fitted the growth inhibition curves to the Hill function in Eq. (4.7), and obtained the values for $\text{IC}_{50}$ (Figure 4.3 **B**) and the dose-sensitivity $n$ (Figure 4.3 **C**). Our model predicts that $\text{IC}_{50}$ (resistance) increases with decreasing aspect ratio in rich-nutrient medium, while being less sensitive to changes in cell aspect ratio in poor-nutrient medium (Figure 4.3 **B**). Dose-sensitivity to changes in drug concentration increases with decreasing aspect ratio and increasing nutrient quality (Figure 4.3 **C**), such that dose-sensitivity is positively correlated with drug resistance (Figure 4.3 **D**). These results indicate that cellular response to translation inhibitory antibiotics is sensitive to both the nutrient quality as well as cell shape. We find that round coccoidal cells are most drug-resistant, while filamentous cells are least resistant (Figure 4.3 **E**). Furthermore, depending on nutrient-quality, cellular morphological response to translation inhibitory drugs is different. While cells increase their surface-to-volume ratio to import more nutrients in nutrient-poor medium, cells prefer to reduce their surface-to-volume ratio in rich-nutrient medium to inhibit antibiotic influx (Figures 3.3 and 4.2). These findings predict that bacterial growth inhibition can be maximized by simultaneously inhibiting ribosomal translation and promoting surface area production in nutrient-poor media.

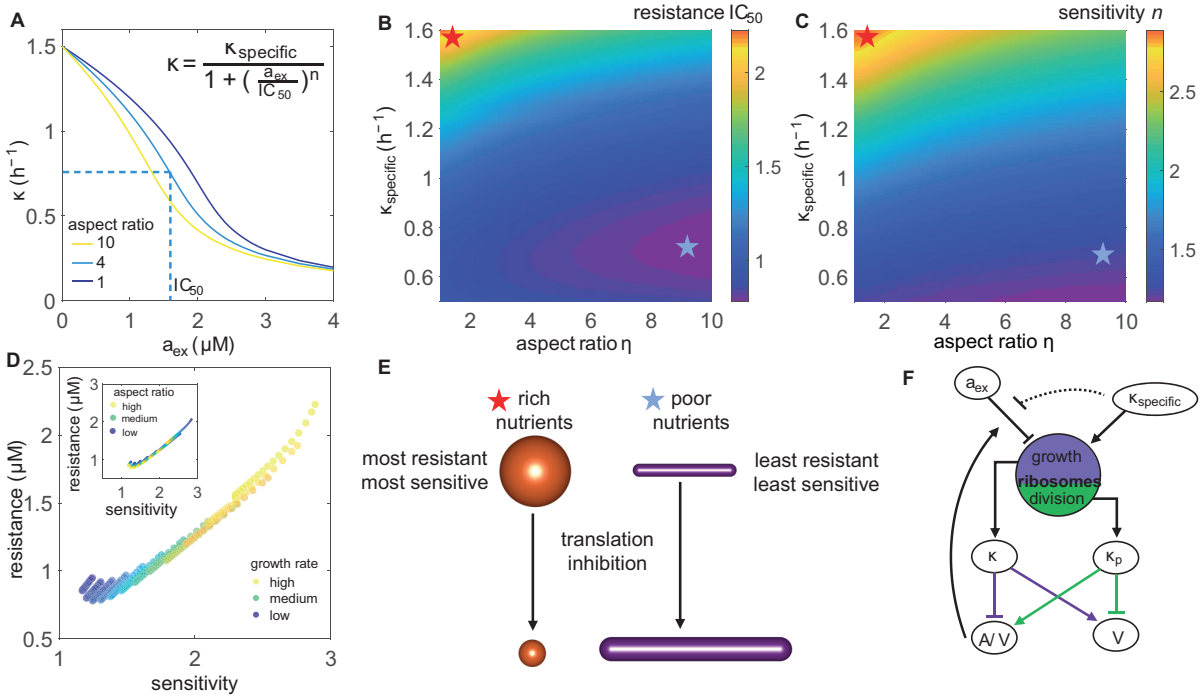


Figure 4.3: **Cell shape and nutrient quality control bacterial resistance to ribosome-targeting antibiotics**. **A.** Growth inhibition curves for three different values of cell aspect ratio in a nutrient-rich medium. Dashed line corresponds to $IC_{50}$ on the x-axis, the concentration of antibiotic when the growth rate reduces by half. **B.** Heatmap of $IC_{50}$, a metric for drug resistance, showing the effects of changing aspect ratio and nutrient quality. Red asterix: Maximally resistant, blue asterix: least resistant. **C.** Heatmap of drug dose-sensitivity ($n$), showing the effects of changing cellular aspect ratio and nutrient quality of the growth medium. **D.** Correlation between drug resistance and dose-sensitivity under changes in nutrient quality ($\kappa_{\text{specific}}$). Inset: Correlation between drug resistance and dose-sensitivity under changes in aspect-ratio. **E.** Schematic illustrating fitness value for cell shapes and morphological changes that accompany bacterial response to translation inhibition in nutrient-rich and nutrient-poor growth media. **F.** Schematic representation of the feedback pathways that connect ribosomal translation to bacterial cell shape, growth, nutrient and antibiotic transport. See Tables 7.1, 7.2 and 7.3 for a complete list of parameter values.

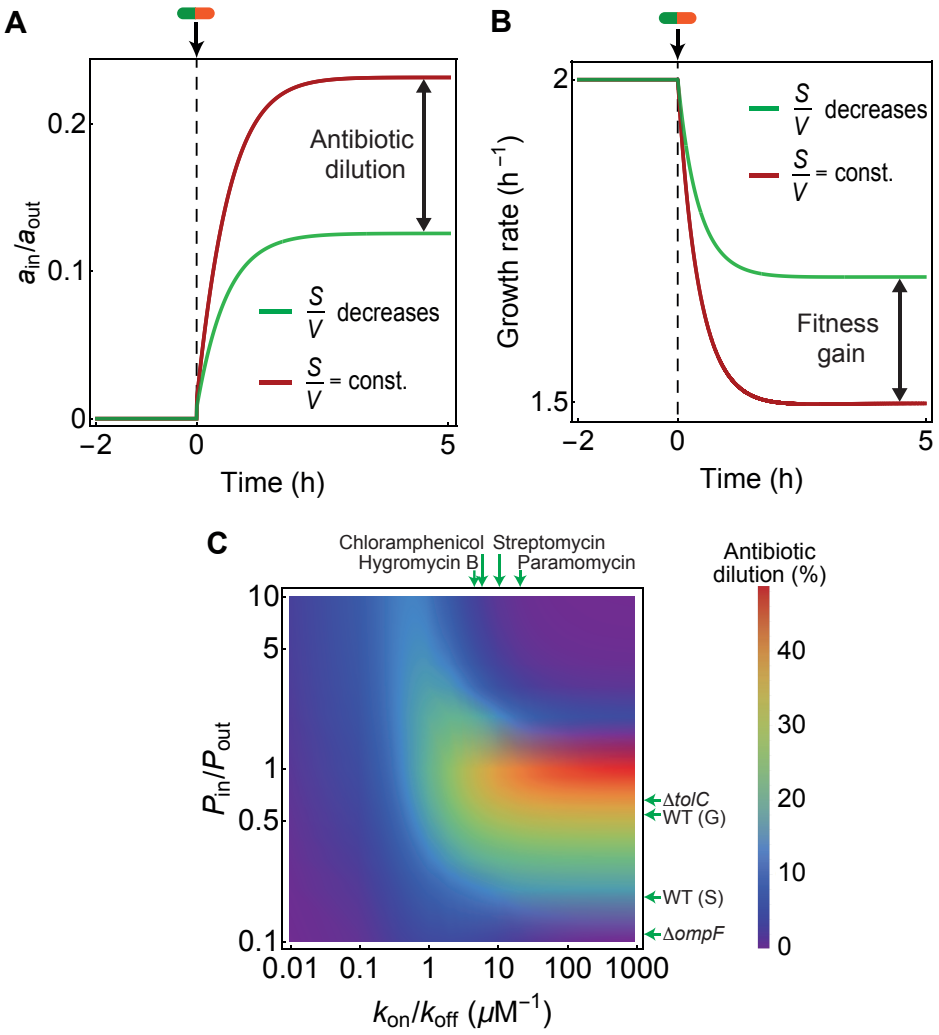


Figure 4.4: **Role of cell shape changes on antibiotic dilution. A.** Relative antibiotic concentration inside the cell vs time obtained by model simulations for two cases: (i) $S/V$ = const. = 5 $\mu m^{-1}$ (red), (ii) $S/V$ decreases from 5 to 3 $\mu m^{-1}$ (green) via the pathway shown in Figure 4.3. Here $a_{\text{out}} = 5$ $\mu$M and $P_{\text{in}}/P_{\text{out}} = 1$. **B.** Bacterial growth rate vs time obtained from simulations for two different cases as in panel **A**. The decrease in $S/V$ results in fitness gain. **C** Heat map of antibiotic dilution factor predicted from simulations as functions of membrane permeability ratios ($P_{\text{in}}/P_{\text{out}}$) and the ratio of antibiotic-ribosome binding and unbinding rates ($k_{\text{on}}/k_{\text{off}}$). Antibiotic dilution was calculated when bacterial $S/V$ was altered from 15 to 3 $\mu m^{-1}$.

Figure 4.4: Continued caption. Membrane permeability ratios shown with horizontal arrows were estimated (Supplementary material [139]) for growing wild-type, WT (G), and stationary wild type *E. coli* cells, WT (S), OmpF porin deficient ($\Delta ompF$) and efflux-pump deficient ($\Delta tolC$) cells [153]. Experimentally measured $k_{\rm on}/k_{\rm off}$ values for different ribosome-targeting antibiotics are shown with vertical arrows [154, 155, 156].

## 4.5 Impact of cell shape changes on antibiotic dilution

We used the whole-cell model for cell growth under antibiotic action to estimate the amount of antibiotic dilution due to cell shape changes. To this end, I simulated a whole-cell model of bacterial growth that evolved the dynamics of cell size, shape and protein synthesis, coupled to the kinetics of antibiotics binding to and unbinding from ribosomes just as before in the "Nutrient dynamics" and "Antibiotic dynamics" sections of this Chapter (Figure 4.2). Using parameters bench-marked for *E. coli* cells, under conditions when $S/V$ remains unchanged, the intracellular antibiotic concentration is higher and the growth rate is lower compared to the case where $S/V$ spontaneously decreased over time (Figure 4.4 **A-B**). The simulations revealed that the maximum antibiotic dilution was obtained for antibiotics with high affinity constants ($k_A = k_{\rm on}/k_{\rm off} > 1\mu{\rm M}^{-1}$) typical for aminoglycosides: Hygromycin B ($k_A = 5\,\mu{\rm M}^{-1}$), Chloramphenicol ($k_A = 5.8\,\mu{\rm M}^{-1}$), Streptomycin ($k_A = 10\,\mu{\rm M}^{-1}$), and Paromomycin ($k_A = 19\,\mu{\rm M}^{-1}$). Depending on the ratio of the membrane permeability constants ($P_{\rm in}/P_{\rm out}$), the antibiotic dilution factor is non-monotonic and reaches a maximum for $P_{\rm in}/P_{\rm out} \approx 1$ (Figure 4.4 **C**). Since Chloramphenicol is predominantly transported inside of the cell by OmpF porins, we estimated the permeability coefficients for fluorescent oflaxacin that is also translocated by OmpF [153]. By analyzing time traces of fluorescent antibiotic accumulation inside of the cell, we estimated that growing *E. coli* cells readily accumulate antibiotics, $P_{\rm in}/P_{\rm out} \approx 0.54$, while for stationary cells $P_{\rm in}/P_{\rm out} \approx 0.11$. Interestingly, for bacterial cells lacking porins ($\Delta ompF$), $P_{\rm in}/P_{\rm out} \approx 0.18$ and for bacteria lacking efflux pumps ($\Delta tolC$), $P_{\rm in}/P_{\rm out} \approx 0.66$. Therefore, these results suggest that the antibiotic dilution by changes in $S/V$ could approach

the maximum value achieved for $P_{\text{in}} \approx P_{\text{out}}$ and large $k_{\text{on}}/k_{\text{off}}$ (Figure 4.4 **C**).

## 4.6 Discussion

Comparing our theory to experimental data, we uncover several feedback pathways among cell shape, growth rate, protein synthesis, and extracellular transport that were previously unknown (Figure 4.3 **F**). In particular, we predict that under translation inhibition, cells break the balanced trade-off between ribosomes and division protein synthesis, leading to cell size inflation, reduction, or size invariance, in a nutrient-dependent manner. Our model predictions are in quantitative agreement with experimental data on *E. coli* cells subjected to chloramphenicol perturbations across various nutrient conditions[5]. If cells are grown in nutrient-rich media, the excess ribosomes produced under translation inhibition are allocated toward division, leading to smaller cell sizes and higher surface-to-volume ratios. This is in agreement with chloramphenicol-treated *E. coli* cells grown in synthetic rich medium. Conversely, in nutrient-poor media cells allocate excess ribosomes toward growth, leading to cell size inflation and lower surface-to-volume ratios, in agreement with *E. coli* cell data in glycerol medium.

Our results suggest that changes in cell shape, in response to translation-inhibitory antibiotics, may confer certain fitness advantages under stress. In nutrient-rich media, it is more favorable for cells to reduce their surface-to-volume to minimize antibiotic influx. Whereas in nutrient-poor media, cells adapt to import more nutrients by increasing their surface-to-volume ratios. To quantitatively test the role of cell shape and nutrient quality on bacterial growth inhibition under antibiotic stress, we simulated bacterial growth under simultaneous perturbation of surface area production and translation inhibition in varying nutrient media (Figure 4.3). From growth-inhibition curves we measured bacterial response to antibiotics by quantifying resistance (half-inhibitory concentration of the drug) and dose sensitivity to increasing concentration of the drug. Round-shaped cells are fitter and more drug resistant than higher-aspect-ratio filamentous cells, and dose sensitivity increases with increasing nutrient quality. These results can be tested experimentally by measuring bacterial growth rates in response to simultaneous application

of cell-wall targeting and ribosome-targeting antibiotics, in different nutrient concentrations. Interestingly, we predict that bacterial growth-inhibition can be maximized by simultaneously inhibiting ribosomal translation and promoting surface area production in nutrient-poor media.

In synergy with shape changes, bacteria can actively regulate the antibiotic concentration inside the cell by controlling porin and efflux pump expression [157, 158]. Cell wall-targeting antibiotics, such as $\beta$-lactams, that disrupt the stability of the peptidoglycan meshwork are translocated by OmpF porins to induce the envelope stress response (Cpx) [159]. The activation of the Cpx system decreases ompF expression [160], creating a negative-feedback loop, resulting in lower porin numbers and lower inward membrane permeability ($P_{in}$). Similarly, when E. coli cells are exposed to DNA-targeting antibiotics that are also translocated inside the cell by OmpF, the expression level of ompF decreases within 30 to 120 min after antibiotic treatment [157]. A reduction in porin numbers will act in synergy with a reduction of $S/V$ to confer stronger resistance phenotypes. In addition to controlling antibiotic influx, bacteria can decrease the intercellular antibiotic concentration through the overexpression of efflux pumps [157, 161, 162]. In the future, time-lapse experiments are necessary to reveal the time scales associated with the onset and completion of morphological transformation under antibiotic perturbations and how these time scales compare with changes in the expression profiles of proteins responsible for regulating antibiotic influx and efflux. These studies would be essential to quantify the contributions of the different resistance pathways and their synergistic effects responsible for increasing bacterial fitness.

A reduction in surface-to-volume ratio not only lowers antibiotic influx, but also leads to a reduced nutrient influx that may in turn lower cellular metabolic activity. In recent work, Lopatkin *et al.* showed that metabolism plays a crucial role in bacterial response to antibiotics such that cells with decreased metabolic activities are more antibiotic-resistant [163]. Metabolic mutations in response to antibiotic exposure suggest adaptive mechanisms in central carbon and energy metabolism. Interestingly, some of the advan-

tageous metabolic mutations that mitigate antibiotic susceptibility have been identified in $> 3500$ clinically relevant pathogenic *E. coli* [163]. These findings point towards a new pathway of antibiotic resistance mediated by mutations in the core metabolic genes. Our findings that bacteria decrease surface-to-volume may act in synergy with the metabolic slowdown to confer stronger antibiotic resistance.

# Chapter 5

# Energy allocation theory for bacterial growth and cell shape control

Efficient allocation of energy resources to the main physiological functions of the cell allows bacteria to grow and thrive in diverse environments and survive under a wide range of perturbations. To understand how bacteria regulate their growth rate, cell shape and size in different environmental conditions, resource allocation theories based on proteome partitioning (Chapter 2) provide a meaningful coarse-grained description of cellular physiology when no mechanistic information is available. However, once the model requires constraints to be imposed on proteins that are present in relatively small copy numbers, one needs to introduce a new "micro-sector" for every new perturbation to the proteome. This leads to a computationally expensive model and intricate relationships between different sectors when the perturbations affect multiple protein classes.

To overcome this limitation, we develop a mechanistic model based on the allocation of cellular energy to key cellular functions: nutrient import into the cell, energy expended for growth and division, metabolism, shape maintenance and energy loss due to dissipation. It is important to note that the model is based on allocation of resources rather

than specific proteins making it versatile in understanding the cellular physiology and morphology under chemical and mechanical perturbations.

Energy budget models have been previously used to understand ontogenetic growth. Derived from data from birds and mammals, Hou *et al.* [164] developed a model predicting how growing animals allocate food energy between synthesis of new biomass and maintenance of existing mass. During growth, some fraction of the food is oxidized to sustain the total metabolic rate and the remaining fraction is synthesised and stored as biomass. The metabolic rate is then partitioned between the resting metabolic rate (used as energy for maintenance and the rate of energy for biosynthesis) and the rate of energy for locomotion and other activities. Combining the model for partitioning of assimilated energy and resource allocation strategies for bacterial growth, we developed a mechanistic model based on the budgeting of cellular energy for key physiological unctions in a bacterium: nutrient import, growth, division, metabolism, shape maintenance and energy loss.

For a given intake energy, we optimize the energy used for cellular growth to derive the equations governing cell elongation, shape maintenance and protein production. The resultant model allows us to predict the mechanical and chemical response of the cell in different environmental conditions and under diverse perturbations. In particular, by calibrating the model parameters with available experimental data on the model organism *E. coli*, we simulate the cellular growth and shape dynamics in response to dynamic nutrient shifts and osmotic shocks.

### 5.1 Energy budget model

The energy budget model is based on optimizing the rate of assimilation of physiological energy in the cell. The energy per cell changes according to:

$$\frac{dE_{cell}}{dt} = \frac{dE_{in}}{dt} - \frac{dE_{used}}{dt} \tag{5.1}$$

where $E_{\text{in}}$ is the energy influx, and $E_{used}$ is the total energy used for different physiological processes such as metabolism, division, shape maintenance or dissipated as heat

(Figure 5.1). To build new cellular mass, the energy available via nutrient influx must be in excess of that needed for metabolism. We thus assume that the excess energy $E_{cell}$ is used for growth.

Our *key hypothesis* is that a growing cell maximizes the rate of energy assimilation, which is used for growth:

$$\frac{\partial \dot{E}_{cell}}{\partial \dot{q}_i} = 0 \, , \tag{5.2}$$

where $\{q_i(t)\}$ is the set of variables that describe the non-equilibrium state of the cell. For rod-shaped bacterial cell, a minimal number of variables representing the physiological state of the cell could be cell length, radius and protein copy number. Below we describe the key energy components considered by our theory for cellular functions such as nutrient uptake, cell division, metabolism, cell mechanics and shape maintenance, and energy loss due to dissipation.

## 5.2 Energy components of the cell

The *intake energy* flux occurs through the cell surface at a rate $J$ per unit surface area $S$. Therefore, $dE_{\rm in}/dt = JS$, with $J = d\varepsilon/dt$, such that $\varepsilon$ is the energy uptake per unit surface area of the cell:

$$\frac{dE_{in}}{dt} = \frac{d\varepsilon}{dt} S \, . \tag{5.3}$$

For *division*, we consider the energy spent to produce division proteins, rather than the last stage of division when the cell wall starts constricting. The division energy is therefore proportional to the number of division proteins:

$$E_{div} = -\mu X \tag{5.4}$$

where $\mu$ is the chemical potential for division protein synthesis, and $X$ is the division protein copy number in the cell. Following the threshold initiator model for cell division control (see Chapter 2), the cells divide upon accumulating a fixed threshold number of division proteins at the septum. As presented in Chapter 3 and in [67], the threshold protein copy number is proportional to the cell diameter: $X_0 = 2\pi R\gamma$, where $\gamma$ is the

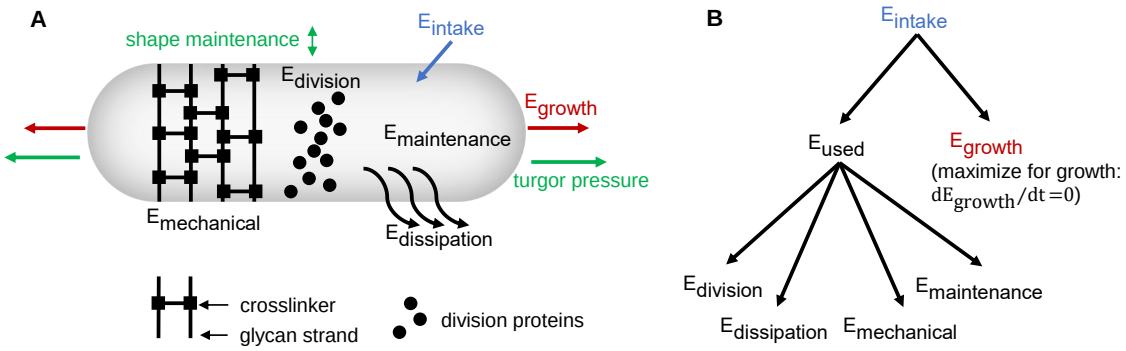


Figure 5.1: **Model schematic and optimization principle. A.** Food from extracellular environment is imported inside the cell via the membrane and represented by the intake energy ($E_{intake}$) which is proportional to the surface area of the cell. Cells elongate while maintaining a fixed radius (shape maintenance represented in green) by using the energy for growth ($E_{growth}$). The energy used by the cell during a growth cycle is allocated to different physiological processes such as maintenance of biomass ($E_{maintenance}$) and division ($E_{division}$), but also converted to mechanical energy ($E_{mechanical}$) to balance turgor pressure and store stain energy in the cell wall (proxy for crosslinkers and glycan strands, see main text). We also account for energy loss due to dissipation ($E_{dissipation}$) and protein production. **B.** Energy diagram showing the energy used for growth $E_{growth} = E_{intake} - E_{used}$, where $E_{used} = E_{division} + E_{dissipation} + E_{mechanical} + E_{maintenance}$. Optimizing the rate of assimilation of physiological energy (i.e. $dE_{growth}/dt = 0$) translates into optimizing the energy for cell growth.

proportionality constant, and $R$ is the cell radius. Therefore, the energy required to synthesize the sufficient amount of proteins for cell division is given by: $E^*_{div} = -2\mu\gamma\pi R$.

The energy for the maintenance of existing biomass is $E_M = gV \approx g\pi R^2 L$, where $g$ is the maintenance energy per unit volume and $V$ is the cell volume. We thus interpret $dE_M/dt$ is the *resting metabolic rate* of the cell.

The *mechanical energy* of the cell envelope is given by the sum of contributions from the energy required to maintain cell width ($E_{\text{width}}$) and the elastic strain energy in the cell wall arising from the internal turgor pressure ($P$) [165]:

$$E_{\text{mech}} = E_{\text{width}} + E_{strain} \tag{5.5}$$

where $E_{\text{width}} = \kappa_c \pi R L \left(\frac{1}{R} - \frac{1}{R_0}\right)^2$, where $R_0$ is the reference radius of cross-section and $\kappa_c$ is the rigidity. The *elastic strain energy* can be expressed/approximated as $E_s = N_g E_p$ where $N_g$ is the number of glycan strands and $E_p$ is the energy of all the crosslinkers connecting two consecutive glycan strands. Under no growth/stretching, the elastic energy of the peptides balances the turgor pressure, i.e., $E_p = PV_p$ where $V_p$ is the volume of the region enclosed between two consecutive glycan strands. However, as the cell elongates, the mechanical energy of the peptides is positive: $E_{mech,p} = E_p - PV_p = E_p - P\pi R^2 l > 0$:

$$E_{mech,p} = \frac{1}{2} k_s \rho_p 2\pi R \left(l - l_0\right)^2 - P\pi R^2 l > 0 \tag{5.6}$$

where $l$ is the length of a peptide/crosslinker, $l_0$ is the rest length of a peptide/crosslinker. We assume that mechanical energy of the strained peptides relaxes at a much faster timescale than the timescale for cellular growth. This assumption allows us to compute the effective strain energy of the cell envelope by minimizing the mechanical energy of the peptides $\partial E_{mech,p}/\partial l = 0$, which results in the expression for the length deformation in terms of pressure: $\delta l = l - l_0 = PR/(2k_s\rho_p)$. Therefore, we can rewrite the strain energy $E_s = N_g E_p$ as follows:

$$E_{strain} = N_g \frac{1}{2} k_s \rho_p 2\pi R \left(\frac{PR}{2k_s\rho_p}\right)^2 = N_g \pi \frac{P^2 R^3}{4k_s\rho_p} = \rho_g L \pi \frac{P^2 R^3}{4k_s\rho_p} = \lambda \pi R^3 L$$

where $\lambda = \frac{P^2 \rho_g}{4 k_s \rho_p}$ is a material parameter of the cell, and $\rho_g = N_g/L$ is the line density of the glycan strands. From Eq. 5.5 we can derive the total mechanical energy as:

$$E_{mech} = \kappa_c \pi R L \left( \frac{1}{R} - \frac{1}{R_0} \right)^2 + \lambda \pi R^3 L \tag{5.7}$$

The energy lost as *dissipation* consists of mechanical and chemical components. Firstly, the dissipation of mechanical energy corresponds to the amount of work done to the medium when the shape of the cell deforms at a rate $\dot{q}_i$, where $q_i \in \{R, L\}$. Banerjee *et al.* [165] derived the dissipated energy to be $\mathscr{D}_1 = \frac{1}{2} V_d \sum_i \eta_i \left( \frac{\dot{q}_i}{q_i} \right)^2$, where $V_d = hS$ is the volume of dissipation, $h$ is the envelope thickness, $S \approx 2\pi RL$ is the area of dissipation, and $\eta_i \in \{\eta_L, \eta_R\}$ is the viscosity parameter. Secondly, dissipation of chemical energy is proportional to the rate of production of division proteins $\dot{X}$ : $\mathscr{D}_2 = \frac{\xi}{2V} \dot{X}^2$, where $\xi$ regulates dissipation rate via protein production. Therefore, the total dissipation rate is $\mathscr{D} = \mathscr{D}_1 + \mathscr{D}_2$:

$$\mathscr{D} = \frac{1}{2} V_d \sum_i \eta_i \left( \frac{\dot{q}_i}{q_i} \right)^2 + \frac{\xi}{2V} \dot{X}^2. \tag{5.8}$$

By definition, the elongation rate is $\kappa_L = \frac{1}{L} \frac{dL}{dt}$, the radial growth rate is $\kappa_R = \frac{1}{R} \frac{dR}{dt}$ and the division protein synthesis rate is $k_P = \frac{1}{L} \frac{dX}{dt}$. Therefore, the dissipation rate becomes:

$$\mathscr{D} \approx \pi RLh \left( \eta_L \kappa_L^2 + \eta_R \kappa_R^2 \right) + \frac{\xi L}{2\pi R^2} k_P^2.$$

Having accounted for the main physiological functions of the cell (i.e. what $E_{used}$ is used for), we can re-write the rate of energy assimilation in the cell as:

$$\frac{dE_{cell}}{dt} = \frac{dE_{in}}{dt} - \frac{dE_{used}}{dt} = JA - \left( \frac{dE_{div}}{dt} + \mathscr{D} + \frac{dE_{mech}}{dt} + \frac{dE_M}{dt} \right) \tag{5.9}$$

### 5.3 Equations of motion for cellular variables

To derive the equations of motion governing the dynamics of cellular variables $q(t)$, we maximize $dE_{cell}/dt$ with respect to the rate of change of $q$. For a rod-shaped bacterial cell $q$ is represented by the cell length $L$, cell radius $R$, and the copy number of the division protein $X$. As a first step, from optimizing $\dot{E}_{cell}$ with respect to $\dot{X}$, the division

protein number, we can obtain the rate of synthesis of division proteins ($\kappa_p$) as follows:
$\frac{\partial \mathscr{D}}{\partial \dot{X}} + \frac{\partial E_{div}}{\partial X} = \frac{\xi}{V}\dot{X} - \mu = 0$

$$\therefore \frac{dX}{dt} = \frac{\mu}{\xi} V = k_P L \tag{5.10}$$

where $k_P = \pi R^2 \mu / \xi$. By combining Eq. 5.9 and 5.2 we obtain the *equations of motion* governing the dynamics of cell length and radius:

$$(2h\eta_L)\,\frac{\dot{L}}{L} = 2\varepsilon - gR - \frac{1}{\pi R}\frac{\partial E_{\text{mech}}}{\partial L}\ . \tag{5.11}$$

$$(2h\eta_R)\,\frac{\dot{R}}{R} = 2(\varepsilon - gR) - \frac{1}{\pi L}\frac{\partial E_{\text{mech}}}{\partial R}\ . \tag{5.12}$$

The mechanical energy assumes the scaling form $E_m(R, L) = \pi U(R) L$ so we can re-write the equations of motion as:

$$\frac{1}{L}\frac{dL}{dt} = \mu_L \left( (2\varepsilon - gR) - \frac{U(R)}{R} \right)\ , \tag{5.13}$$

$$\frac{1}{R}\frac{dR}{dt} = \mu_R \left( 2(\varepsilon - gR) - \frac{dU}{dR} \right)\ , \tag{5.14}$$

where $\mu_L = 2\eta_L h$ and $\mu_R = 2\eta_R h$. It is evident from Eq. (5.13) that cell length increases exponentially at a rate $\kappa$ given by (Figure 5.2 **A**):

$$\therefore \kappa = \mu_L(2\varepsilon - gR) - \mu_L \frac{U(R)}{R}\ . \tag{5.15}$$

Cell radius, on the other hand, is constant during cell elongation, and is given by the minimum of the the effective energy $E_{\text{eff}}$ defined as:

$$E_{\text{eff}} = \int \left( 2(\epsilon - gR) - \frac{dU}{dR} \right) dR = 2\epsilon R - gR^2 - U\ . \tag{5.16}$$

Upon a nutrient shift, the landscape for the effective energy changes and cells find a new radius that minimizes $E_{\text{eff}}$ (Figure 5.2 **B**). From Eqs. 5.10, 5.13 and 5.14 we can simulate the dynamics of length, radius and division protein number over multiple generations as a single cell grows and divides (Figure 5.2 **C-D**).

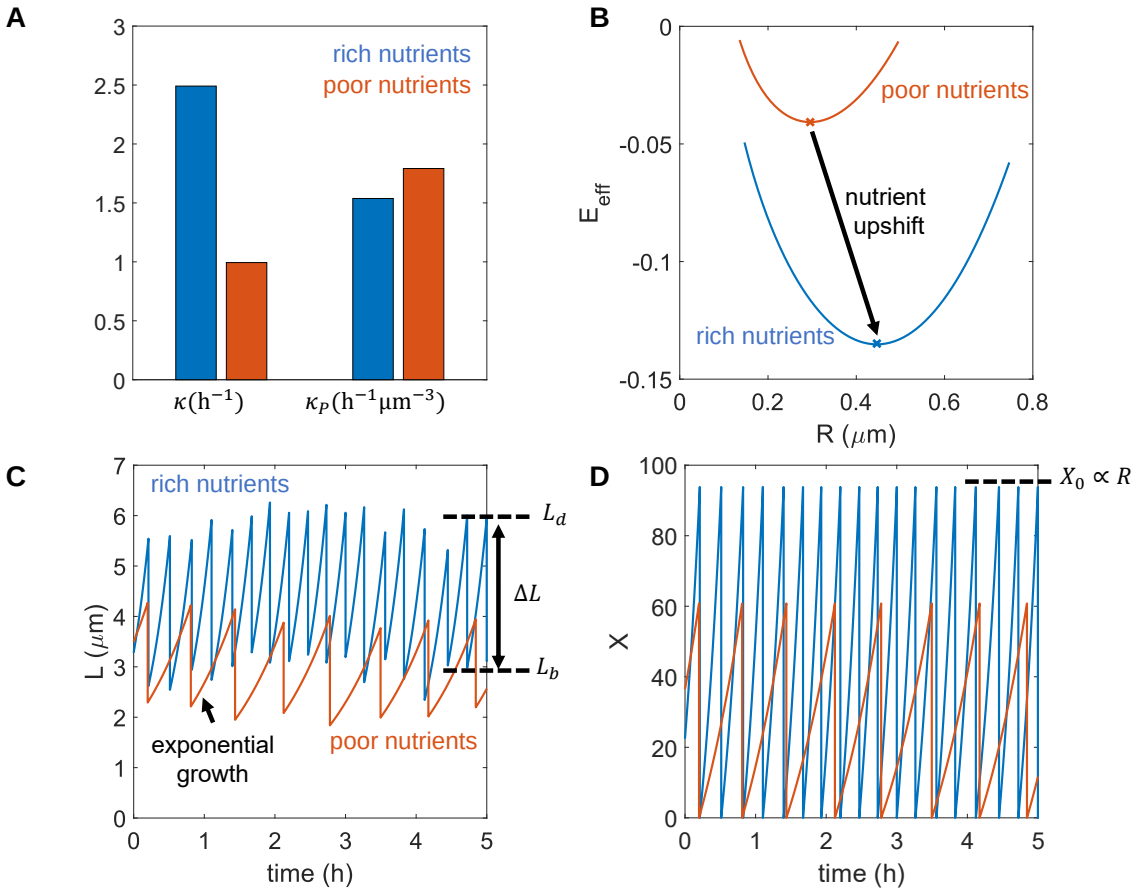


Figure 5.2: **Single cell trajectories predicted by the energy budget model. A.** Growth rates ($\kappa$) and division protein synthesis rates ($\kappa_P$) for rich and poor nutrients in the extracellular medium. **B.** The minimum of the effective energy $E_{\mathrm{eff}}$ corresponds to the preferred radius in the respective growth condition. Nutrient shifts correspond to transitions from one minimum to another. **C.** Dynamics of length in two nutrient conditions where cells have the same growth rates as shown in panel **A**. The length grows exponentially in time and add a fixed length between birth and division $\Delta L = L_d - L_b$ in agreement to the *threshold initiator* model and the *adder* principle. **D.** Cells accumulate division proteins as described by $dX/dt = k_P L$ and divide upon reaching a threshold value proportional to the circumference of the cell: $X_0 = 2\gamma R$. The threshold value is constant for a nutrient condition leading to constant added lengths $\Delta L$ (defined in panel **C.**).

Figure 5.2: Continued caption. Note: We introduce noise in the division ratio $D_R$ such that $L_{i+1}(t=0) = D_R L_i(t=\tau_i)$, where $L_{i+1}(t=0)$ is the length of the cell in generation $i+1$ at birth, $L_i(t=\tau_i)$ is the length of the cell in generation $i$ at division, $\tau_i$ is the division time and $D_R$ is a Gaussian random variable with mean 0.5 and standard deviation 0.05.

### 5.4 Parameter determination and simulation protocol

The reference radius of cross-section $R_0$ can be fixed to the preferred radius of curvature for MreB ($200 - 400nm$ [166]) which is independent of nutrient conditions. MreB forms dynamic helical filaments around the periphery of the cell, perpendicular to the long axis of the cell [167], thus the radius of curvature can be used as a proxy for the radius of cross section of the whole cell. The material parameter of the cell $\lambda = \frac{P^2\rho_g}{4k_s\rho_P}$ can be estimated from known physical parameters of the cell. The turgor pressure in *E. coli* cells is $P = 0.3MPa$, $k_s = 0.03MPa\mu m^3$ [165], $\rho_g = 1000$ and $\rho_p = 25$ [168] [100], leading to $\lambda \approx 30$ (Figure 5.3 **A**).

The model comes with several other parameters not known apriori: $\lambda, \epsilon, g, \mu_L, \mu_R$, and $k_c$. We normalise the parameters as $\bar{\lambda} = \lambda/k_c$, $\bar{\epsilon} = \epsilon/k_c$, $\bar{g} = g/k_c$, $\bar{\mu_L} = k_c\mu_L$ and $\bar{\mu_R} = k_c\mu_R$. From experimental data on steady-state exponential growth rate and the morphology of bacterial cells, we have the initial conditions $\kappa = \kappa_{\text{specific}}$ and $R = R^*$. From Eq. 5.13 we write the first initial condition as:

$$\kappa_{\text{specific}} = \bar{\mu_L}(2\bar{\epsilon} - \bar{g}R^*) - \bar{\mu_L}\frac{U(R^*)}{R^*}\,, \tag{5.17}$$

from which we can determine $\bar{\mu_L} = \kappa_{\text{specific}}^{-1}\left(-\bar{\lambda}R^{*^2} + 2\bar{\epsilon} - \bar{g}R^* - (1/R^* - 1/R_0)\right)$. The second initial condition is that the effective energy $E_{\text{eff}}$ is minimised by the radius (i.e. $\frac{dU}{dR} = 2(\bar{\epsilon} - \bar{g}R)$ when $R = R^*$) from which we obtain $\bar{\epsilon}$:

$$\bar{\epsilon} = \bar{g}R^* + \frac{3}{2}\bar{\lambda}R^{*^2} + \frac{1}{2}\left(\frac{1}{R^*} - \frac{1}{R_0}\right)^2 + \frac{R^* - R_0}{R_0R^{*^2}}\,. \tag{5.18}$$

The leftover unknown parameters $\bar{\lambda}$ and $\bar{g}$ are determined by fitting the experimental data for the dependence of steady-state cell volume on growth rate (Figure 5.3 **A-B**). We use the root mean square deviation from the mean as a measure for the goodness of

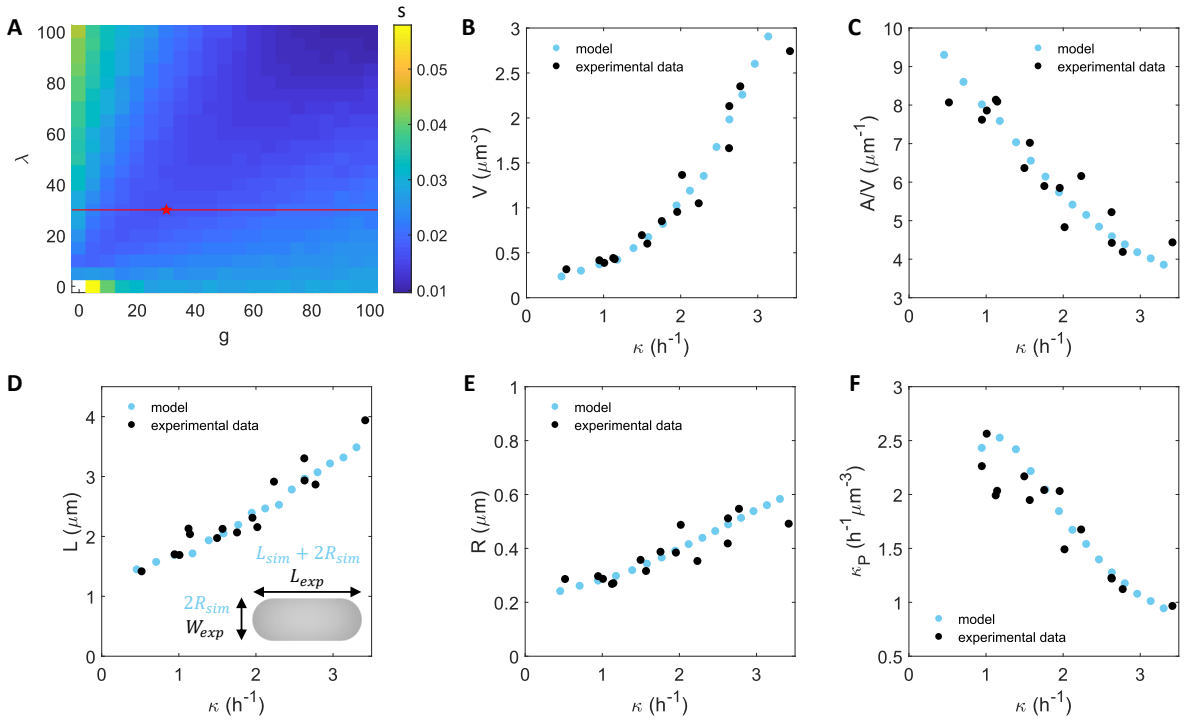


Figure 5.3: **Dependence of cell morphology on growth rate obtained using the energy budget model. A.** Heatmap of *fitting coefficient* ($S$) for different values of $\bar{\lambda}$ and $\bar{g}$. The fitting coefficient is defined as $S = \frac{\sqrt{\sum(V_{exp} - V_{sim})^2}}{N}$, where $V_{exp}$ is the expected cell size value from the exponential fit following the nutrient growth law, $V_{sim}$ is the average steady state value in simulations and $N$ is the number of points used. Red line indicates $\bar{\lambda} \approx 30$, value estimated from literature (see main text) and the star indicates the minimum value for $S$ for this value that helps set $g \approx 30$. Unless otherwise stated, the parameter values are $\bar{\lambda} = 30$ and $\bar{g} = 30$. **B-C.** Cell size volume and surface area as a function of growth rate obtained from the model and experimental data. **D.** Cell length as a function of growth rate, where we accounted for the pole-to-pole length to compare to experimental data (inset). **E-F.** Radius and division protein synthesis rate ($\kappa_P = k_P/(\pi R^2)$) as a function of growth rate obtained from the model and experimental data from Taheri *et al.* [32]. $\kappa_P$ is estimated as $\kappa/V$ from experimental data as in Chapter 2. Parameters used: $\eta = 3$, $\gamma = 100$, $\mu = 1$, $\xi = 0.0036$, $k_c = 1$, $\bar{\mu_R} = 0.1$, $h = 0.1 * 10^{-3}$, $\bar{g} = 30$, $\bar{\lambda} = 30$, $R_0 = 0.3$, $\sigma_R = 0.0267$.

the fit: $s = \sqrt{\sum (V_{exp} - V_{sim})^2}/N$, where $V_{exp}$ is the expected cell size value from the nutrient growth law fitted to experimental data (Eq. 1.9), $V_{sim}$ is the value for the cell size obtained from simulating single cell growth at steady state and $N$ is the number of points used to calculate $s$. The parameter $\bar{\mu}_R$ controls how fast the cell radius adapts to a new steady-state value when deviated from the steady-state, but it does not influence the morphology of the cell at steady state. Below we show how $\bar{\mu}_R$ and can be calibrated from experimental data on bacteria growing in non-steady growth conditions, such as nutrient shifts or antibiotic-induced stresses (Figure 5.5). After finding the best fits for volume as a function of the growth rate (Figure 5.3 **B**) and calculating the remaining free parameters, we can compare without any further fitting the surface-to-volume ratio, length, radius and division protein synthesis as a function of growth rate obtained from simulations against experimental data (Figure 5.3 **C-F**).

## 5.5 Cellular energy allocation in different nutrient environments

With the free model parameters calibrated using experimental data in Figure 5.3, we can go back to the theoretical model, and predict how cellular energy is partitioned and allocated to different physiological functions in different nutrient conditions. In terms of absolute values, all energies increase as a function of growth rate (Figure 5.4 **A**), however when normalized by the intake energy, we observe different behaviours for the energy fractions allocated to different tasks (Figure 5.4 **B**): the mechanical energy has a non-monotonic behaviour while the energy for maintenance and the dissipation rate decrease. Clustering the energy components into energy for growth, mechanical and metabolic energies, the theory predicts a decrease in the metabolic energy (Figure 5.4 **C**), consistent with metabolic proteins mass fraction decreasing with nutrient quality in proteomics experiments [6]. The final comparison to proteomic components is between the normalised energy for growth and ribosomal mass fraction $\phi_R$ which can be calculated from the growth rate by using Eq. 1.2. The normalised energy for growth increases with the ribosome mass fraction, analogous to the bacterial growth law (Figure 5.4 **D**).

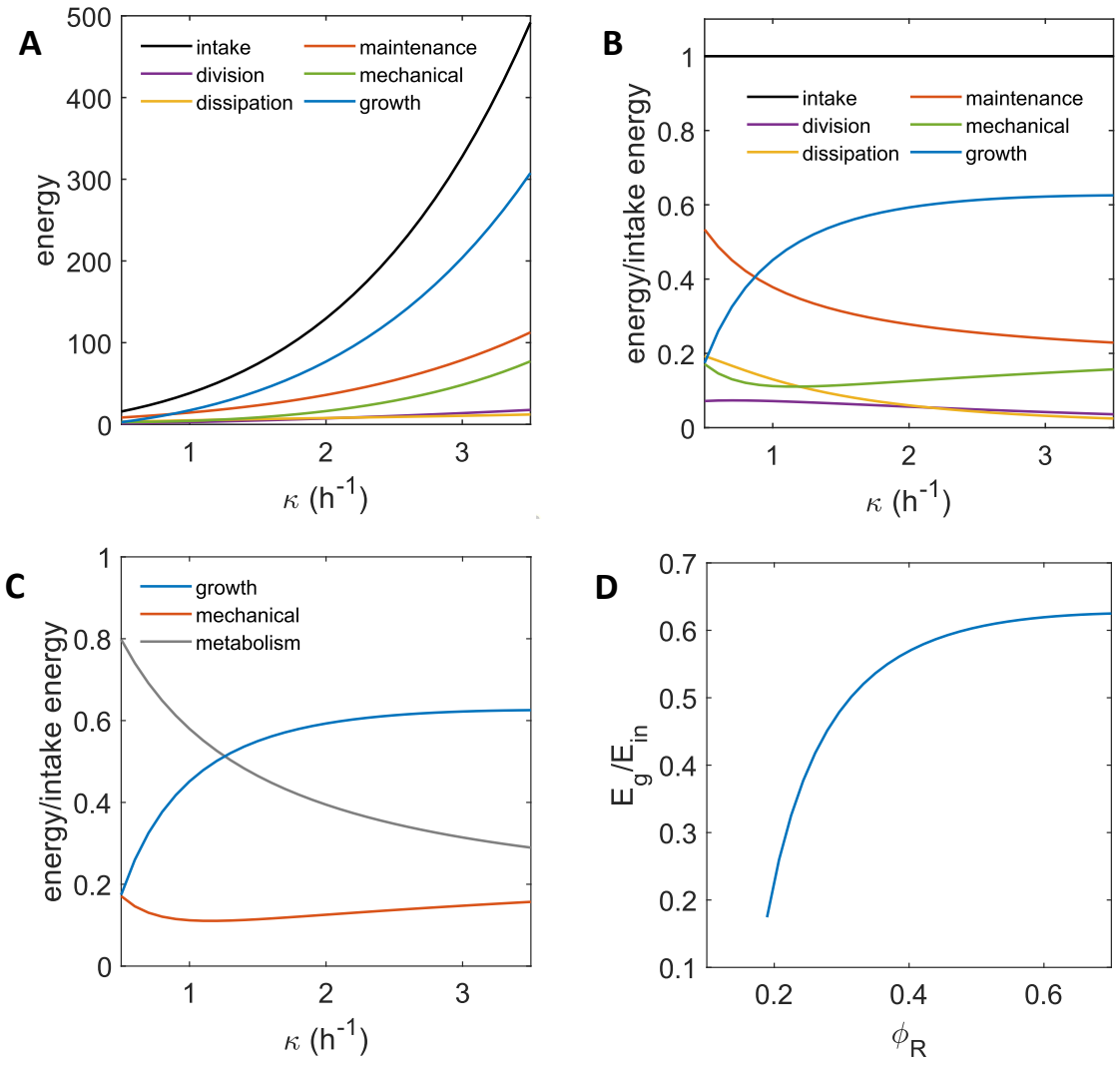


Figure 5.4: **Cellular energy allocation in different nutrient environments**. **A-B.** The values for the energy components are calculated from theory (summarised in Table 7.4) and the expression for length and radius as a function of growth rate are obtained from fitting single cell data from [32] (i.e. $L = 1.262e^{0.3288\kappa}$ and $R = 0.1\kappa + 0.195$). **C.** Combining the energy components into energy for growth, mechanical energy and metabolism for a qualitative comparison to proteomic data from [6]. **D.** The normalised energy for growth increases with ribosome mass fraction.

## 5.6 Cellular response to nutrient up- and down- shifts

After calibrating the parameters to steady-state cell size experimental data (Figure 4.1) and ensuring that the energy components behave in synergy with the proteomic components (Figure 4.4), we study cellular response to nutrient shifts.

The change in nutrient quality can be simulated by changing $\epsilon$ which controls the nutrient influx ($dE_{in}/dt = Sd\epsilon/dt$) and to represent a gradual response we use a Heaviside step function $\bar{\epsilon} = \bar{\epsilon}\left(1 + \alpha(1 + e^{-hs(t-t_{shift})})^{-1}\right)$, where $\alpha$ is the percentage increase in nutrient quality, $hs$ is the steepness of the function and $t_{shift}$ is the time when the shift is applied. In Figure 5.5 **A** the response of $\bar{\epsilon}$ is shown for different values of $hs$ representing fast and slow changes in the nutrient quality in the extracellular environment.

Furthermore, we can tune the adaptive response of the growth rate via the radial mobility coefficient $\mu_R$ introduced in Eq. 5.14. The radius does not change as the cell elongates during the cell cycle for a fixed $\epsilon$ (i.e. nutrient environment), but how fast the radius reaches the new value is dictated by $\mu_R$ (Figure5.5 **C**). In other words, the transitions from one energy minimum to another in Figure 5.2 **B** is given by the radial mobility coefficient. Interestingly, for slow adaptive response we observe an overshoot in growth rate and a slow relaxation to the new steady state value, but the length dynamics does not present any over- or under-shooting (Figure 5.5 **D**). The growth rate response for a nutrient up- and down-shift can be compared to experimental data [33] (Figure 5.5 **E-F**) by fitting $\alpha$ and $hs$.

While the nutrient upshift can be captured by changing how fast the extracellular nutrients change ($hs$) and the intrinsic response of the cell ($\bar{\mu_R}$), the nutrient downshift requires a change in $\bar{g}$, the maintenance energy per unit volume. This suggests that during the transition from one steady state to another following nutrient depletion, cells invest resources into other physiological functions. Previous work suggested bacterial cells overexpress proteins to quickly meet demand upon sudden improvement in growth conditions [169]. Similarly, our results can be interpreted as cells decreasing the energy for maintenance and investing allocating more resources to growth or metabolic energies

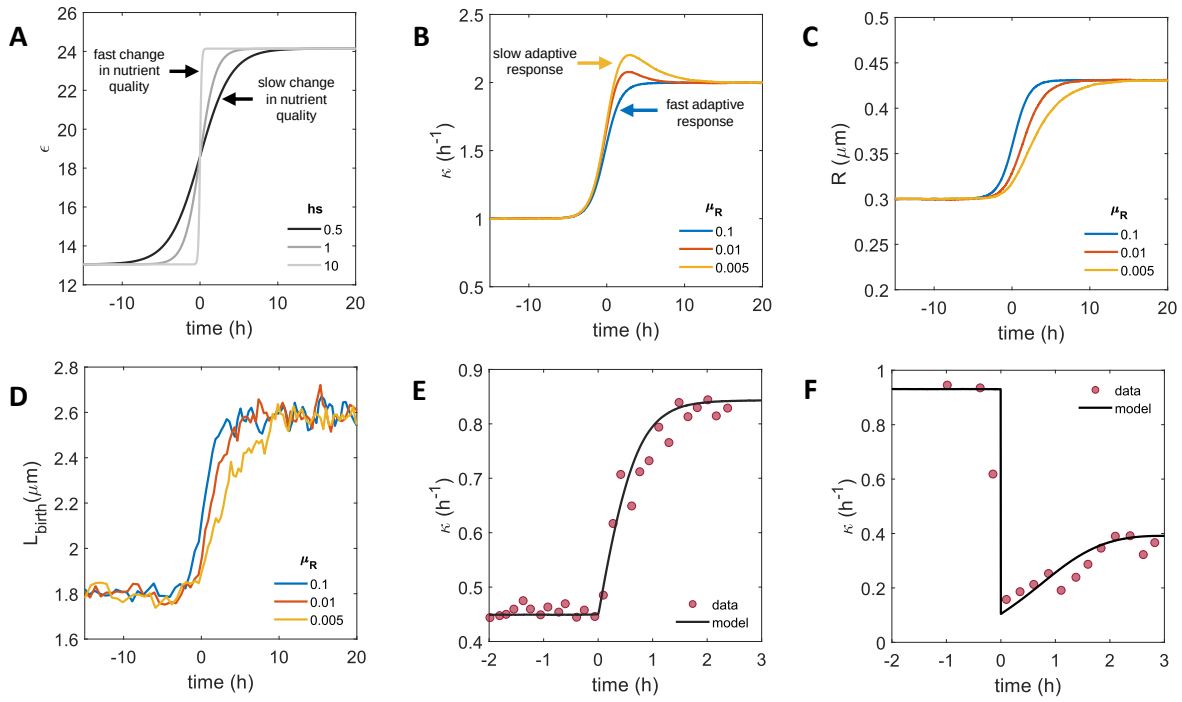


Figure 5.5: **Single-cell nutrient shift simulation using the energy model. A.** The upshift is simulated by increasing $\epsilon$ using a Heaviside step function: $\bar{\epsilon} = \bar{\epsilon}(1+\alpha(1+e^{-hs(t-t_{shift})})^{-1})$, where $\alpha$ represents the increase (or decrease if $\alpha < 0$) in nutrient quality and $t_{shift}$ is the time at which the perturbation is applied. $hs$ describes the steepness of the function or how fast the nutrient quality is changed: high $hs$ corresponds to a fast change in nutrient quality, while low $hs$ corresponds to a slow change. **B-D.** The response of growth rate $\kappa$, radius $R$ and length $L$ of the cell upon a nutrient up-shift when $hs = 1$ and the mobility coefficient for three different values of $\mu_R$ corresponding to slow, medium and fast adaptive response. **E-F.** Comparison of simulated nutrient up- and down-shift to experimental data from [33]. **Parameters used**: $\eta = 3$, $\gamma = 30$, $\bar{\mu_R} = 0.1$ in panel **A** and variable in **B-D**, $k_c = 1$, $h = 0.1 * 10^{-3}$, $\bar{g} = 30$, $\bar{\lambda} = 30$, $R_0 = 0.3$, $\sigma_R = 0.0267$, $\alpha = 0.3$, $hs$ variable in panel A and $hs = 1$ in panels **B-D**. For panels **E** and **F** we fitted $\alpha$ and $hs$ to capture the nutrient shifts. Note: for the nutrient downshift we decreased $\bar{g}$ by $2 * 10^{-5}$.

upon nutrient depletion for a quicker adaptation to the new steady state.

## 5.7 Discussion

In this Chapter I presented an energy budget model based on allocation cellular energy to different physiological tasks, where optimizing the cellular energy for growth results in equation of motion for various cellular variables from an underlying energy function. One of the advantages of using a physiological-based coarse-graining as opposed to a proteome partitioning theory (Chapter 2) is that we can investigate the cellular response to diverse types of perturbations without adding any new protein sectors to the model.

In addition to nutrient perturbations, the model can be used to capture behaviour observed in osmotic shock experiments [170], which involves changing the osmolarity of the growth medium, leading to changes in the turgor pressure ($\lambda$ in our model) of the cell. Rojas *et al.* [170] showed that osmotic pressure is not essential for cell-wall expansion of E. coli cells and that growth is robust to changes in osmotic pressure. In an initial attempt at simulating the osmotic shock experiments, we altered $\bar{\lambda}$ and looked at the response of growth rate, length and radius in time (Figure 5.6). Using the same parameters as for nutrient shifts, we notice that for small changes in $\lambda$ the growth rate recovers to the pre-shock value.

In the future we plan on using the model, to capture various other physiological perturbations, such temperature snd pressure changes in the extracellular environment [171]. The theory is not constrained by the shape of the cells, as Banerjee *et al.* showed [165], the equations of motion for the length and radius can also capture the dynamics for the shape parameters for spherical cells. Therefore, another idea is to apply the model to other cell shapes, such as flattened bacteria under mechanical stress [172]. Lastly, by looking at the metabolic energy during the cell cycle we can connect it to ATP production. In recent experiments, Li and Jacobs-Wagner [173] show that the ATP concentration is non-monotonic between cell birth and division.

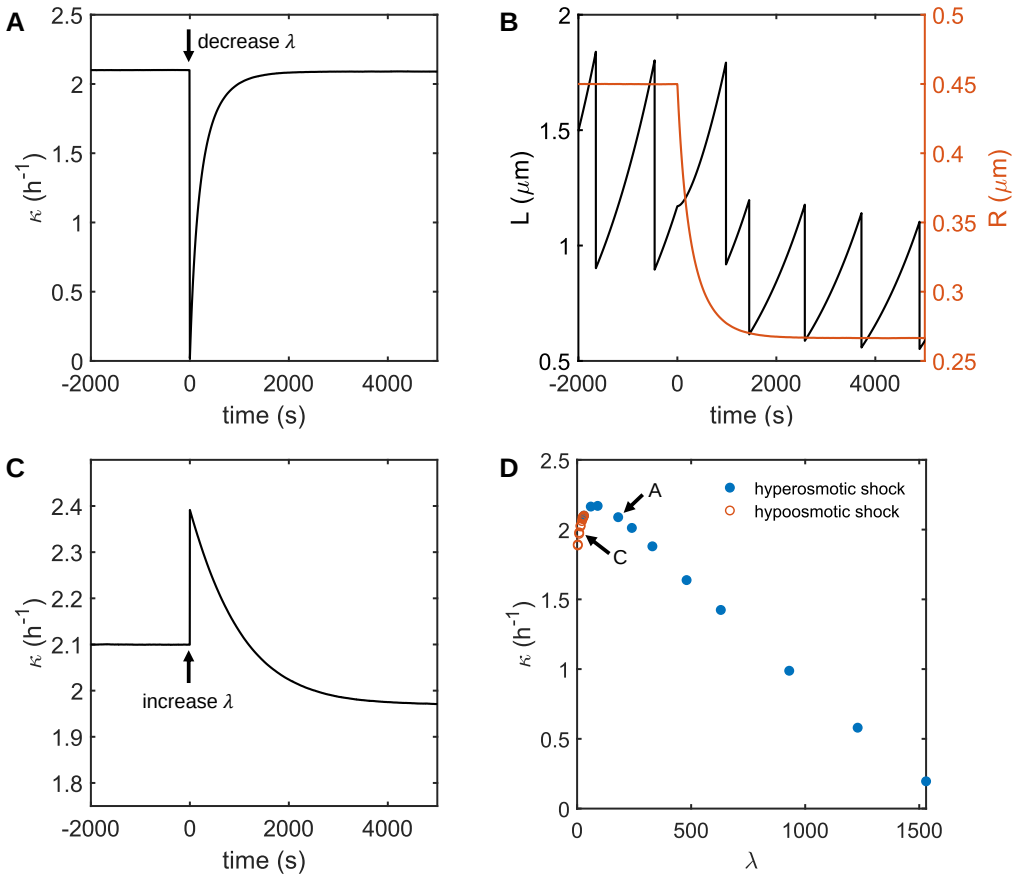


Figure 5.6: **Single-cell osmotic shock simulation using the energy model. A.** Growth rate dynamics following a hyperosmotic shock at $t = 0$ simulated by an instantaneous increase in $\bar{\lambda}$ from 30 to 180. **B.** Length and radius dynamics following a hyperosmotic shock. The rate of change in length decreases at $t = 0$ and upon a division event, the subsequent division and birth lengths decrease with respect to the pre-shock values **C.** Growth rate dynamics following a hypoosmotic shock at $t = 0$ simulated by an instantaneous decrease in $\bar{\lambda}$ from 30 to 15. **D.** Steady state growth rate after osmotic shocks for different values of $\bar{\lambda}$. A and C indicate the values used in panels **A** and **C**.

# Chapter 6

# Conclusions, discussions and future work

One of the central questions of my work has been what is the connection between cell size and nutrient-imposed growth rate (the *nutrient growth law*) and how the scaling between cell size and growth rate arises at the single-cell level via coordination between cell growth and division. While this question is seemingly simple, it requires a molecular-level understanding of what sets the adder behaviour in cells and how do bacteria manage to measure the added size in different growth media. Using a coarse-grained model of cell growth based on proteome allocation theory, extended to include modules for cell size and division control, we found out that a balanced allocation of resources sets the size of bacteria (Figure 6.1 **A**). Based on this principle, the resources allocated to a particular proteomic sector are inversely proportional to the efficiency of that sector [95]. In nutrient-rich media, cells invest more ribosomal resources to growth thus compensating for a lower translational capacity that can arise from an increased dilution rate of ribosomes under fast growth conditions. In nutrient-poor media, cells have a lower nutritional capacity that they compensate by allocating more resources to metabolism and division protein synthesis.

Comparing our theory to experimental data, we uncover several feedback pathways

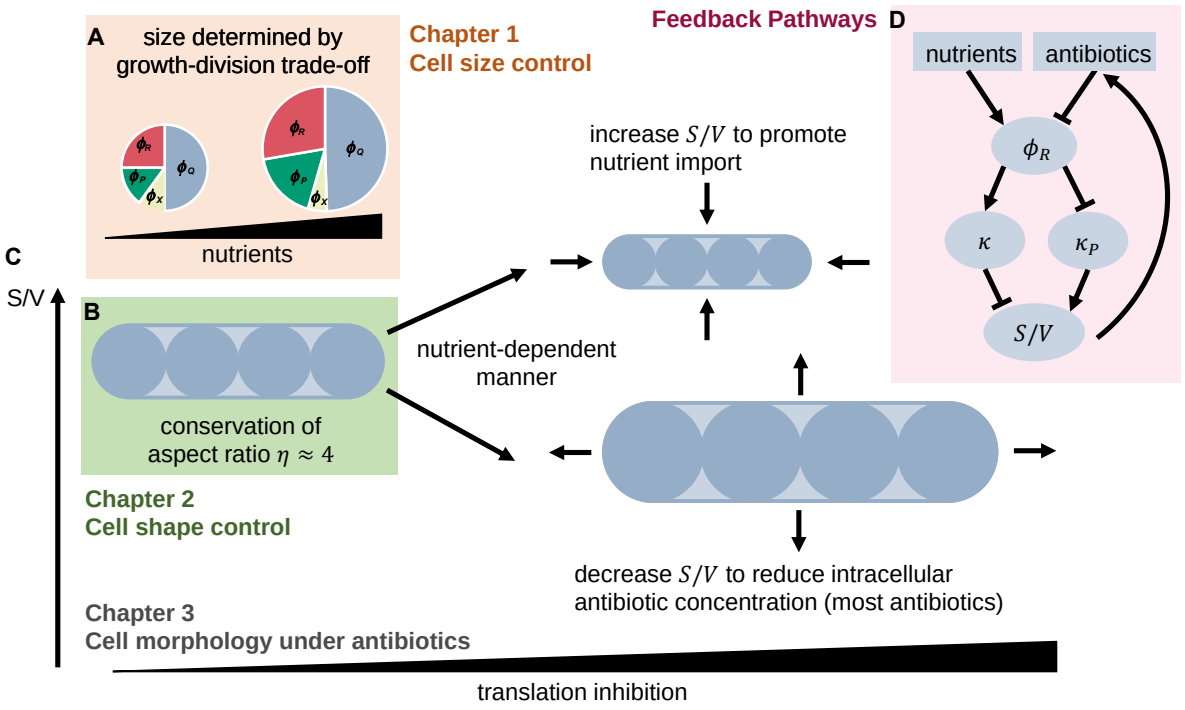


Figure 6.1: **Graphic summary of the work presented in this thesis. A.** The bacterial cell size is determined by a trade-off between resources invested in growth and division. In nutrient-rich conditions, cells have an increased ribosomal sector mass fraction $\phi_R$ which leads to high growth rates and large sizes. Conversely, in nutrient-poor conditions, cells allocate less resources to the growth rates and increase the division proteins sector mass fraction $\phi_X$ which results in smaller cells. **B.** Cells control their shapes across growth conditions by maintaining a constant aspect ratio on average ($\approx 4$ for *E. coli* cells) which leads to a conserved scaling relation between cell surface area and volume $S \propto V^{2/3}$. **C.** Diagram showing how *E. coli* cells change morphology under translation inhibition induced by Chloramphenicol in a nutrient-dependent manner. Bacteria growing in nutrient-poor conditions increase the volume to decrease the surface-to-volume ratio and reduce the intracellular antibiotic concentration, whereas bacteria growing in rich conditions increase the surface-to-volume ratio to promote nutrient influx. As shown in Figure 4.1 *E. coli cells* tend to decrease $S/V$ when treated with a wide variety of cytosolic antibiotics, and increase $S/V$ when treated with membrane-targeting antibiotics.

Figure 6.1: Continued caption. **D.** Feedback diagram showing the surface-to-volume regulation by growth rate $\kappa$ and division proteins synthesis rate $\kappa_P$.

between cell shape, growth rate, protein synthesis and extracellular transport that were previously unknown (Figure 6.1 **D**). In particular, we predict that under translation inhibition, cells break the balanced trade-off between ribosomes and division protein synthesis, leading to cell size inflation, reduction or size invariance, in a nutrient-dependent manner (Figure 6.1 **C**). If cells are grown in nutrient-rich media, the excess ribosomes produced under translation inhibition are allocated towards division, leading to smaller cell sizes and higher surface-to-volume ratios. Conversely, in nutrient-poor media cells allocate excess ribosomes towards growth, leading to cell size inflation and lower surface-to-volume ratios.

To understand the different responses of cell volume under translation inhibition we studied the behavior of cell surface-to-volume ratio to characterise cell shape. Interestingly, *E. coli* cells maintain a constant aspect ratio on average (Figure 6.1 **B**) for a wide range of perturbations that do not alter the division machinery and therefore conserve the surface-to-volume scaling $S \propto V^{2/3}$. Our results suggest that cells shape changes in response to translation-inhibitory antibiotics may confer certain fitness advantages under stress. In nutrient-rich media it is more favorable for cells to reduce their surface-to-volume in order to minimize antibiotic influx. However, in nutrient-poor media, cells adapt to import more nutrients by increasing their surface-to-volume ratios.

Coarse-grained proteome partitioning models [4, 8] come with the challenge of identifying the proteome sector to which the protein of interest belongs or if a new sector has to be included. In recent work, it has been suggested that the division proteins belong to the non-ribosomal $P$-sector [32, 5, 66], while others considered a separate proteome sector for division proteins [15, 174, 65]. By accounting for a separate division protein sector, we showed that the division protein sector behaves as a sub-class of $P$-sector proteins, given there is a negative correlation between protein mass fractions of $X$-sector and $R$-sector

proteins under nutrient perturbations [65]. Existing data support this model and also exclude other possible models of division proteins belonging to the $R$- or $Q$- sectors. For instance, if the division molecule is in the $R$-sector, then we expect $\kappa_p$ to be positively correlated with ribosome mass fraction in all conditions. Therefore, under translation inhibition we expect $\kappa_p$ to increase. Since growth rate decreases under translation inhibition, we would predict cell volume to decrease for all conditions. This is inconsistent with experimental data [5]. However, if the division proteins are in the $Q$-sector, then the invariance of $Q$-sector with nutrient shifts and translation inhibition would imply a constant division protein synthesis rate for all conditions. Therefore cell size would always decrease under translation inhibition, inconsistent with experimental data. Hence the division protein sector needs to be in the non-ribosomal sector to capture the tradeoff between the rates of growth and division protein synthesis under nutrient perturbations.

It is important to note that the model presented in Chapter 2 for cell size control is based on cells grown in a medium where nutrients are readily available and the flux of nutrients (or equivalently the amino acid concentration inside the cell) is constant. However this is rarely the case in nature, bacteria constantly compete with other organisms for resources and the nutrient environments fluctuate. One approach is to think of the ribosomal and metabolic efficiencies in a dynamic way (i.e. $\kappa_t = \kappa_t(t)$ and $\kappa_n = \kappa_n(t)$) or as amino-acid concentration dependent [8] to understand the transitions between growth conditions.

The phenomenological growth laws that allow us to predict how bacterial cells regulate their grow rates, proteome composition, cell shape and size are formulated for steady-state growth conditions. We currently have a limited understanding of the dynamics of cellular state variables in non-steady state conditions. With recent developments in high-throughput imaging and single-cell studies of bacterial growth, understanding the cells' behaviors during transition from one growth condition to another is of great interest [169, 33, 175, 176, 137, 17, 132]. Recent single-cell studies show that during single nutrient shifts [17, 66] or antibiotic treatments [132] bacterial cells preserve their size

control strategies, indicating that the division proteins are actively regulated in changing environments. When subject to nutrient fluctuations between low and high concentrations of nutrients [177], cells adopt a growth rate that cannot be predicted from the individual growth rates in poor and rich nutrient conditions as predicted by the Monod's law (Eq. 1.1), indicating that the relationship between ribosomes and growth rate does not hold in non-steady conditions. This adaptive mechanism leads to an interesting hypothesis that has been previously formulated in the context of fast transition to a new environmental condition. For instance, bacterial cells have a ribosome reserve arising from the inactive ribosomes that do not participate in translation. This inactive fraction allows cells to rapidly produce proteins in optimal amounts for the new growth condition [169, 45]. How resource allocation strategies are achieved during fast changing environments and whether growth-division tradeoff model still holds for non-steady fluctuating environments remains an open question.

I would like to highlight some interesting results presented in this thesis that would be interesting to explore further in theory or test experimentally. We derived the negative correlation between growth rate and division protein synthesis rate from a molecular level, by extending the three-component proteome setor model proposed by [4] to a four-component proteome sector model by including the division protein sector. So far the synthesis rate of division proteins (FtsZ) has been measured in one growth condition only [12], but it would be interesting to test the negative correlation with growth rate across nutrient conditions and the positive correlation under translation inhibition.

In Chapter 4, we fitted the growth inhibition curves (growth rate versus antibiotic concentration) to obtain the free parameters in the model. As we show in Figure 4.2 **D**, the ratio between the inward and outward membrane permeabilities increases with decreasing nutrient quality. This suggests that the membrane permeability is nutrient-dependent. It would be interesting to measure the membrane permeabilities in different growth conditions as a proxy for the permeability to antibiotics.

The results from Chapter 4 show that cells shape changes in response to translation-

inhibitory antibiotics may confer certain fitness advantages under stress. In nutrient-rich media it is more favorable for cells to reduce their surface-to-volume in order to minimize antibiotic influx. Whereas in nutrient-poor media, cells adapt to import more nutrients by increasing their surface-to-volume ratios. To quantitatively test the role of cell shape and nutrient quality on bacterial growth inhibition under antibiotic stress, we simulated bacterial growth under simultaneous perturbation of surface area production and translation inhibition in varying nutrient media. We find out that that round-shaped cells are fitter and more drug-resistant than higher aspect ratio filamentous cells, and that dose-sensitivity increases with increasing nutrient quality. These results can be tested experimentally by measuring bacterial growth rates in response to simultaneous application of cell-wall targeting and ribosome-targeting antibiotics, in different nutrient concentrations. Can growth inhibition be maximized by simultaneously inhibiting ribosomal translation and promoting surface area production in nutrient-poor media?

# Chapter 7

# Appendix

## METHOD DETAILS

### 7.1 Cell growth simulations - Chapter 4

To investigate the dynamic response of cell shape and growth to applied antibiotic and nutrient shifts, we simulated single-cell growth over multiple generations. We first initiated cells at random stages in their cell cycle, and upon division followed the daughter cells over a number of generations until steady-state is reached. During each cell generation $i$, we evolved the following seven coupled differential equations for cell volume $V_i$, division protein abundance $X_i$, surface area $A_i$, nutrient concentration inside the cell $[n_i]$, antibiotic concentration inside the cell $a^i_{in}$, active ribosomes $r^i_a$, and inactive or antibiotic-bound ribosomes, $r^i_b$.

$$\frac{dV_i}{dt} = \kappa(r^i_a)V_i(t), \tag{7.1}$$

$$\frac{dX_i}{dt} = \kappa_p(r^i_a)V_i(t) - \mu X_i(t), \tag{7.2}$$

$$\frac{dA_i}{dt} = \beta(r^i_a)V_i(t), \tag{7.3}$$

$$\frac{d\left[n_i\right]}{dt} = J_n([n_i], A_i, V_i) - \kappa(r^i_a)[n_i] - \kappa_r r^i_a, \tag{7.4}$$

$$\frac{da^i_{\text{in}}}{dt} = -\kappa(r^i_a)a^i_{\text{in}} + f(a^i_{\text{in}}, r^i_a, r^i_b) + J_a(a^i_{\text{in}}, [n_i], A_i, V_i), \tag{7.5}$$

$$\frac{dr^i_a}{dt} = -\kappa(r^i_a)r^i_a + f(a^i_{\text{in}}, r^i_a, r^i_b) + s(r^i_a, [n_i]), \tag{7.6}$$

$$\frac{dr^i_b}{dt} = -\kappa(r^i_a)r^i_b - f(a^i_{\text{in}}, r^i_a, r^i_b). \tag{7.7}$$

In the above equations, we have (dropping $'i'$ for simplicity):

$\kappa(r_a) = \kappa_t(r_a - r_{\min})$.

$\kappa_p(r_a) = \kappa^0_p(r^*_{\max} - r_a)$.

$\beta(r_a) = \nu[\kappa(r_a)]^{2/3}[\kappa_p(r_a)]^{1/3}$.

$J_n(A, V, [n]) = [n_{\text{ext}}]P_{\text{in}}([n])A/V$, where $[n_{\text{ext}}]$ is the extracellular nutrient concentration, and $P_{\text{in}}([n])$ is the nutrient-dependent inward permeability (Figure 3E)

$f(a_{\text{in}}, r_a, r_b) = -k_{\text{on}}a_{\text{in}}(r_a - r_{\min}) + k_{\text{off}}r_b$.

$J_a(a_{\rm in},[n],A,V) = (P_{\rm in}([n])a_{\rm ex} - P_{\rm out}a_{\rm in})A/V$.
$s(r_a,[n])) = \kappa(r_a)(r_{\rm max} - \kappa(r_a)(r_{\rm max} - r_{\rm min})(\kappa_{\rm specific}([n])^{-1} - \kappa_t/(r_{\rm max} - r_{\rm min}))$.
$\kappa_{\rm specific}([n]) = \kappa_0[n]/([n] + n^*)$.

For each cell cycle $i$, Eq. (7.1)-(7.7) are evolved for $t \leq \tau_i$, where $\tau_i$ is the interdivision time for the $i^{\rm th}$ generation. Division is triggered when $X_i > X_0$, with $X_0$ a constant. Upon division, we set: $V_{i+1}(0) = D_R V_i(\tau_i)$, $X_{i+1}(0) = 0$, $A_{i+1}(0) = D_R A_i(\tau_i)$, $[n_{i+1}](0) = [n_i](\tau_i)$, $a_{\rm in}^{i+i}(0) = a_{\rm in}^i(\tau_i)$, $r_a^{i+1}(0) = r_a^i(\tau_i)$, $r_b^{i+1}(0) = r_b^i(\tau_i)$, where $D_R$ is a Gaussian random variable with mean 0.5 and standard deviation 0.05. We initialize the nutrient concentration inside the cell ($[n_i]$) close to zero, and calibrate the extracellular nutrient concentration $[n_{\rm ext}]$ to reach the growth rate of the medium we choose to simulate. Over time $[n_i]$ reaches the steady-state value $n^*\kappa_{\rm specific}/(\kappa_0 - \kappa_{\rm specific})$, such that $\kappa = \kappa_{\rm specific}$. We run simulations for additional 5h after the nutrient concentration reaches steady-state, to record the average values of cell volume, area, and ribosome concentration. Antibiotic perturbation is applied after 10h from the start of the simulations and continued for another 20h, when we compute the average values for the various cellular variables.

## QUANTIFICATION AND STATISTICAL ANALYSIS

### 7.2 Parameter determination - Chapters 2 and 4

We extracted the parameters $\kappa_t$ and $r_{\rm min}$ by fitting the equation $\kappa = \kappa_t(r - r_{\rm min})$ to the data for growth rate vs RNA/protein ratio [9] (Table 7.1). Using our theoretical model, we obtained the expression for cell volume $V$ as a function of $r$ (Eq. (2.6)), which we fitted to experimental data [9], in order to to extract the parameters $\kappa_p^0$, $r_{\rm max}^*$ and $\mu$ (Tables 7.1 and 7.2). For cells under Chloramphenicol stress, the nutrient-dependent parameters $\kappa_n$ and $\delta r$ were obtained by fitting Eq. (2.20) and Eq. (2.21) to the experimental dataset for each nutrient condition (Tables 7.1 and 7.2). From experimental data [9], we estimated the division protein production rate as $\kappa_p = \kappa/\langle V\rangle$. To determine the permeability of the cell envelope to nutrient and antibiotic transport, we fitted the growth inhibition curves resulting from our simulations to the growth inhibition curves from the data in [9], using

a method of least-squares. We find that $P_{\text{in}}/P_{\text{out}}$ is a function of nutrient quality, and used that as an input to our model simulations. Tables 7.1, 7.2 and 7.3 list a complete set of parameter values used in our model simulations. Note that there are free parameters in the model that are not fixable by fitting experimental data. These include: $X_0$, $n^*$ and $\kappa_0$. We do not use $X_0$ directly, as the value is absorbed in $\kappa_p$ by re-normalising the number of division proteins by $X_0$ i.e. $X\left(t=0\right)=0$ and $X\left(t=\tau\right)=X_0=1$. We determine the nutrient specific growth rate by treating $[n_{\text{ext}}]/n^*$ as a fitting parameter. To this end, we arbitrarily pick the values for $n^*$ and $\kappa_0$ and let the nutrients inside the cell to reach steady-state, $d[n]/dt=0$. The steady-state value for $[n]$ depends on $[n_{ext}]$ and determines the nutrient-specific growth rate $\kappa=\kappa_{\text{specific}}=\kappa_0\left[n\right]/(n^*+[n])$. For each growth medium, we tune the value of $[n_{ext}]/n^*$ such that it results in the value of $\kappa$ equal to the growth rate reported in experiments.

### 7.3 Cell growth simulations - Chapter 5

We pick an arbitrary value of $\gamma$ to set the threshold $X_0$. Knowing $\eta$ from experimental data and the growth rate $\kappa$ from Eq. (5.13), we can then determine the division protein synthesis rate $k_P$.

I start with $\kappa_0=1h^{-1}$ the initial growth rate, and $L^*$ the initial length at birth. I calculate $R^*\approx(L^*/\eta)/2$ and the threshold value for division $X_0=\gamma 2R$. I set a random value for $X=X_{birth}$ such that $X_{birth}<\gamma 2R$. Then from the first initial condition (Eq. 5.17) I calculate $\bar{\mu_L}$ and from the second initial condition (Eq. 5.18) I calculate $dU$ (and $\bar{\epsilon}$). This implies that I already know the following: $\bar{\lambda}$, $\bar{g}$, $\mu_0$, $k_c$, $R_0$, $\mu_R$.

As long as $X(t)<X0$, each time step $dt$ I calculate the following:

1. the energies $E$, $U$, $dU$
2. the growth rates $\kappa$, $\kappa_r$ and $\kappa_p$
3. the changes in length, radius and division protein numbers: $dL/dt=\kappa L$, $dR/dt=\kappa_r R$ and $dX/dt=\kappa_p L$.

When $X>X0$, I divide the cell: $L=L/2$, $R=R$ and $X=X_{birth}$, with some error in length .

Nutrient shift - I change $\epsilon$ after a division event and carry on with steps 1)-3). Here I constantly recalculate $X0 = \gamma 2R$ to account for the fact that the radius has not yet reached the steady state value and the threshold is not fixed.

Table 7.1: **List of parameters used in models of growth perturbations (Figures 2.1,2.2,2.3,4.2,4.3).**

| Parameter | Value | Growth medium | Expression/method used | Figure number |
|---|---|---|---|---|
| $\phi_R^{\min}$ | 0.1 | all | $\kappa = \kappa_t(r - r_{\min})$ | 2.1, 2.2, 2.3, 4.2, 4.3 |
| $\kappa_t(\mathrm{h}^{-1})$ | 5.6 | all | | |
| $\kappa_p^0(\mathrm{h}^{-1}\mu\mathrm{m}^{-3})$ | 2.1 | all | Eq. (5) | 2.1, 2.2, 2.3, 4.2, 4.3 |
| $\phi_R^{max^*}$ | 0.7 | all | | |
| $\mu(\mathrm{h}^{-1})$ | 0.24 | all | | 2.1 |
| $\phi_R^{max} - \phi_X$ | 0.76 | TSB | $\kappa = \kappa_n(r_{\max} - r_X - r)$ | 2.3, 4.2, 4.3 |
| | 0.92 | synthetic rich | | |
| | 0.76 | glucose + 12a.a. | | |
| | 0.54 | casamino acid | | |
| | 0.58 | glucose + 6a.a. | | |
| | 0.74 | glucose | | |
| | 0.64 | glycerol | | |
| | 0.29 | sorbitol | | |
| | 0.23 | mannose | | |
| $\kappa_n(\mathrm{h}^{-1})$ | 9.1 | TSB | $\kappa_p = \frac{\kappa_p^0}{\kappa_n}\kappa + \kappa_p^0\delta r$ | 2.3, 4.2, 4.3 |
| | 8.9 | synthetic rich | | |
| | 3.4 | glucose + 12a.a. | | |
| | 3.5 | casamino acid | | |
| | 3.4 | glucose + 6a.a. | | |
| | 2.2 | glucose | | |
| | 1.1 | glycerol | | |
| | 1.6 | sorbitol | | |
| | 1.4 | mannose | | |

Table 7.2: **List of parameters used in models of growth perturbations (Figures 1-4).**

| Parameter | Value | Growth medium | Expression/method used | Figure number |
|---|---|---|---|---|
| $\delta r$ | 0.37 | TSB | $\kappa_p = \kappa_p^0(r_{\max} - r_X + \delta r - r)$ | 2.3, 4.2, 4.3 |
| | 0.13 | synthetic rich | | |
| | -0.18 | glucose + 12a.a. | | |
| | 0.08 | casamino acid | | |
| | -0.04 | glucose + 6a.a. | | |
| | 0.07 | glucose | | |
| | -0.1 | glycerol | | |
| | -0.4 | sorbitol | | |
| | -0.43 | mannose | | |
| $\kappa_m(\mathrm{h}^{-1})$ | 2.6 | all | $\kappa_n = \kappa_t \frac{\kappa}{\kappa_m - \kappa}$ | 2.3 |
| $\kappa_r(\mathrm{h}^{-1})$ | 0.6 | all | calibrated | 4.2, 4.3 |
| $\kappa_0(\mathrm{h}^{-1})$ | 3 | all | calibrated | 4.2, 4.3 |

Table 7.3: **List of parameters used in antibiotic simulations (Figures 4.2- 4.3)**

| Parameter | Value | Growth medium | Expression/method used | Figure number |
|---|---|---|---|---|
| $[n_{\text{ext}}]/n^*$ | 0.2 | TSB | Fitting $\kappa = \kappa_0 \frac{[n]}{[n]+n^*}$ when $\frac{d[n]}{dt} = 0$ | 4.2, 4.3 |
| | 0.08 | synthetic rich | | |
| | 0.03 | glucose + 12a.a. | | |
| | 0.05 | casamino acid | | |
| | 0.018 | glucose + 6a.a. | | |
| | 0.008 | glucose | | |
| | 0.002 | glycerol | | |
| $P_{\text{out}}(\text{h}^{-1}\mu\text{m}^{-1})$ | 20 | all | $15 - 30$ h$^{-1}$ [144] | 4.2, 4.3 |
| $P_{\text{in}}/P_{\text{out}}$ | 0.45 | TSB | Fitting growth inhibition curves | 4.2, 4.3 |
| | 0.80 | synthetic rich | | |
| | 0.88 | glucose + 12a.a. | | |
| | 0.80 | casamino acid | | |
| | 0.85 | glucose + 6a.a. | | |
| | 1.6 | glucose | | |
| | 2.1 | glycerol | | |
| | 10 | sorbitol | | |
| | 15 | mannose | | |
| $k_{\text{on}}(\mu\text{M}^{-1}\text{h}^{-1})$ | 10 | all | $1.08 - 13$ $\mu$M$^{-1}$h$^{-1}$ [144] | 4.2, 4.3 |
| $k_{\text{D}}(\mu\text{M})$ | 2.5 | all | $0.5 - 5$ $\mu$M [144] | 4.2, 4.3 |
| $k_{\text{off}}(\text{h}^{-1}) = k_{\text{D}}k_{\text{on}}$ | 25 | all | calculated | 4.2, 4.3 |

Table 7.4: **Energy expressions** (used in Figure 5.4)

| **Energy type** | **Equation** |
|---|---|
| intake energy (average) | $E_{in} = \epsilon A$ |
| energy dissipated (per cell cycle) | $E_{dissip} \approx \mathscr{D}\tau_{cyc} = \left(\pi RL\left(\eta_L\kappa_L^2 + \eta_R\kappa_R^2\right) + \frac{\xi L}{2\pi R^2}{\kappa_P^{(L)}}^2\right)\frac{1}{\kappa}log(2)$ |
| mechanical energy (average) | $E_{mech} = k_c\pi RL\left(\frac{1}{R} - \frac{1}{R_0}\right)^2 + \lambda\pi R^3 L$ |
| maintenance energy (average) | $E_M = g\pi R^2 L$ |
| division energy (at division) | $E_{div} = -\kappa_P^{(V)}\xi 2\pi R\gamma = -\frac{\kappa_P^{(L)}}{\pi R^2}\xi 2\pi R\gamma = \kappa_P^{(L)} 2\xi\gamma/R$ |
| **Energy rate** | **Equation** |
| rate of intake energy | $\frac{dE_{in}}{dt} = \left(g\kappa_R R + 3\lambda\kappa_R R^2 + \frac{R-R_0}{R_0R^2} + \frac{\kappa_R}{RR_0} - \frac{2(R-R_0)}{R_0R^2}\kappa_R\right)A$ |
| dissipation rate | $\frac{dE_{dissip}}{dt} = \frac{1}{2}hA(\eta_L\kappa^2 + \eta_R\kappa_R^2) + \frac{\xi}{2\pi R}\kappa_P^2\eta$ |
| rate of mechanical energy | $\frac{dE_{mech}}{dt} = k_c\pi RL\left(\frac{1}{R} - \frac{1}{R_0}\right)^2(\kappa_R + \kappa) - 2k_c\pi L\kappa_R\left(\frac{1}{R} - \frac{1}{R_0}\right)$ |
| rate of maintenance energy | $\frac{dE_M}{dt} = \pi R^2 L\left(\kappa + 2\kappa_R\right)$ |
| rate of division energy | $\frac{dE_{div}}{dt} = -\mu\kappa_P L$ |

Table 7.5: **List of parameters used in Fig. 5.2, 5.3, 5.4**

| **parameter** | **value** | **how it is obtained** |
|---|---|---|
| $\bar{\lambda}$ | 30 | estimated |
| $\bar{g}$ | 30 | fitted from nutrient growth law |
| $R_0$ | 0.3 | estimated |
| $\bar{\mu_R}$ | 0.1 | fitted from nutrient growth law, used in Fig. 2-4 |
| $\bar{\mu_L}$ | 0.0807 | average value, used in Fig. 4 |
| $\eta$ | 1.5-3 | calculated from data |

# Bibliography

[1] Suckjoon Jun, Fangwei Si, Rami Pugatch, and Matthew Scott. Fundamental principles in bacterial physiology—history, recent progress, and the future with focus on cell size control: a review. *Reports on Progress in Physics*, 81(5):056601, 2018.

[2] Jes Forchhammer and Lasse Lindahl. Growth rate of polypeptide chains as a function of the cell growth rate in a mutant of escherichia coli 15. *Journal of Molecular Biology*, 55(3):563–568, 1971.

[3] Hans Bremer and Patrick P Dennis. Escherichia coli and salmonella: cellular and molecular biology. *Washington (DC): American Society for Microbiology. Chapter, Modulation of chemical composition and other parameters of the cell by growth rate*, pages 1553–1569, 1996.

[4] Matthew Scott, Carl W Gunderson, Eduard M Mateescu, Zhongge Zhang, and Terence Hwa. Interdependence of cell growth and gene expression: origins and consequences. *Science*, 330(6007):1099–1102, 2010.

[5] Fangwei Si, Dongyang Li, Sarah E Cox, John T Sauls, Omid Azizi, Cindy Sou, Amy B Schwartz, Michael J Erickstad, Yonggun Jun, Xintian Li, et al. Invariance of initiation mass and predictability of cell size in escherichia coli. *Current Biology*, 27(9):1278–1287, 2017.

[6] Alexander Schmidt, Karl Kochanowski, Silke Vedelaar, Erik Ahrné, Benjamin Volkmer, Luciano Callipo, Kevin Knoops, Manuel Bauer, Ruedi Aebersold, and

Matthias Heinemann. The quantitative and condition-dependent escherichia coli proteome. *Nature Biotechnology*, 34(1):104–110, 2016.

[7] Parth Pratim Pandey and Sanjay Jain. Analytic derivation of bacterial growth laws from a simple model of intracellular chemical dynamics. *Theory in Biosciences*, 135 (3):121–130, 2016.

[8] Matthew Scott, Stefan Klumpp, Eduard M Mateescu, and Terence Hwa. Emergence of robust growth laws from optimal regulation of ribosome synthesis. *Molecular systems biology*, 10(8):747, 2014.

[9] Fangwei Si, Dongyang Li, Sarah E. Cox, John T. Sauls, Omid Azizi, Cindy Sou, Amy B. Schwartz, Michael J. Erickstad, Yonggun Jun, Xintian Li, and Suckjoon Jun. Invariance of Initiation Mass and Predictability of Cell Size in Escherichia coli. *Current Biology*, 27(9):1278–1287, May 2017. ISSN 09609822. doi:10.1016/j.cub.2017.03.022. URL `https://linkinghub.elsevier.com/retrieve/pii/S0960982217302919`.

[10] M. Scott, C. W. Gunderson, E. M. Mateescu, Z. Zhang, and T. Hwa. Interdependence of Cell Growth and Gene Expression: Origins and Consequences. *Science*, 330(6007):1099–1102, November 2010. ISSN 0036-8075, 1095-9203. doi:10.1126/science.1192588. URL `http://www.sciencemag.org/cgi/doi/10.1126/science.1192588`.

[11] M. Schaechter, O. MaalØe, and N. O. Kjeldgaard. Dependency on Medium and Temperature of Cell Size and Chemical Composition during Balanced Growth of Salmonella typhimurium. *Microbiology*, 19(3):592–606, 1958. doi:10.1099/00221287-19-3-592. URL `https://mic.microbiologyresearch.org/content/journal/micro/10.1099/00221287-19-3-592`.

[12] Fangwei Si, Guillaume Le Treut, John T Sauls, Stephen Vadia, Petra Anne Levin,

and Suckjoon Jun. Mechanistic origin of cell-size control and homeostasis in bacteria. *Current Biology*, 29(11):1760–1770, 2019.

[13] Hai Zheng, Yang Bai, Meiling Jiang, Taku A Tokuyasu, Xiongliang Huang, Fajun Zhong, Yuqian Wu, Xiongfei Fu, Nancy Kleckner, Terence Hwa, et al. General quantitative relations linking cell growth and the cell cycle in escherichia coli. *Nature Microbiology*, 5(8):995–1001, 2020.

[14] Manlu Zhu, Xiongfeng Dai, Weilun Guo, Zengxiang Ge, Mingxuan Yang, Haikuan Wang, and Yi-Ping Wang. Manipulating the bacterial cell cycle and cell size by titrating the expression of ribonucleotide reductase. *MBio*, 8(6), 2017.

[15] Markus Basan, Manlu Zhu, Xiongfeng Dai, Mya Warren, Daniel Sévin, Yi-Ping Wang, and Terence Hwa. Inflating bacterial cells by increased protein synthesis. *Molecular systems biology*, 11(10):836, 2015.

[16] Poochit Nonejuie, Michael Burkart, Kit Pogliano, and Joe Pogliano. Bacterial cytological profiling rapidly identifies the cellular pathways targeted by antibacterial molecules. *Proceedings of the National Academy of Sciences*, 110:201311066, 2013.

[17] Leigh K Harris and Julie A Theriot. Relative rates of surface and volume synthesis set bacterial cell size. *Cell*, 165(6):1479–1492, 2016.

[18] Stephen Vadia, L Tse Jessica, Rafael Lucena, Zhizhou Yang, Douglas R Kellogg, Jue D Wang, and Petra Anne Levin. Fatty acid availability sets cell envelope capacity and dictates microbial cell size. *Current Biology*, 27(12):1757–1767, 2017.

[19] Manuel Campos, Sander K Govers, Irnov Irnov, Genevieve S Dobihal, François Cornet, and Christine Jacobs-Wagner. Genomewide phenotypic analysis of growth, cell morphogenesis, and cell cycle events in escherichia coli. *Molecular Systems Biology*, 14(6):e7573, 2018.

[20] William T Gray, Sander K Govers, Yingjie Xiang, Bradley R Parry, Manuel Campos, Sangjin Kim, and Christine Jacobs-Wagner. Nucleoid size scaling and intracellular organization of translation across bacteria. *Cell*, 177(6):1632–1648, 2019.

[21] F. Sato. Helicobacter pylori in culture: an ultrastructural study. *[Hokkaido Igaku Zasshi] The Hokkaido Journal of Medical Science*, 75(3):187–196, May 2000. ISSN 0367-6102.

[22] Shlomo Trachtenberg. Shaping and Moving a *Spiroplasma*. *Journal of Molecular Microbiology and Biotechnology*, 7(1-2):78–87, 2004. ISSN 1660-2412, 1464-1801. doi:10.1159/000077872. URL `https://www.karger.com/Article/FullText/77872`.

[23] Andrew E Pelling, Yinuo Li, Wenyuan Shi, and James K Gimzewski. Nanoscale visualization and characterization of myxococcus xanthus cells with atomic force microscopy. *Proceedings of the National Academy of Sciences*, 102(18):6484–6489, 2005.

[24] Charles S Wright, Shiladitya Banerjee, Srividya Iyer-Biswas, Sean Crosson, Aaron R Dinner, and Norbert F Scherer. Intergenerational continuity of cell shape dynamics in caulobacter crescentus. *Scientific Reports*, 5:9155, 2015.

[25] Maxime Deforet, Dave Van Ditmarsch, and Joao B Xavier. Cell-size homeostasis and the incremental rule in a bacterial pathogen. *Biophysical journal*, 109(3):521–528, 2015.

[26] Samantha M Desmarais, Carolina Tropini, Amanda Miguel, Felipe Cava, Russell D Monds, Miguel A de Pedro, and Kerwyn Casey Huang. High-throughput, highly sensitive analyses of bacterial morphogenesis using ultra performance liquid chromatography. *Journal of Biological Chemistry*, 290(52):31090–31100, 2015.

[27] Nikola Ojkic, Javier López-Garrido, Kit Pogliano, and Robert G Endres. Cell-wall

remodeling drives engulfment during bacillus subtilis sporulation. *Elife*, 5:e18657, 2016.

[28] DT Quach, G Sakoulas, V Nizet, J Pogliano, and K Pogliano. Bacterial cytological profiling (bcp) as a rapid and accurate antimicrobial susceptibility testing method for staphylococcus aureus. *EBioMedicine*, 4:95–103, 2016.

[29] Valerie J Carabetta, Todd M Greco, Andrew W Tanner, Ileana M Cristea, and David Dubnau. Temporal regulation of the bacillus subtilis acetylome and evidence for a role of mreb acetylation in cell wall growth. *Msystems*, 1(3):e00005–16, 2016.

[30] Sandip Chattopadhyay, Sarah D. Perkins, Matthew Shaw, and Tonya L. Nichols. Evaluation of exposure to Brevundimonas diminuta and Pseudomonas aeruginosa during showering. *Journal of Aerosol Science*, 114:77–93, December 2017. ISSN 00218502. doi:10.1016/j.jaerosci.2017.08.008. URL `https://linkinghub.elsevier.com/retrieve/pii/S0021850217301441`.

[31] Javier López-Garrido, Nikola Ojkic, Kanika Khanna, Felix R Wagner, Elizabeth Villa, Robert G Endres, and Kit Pogliano. Chromosome translocation inflates bacillus forespores and impacts cellular morphology. *Cell*, 172(4):758–770, 2018.

[32] Sattar Taheri-Araghi, Serena Bradde, John T Sauls, Norbert S Hill, Petra Anne Levin, Johan Paulsson, Massimo Vergassola, and Suckjoon Jun. Cell-size control and homeostasis in bacteria. *Current biology*, 25(3):385–391, 2015.

[33] David W Erickson, Severin J Schink, Vadim Patsalo, James R Williamson, Ulrich Gerland, and Terence Hwa. A global resource allocation strategy governs growth transition kinetics of escherichia coli. *Nature*, 551(7678):119–123, 2017.

[34] Diana Serbanescu, Nikola Ojkic, and Shiladitya Banerjee. Cellular resource allocation strategies for cell size and shape control in bacteria. *The FEBS Journal*, 2021.

[35] Kevin D Young. The selective value of bacterial shape. *Microbiology and molecular biology reviews*, 70(3):660–703, 2006.

[36] Jacques Monod. The growth of bacterial cultures. *Annual review of microbiology*, 3(1):371–394, 1949.

[37] Nathan M Belliveau, Griffin Chure, Christina L Hueschen, Hernan G Garcia, Jane Kondev, Daniel S Fisher, Julie A Theriot, and Rob Phillips. Fundamental limits on the rate of bacterial growth and their influence on proteomic composition. *Cell Systems*, 2021.

[38] Frederick C Neidhardt and Boris Magasanik. Studies on the role of ribonucleic acid in the growth of bacteria. *Biochimica et biophysica acta*, 42:99–116, 1960.

[39] RJ Harvey. Fraction of ribosomes synthesizing protein as a function of specific growth rate. *Journal of Bacteriology*, 114(1):287–293, 1973.

[40] Eyal Metzl-Raz, Moshe Kafri, Gilad Yaakov, Ilya Soifer, Yonat Gurvich, and Naama Barkai. Principles of cellular resource allocation revealed by condition-dependent proteome profiling. *Elife*, 6:e28034, 2017.

[41] Istvan T Kleijn, Amalia Martínez-Segura, François Bertaux, Malika Saint, Holger Kramer, Vahid Shahrezaei, and Samuel Marguerat. Growth-rate-dependent and nutrient-specific gene expression resource allocation in fission yeast. *Life science alliance*, 5(5), 2022.

[42] Douwe Molenaar, Rogier Van Berlo, Dick De Ridder, and Bas Teusink. Shifts in growth strategies reflect tradeoffs in cellular economics. *Molecular Systems Biology*, 5(1):323, 2009.

[43] Stefan Klumpp, Matthew Scott, Steen Pedersen, and Terence Hwa. Molecular crowding limits translation and cell growth. *Proceedings of the National Academy of Sciences*, 110(42):16754–16759, 2013.

[44] Frederick Carl Neidhardt, John L Ingraham, and Moselio Schaechter. *Physiology of the bacterial cell; a molecular approach*. Number 589.901 N397. Sinauer associates, 1990.

[45] Bin Ni, Remy Colin, Hannes Link, Robert G Endres, and Victor Sourjik. Growth-rate dependent resource investment in bacterial motile behavior quantitatively follows potential benefit of chemotaxis. *Proceedings of the National Academy of Sciences*, 117(1):595–601, 2020.

[46] Evert Bosdriesz, Douwe Molenaar, Bas Teusink, and Frank J Bruggeman. How fast-growing bacteria robustly tune their ribosome concentration to approximate growth-rate maximization. *The FEBS Journal*, 282(10):2029–2044, 2015.

[47] Arijit Maitra and Ken A Dill. Bacterial growth laws reflect the evolutionary importance of energy efficiency. *Proceedings of the National Academy of Sciences*, 112 (2):406–411, 2015.

[48] Andrea Y Weiße, Diego A Oyarzún, Vincent Danos, and Peter S Swain. Mechanistic links between cellular trade-offs, gene expression, and growth. *Proceedings of the National Academy of Sciences*, 112(9):E1038–E1047, 2015.

[49] Yael Korem Kohanim, Dikla Levi, Ghil Jona, Benjamin D Towbin, Anat Bren, and Uri Alon. A bacterial growth law out of steady state. *Cell Reports*, 23(10): 2891–2900, 2018.

[50] Moselio Schaechter, Ole Maaløe, and Niels O Kjeldgaard. Dependency on medium and temperature of cell size and chemical composition during balanced growth of salmonella typhimurium. *Microbiology*, 19(3):592–606, 1958.

[51] Frank J Trueba and Conrad L Woldringh. Changes in cell diameter during the division cycle of escherichia coli. *Journal of bacteriology*, 142(3):869–878, 1980.

[52] Stephen Vadia and Petra Anne Levin. Growth rate and cell size: a re-examination of the growth law. *Current opinion in microbiology*, 24:96–103, 2015.

[53] Xiongfeng Dai, Zichu Shen, Yiheng Wang, and Manlu Zhu. Sinorhizobium meliloti, a slow-growing bacterium, exhibits growth rate dependence of cell size under nutrient limitation. *MSphere*, 3(6), 2018.

[54] John T Sauls, Sarah E Cox, Quynh Do, Victoria Castillo, Zulfar Ghulam-Jelani, and Suckjoon Jun. Control of bacillus subtilis replication initiation during physiological transitions and perturbations. *Mbio*, 10(6), 2019.

[55] Ariel Amir. Cell size regulation in bacteria. *Physical review letters*, 112(20):208102, 2014.

[56] Shiladitya Banerjee, Klevin Lo, Matthew K Daddysman, Alan Selewa, Thomas Kuntz, Aaron R Dinner, and Norbert F Scherer. Biphasic growth dynamics control cell division in caulobacter crescentus. *Nature microbiology*, 2(9):1–6, 2017.

[57] Mats Wallden, David Fange, Ebba Gregorsson Lundius, Özden Baltekin, and Johan Elf. The synchronization of replication and division cycles in individual e. coli cells. *Cell*, 166(3):729–739, 2016.

[58] Clotilde Cadart, Larisa Venkova, Pierre Recho, Marco Cosentino Lagomarsino, and Matthieu Piel. The physics of cell-size regulation across timescales. *Nature Physics*, 15(10):993–1004, 2019.

[59] Manuel Campos, Ivan V Surovtsev, Setsu Kato, Ahmad Paintdakhi, Bruno Beltran, Sarah E Ebmeier, and Christine Jacobs-Wagner. A constant size extension drives bacterial cell size homeostasis. *Cell*, 159(6):1433–1446, 2014.

[60] Suckjoon Jun and Sattar Taheri-Araghi. Cell-size maintenance: universal strategy revealed. *Trends in microbiology*, 23(1):4–6, 2015.

[61] Matteo Osella, Eileen Nugent, and Marco Cosentino Lagomarsino. Concerted control of escherichia coli cell division. *Proceedings of the National Academy of Sciences*, 111(9):3431–3435, 2014.

[62] William D Donachie. Relationship between cell size and time of initiation of dna replication. *Nature*, 219(5158):1077–1079, 1968.

[63] Po-Yi Ho and Ariel Amir. Simultaneous regulation of cell size and chromosome replication in bacteria. *Frontiers in microbiology*, 6:662, 2015.

[64] Khem Raj Ghusinga, Cesar A Vargas-Garcia, and Abhyudai Singh. A mechanistic stochastic framework for regulating bacterial cell division. *Scientific reports*, 6(1): 1–9, 2016.

[65] Diana Serbanescu, Nikola Ojkic, and Shiladitya Banerjee. Nutrient-dependent trade-offs between ribosomes and division protein synthesis control bacterial cell size and growth. *Cell Reports*, 32(12):108183, 2020.

[66] Mia Panlilio, Jacopo Grilli, Giorgio Tallarico, Ilaria Iuliani, Bianca Sclavi, Pietro Cicuta, and Marco Cosentino Lagomarsino. Threshold accumulation of a constitutive protein explains e. coli cell-division behavior in nutrient upshifts. *Proceedings of the National Academy of Sciences*, 118(18), 2021.

[67] Nikola Ojkic, Diana Serbanescu, and Shiladitya Banerjee. Surface-to-volume scaling and aspect ratio preservation in rod-shaped bacteria. *Elife*, 8:e47033, 2019.

[68] Ariel Amir. Cell Size Regulation in Bacteria. *Physical Review Letters*, 112(20):208102, May 2014. ISSN 0031-9007, 1079-7114. doi:10.1103/PhysRevLett.112.208102. URL `https://link.aps.org/doi/10.1103/PhysRevLett.112.208102`.

[69] Shiladitya Banerjee, Klevin Lo, Matthew K. Daddysman, Alan Selewa, Thomas Kuntz, Aaron R. Dinner, and Norbert F. Scherer. Biphasic growth dynam-

ics control cell division in Caulobacter crescentus. *Nature Microbiology*, 2(9): 17116, September 2017. ISSN 2058-5276. doi:10.1038/nmicrobiol.2017.116. URL http://www.nature.com/articles/nmicrobiol2017116.

[70] Sattar Taheri-Araghi, Serena Bradde, John T. Sauls, Norbert S. Hill, Petra Anne Levin, Johan Paulsson, Massimo Vergassola, and Suckjoon Jun. Cell-Size Control and Homeostasis in Bacteria. *Current Biology*, 25(3):385–391, February 2015. ISSN 09609822. doi:10.1016/j.cub.2014.12.009. URL https://linkinghub.elsevier.com/retrieve/pii/S0960982214015735.

[71] Leigh K Harris and Julie A Theriot. Surface area to volume ratio: a natural variable for bacterial morphogenesis. *Trends in microbiology*, 26(10):815–832, 2018.

[72] Gabriele Micali, Jacopo Grilli, Matteo Osella, and Marco Cosentino Lagomarsino. Concurrent processes set e. coli cell division. *Science Advances*, 4(11):eaau3324, 2018.

[73] Gabriele Micali, Jacopo Grilli, Matteo Osella, and Marco Cosentino Lagomarsino. Concurrent processes set e. coli cell division. *Science Advances*, 4(11):eaau3324, 2018.

[74] Jacopo Grilli, Clotilde Cadart, Gabriele Micali, Matteo Osella, and Marco Cosentino Lagomarsino. The empirical fluctuation pattern of e. coli division control. *Frontiers in microbiology*, 9:1541, 2018.

[75] M. Kaczanowska and M. Ryden-Aulin. Ribosome Biogenesis and the Translation Process in Escherichia coli. *Microbiology and Molecular Biology Reviews*, 71(3): 477–494, September 2007. ISSN 1092-2172. doi:10.1128/MMBR.00013-07. URL http://mmbr.asm.org/cgi/doi/10.1128/MMBR.00013-07.

[76] S. Klumpp, M. Scott, S. Pedersen, and T. Hwa. Molecular crowding limits translation and cell growth. *Proceedings of the National Academy of*

*Sciences*, 110(42):16754–16759, October 2013. ISSN 0027-8424, 1091-6490. doi:10.1073/pnas.1310377110. URL http://www.pnas.org/cgi/doi/10.1073/pnas.1310377110.

[77] O. Maaløe. Regulation of the Protein-Synthesizing Machinery—Ribosomes, tRNA, Factors, and So On. In Robert F. Goldberger, editor, *Biological Regulation and Development: Gene Expression*, pages 487–542. Springer US, Boston, MA, 1979. ISBN 978-1-4684-3417-0. doi:10.1007/978-1-4684-3417-0_12. URL https://doi.org/10.1007/978-1-4684-3417-0_12.

[78] John Yin. Genome Function—A Virus-World View. In Lee K. Opresko, Julie M. Gephart, and Michaela B. Mann, editors, *Advances in Systems Biology*, pages 31–46, Boston, MA, 2004. Springer US. ISBN 978-1-4419-8861-4.

[79] RE Ecker and M Schaechter. Bacterial growth under conditions of limited nutrition. *Annals of the New York Academy of Sciences*, 102(3):549–563, 1963.

[80] Alon Zaslaver, Shai Kaplan, Anat Bren, Adrian Jinich, Avi Mayo, Erez Dekel, Uri Alon, and Shalev Itzkovitz. Invariant Distribution of Promoter Activities in Escherichia coli. *PLoS Computational Biology*, 5(10):e1000545, October 2009. ISSN 1553-7358. doi:10.1371/journal.pcbi.1000545. URL https://dx.plos.org/10.1371/journal.pcbi.1000545.

[81] Markus Basan, Manlu Zhu, Xiongfeng Dai, Mya Warren, Daniel Sévin, Yi-Ping Wang, and Terence Hwa. Inflating bacterial cells by increased protein synthesis. *Molecular Systems Biology*, 11(10):836, 2015.

[82] N. O. Kjeldgaard, O. MaalOe, and M. Schaechter. The Transition Between Different Physiological States During Balanced Growth of Salmonella typhimurium. *Journal of General Microbiology*, 19(3):607–616, December 1958. ISSN 0022-1287. doi:10.1099/00221287-19-3-607. URL https://www.microbiologyresearch.org/content/journal/micro/10.1099/00221287-19-3-607.

[83] Moselio Schaechter. From growth physiology to systems biology. *International Microbiology*, 9(3):157–161, 2006.

[84] Ao H Stouthamer and Corry Bettenhaussen. Utilization of energy for growth and maintenance in continuous and batch cultures of microorganisms: A reevaluation of the method for the determination of atp production by measuring molar growth yields. *Biochimica et Biophysica Acta (BBA)-Reviews on Bioenergetics*, 301(1): 53–70, 1973.

[85] T Ruusala, D Andersson, M Ehrenberg, and CG Kurland. Hyper-accurate ribosomes inhibit growth. *The EMBO Journal*, 3(11):2575–2580, 1984.

[86] David W. Adams and Jeff Errington. Bacterial cell division: assembly, maintenance and disassembly of the Z ring. *Nature Reviews Microbiology*, 7(9):642–653, September 2009. ISSN 1740-1526, 1740-1534. doi:10.1038/nrmicro2198. URL `http://www.nature.com/articles/nrmicro2198`.

[87] Lydia Robert. Size sensors in bacteria, cell cycle control, and size control. *Frontiers in Microbiology*, 6:515, 2015.

[88] Ingvild Flåtten, Solveig Fossum-Raunehaug, Riikka Taipale, Silje Martinsen, and Kirsten Skarstad. The DnaA Protein Is Not the Limiting Factor for Initiation of Replication in Escherichia coli. *PLOS Genetics*, 11(6):e1005276, June 2015. ISSN 1553-7404. doi:10.1371/journal.pgen.1005276. URL `http://dx.plos.org/10.1371/journal.pgen.1005276`.

[89] Erfei Bi and Joe Lutkenhaus. Ftsz ring structure associated with division in escherichia coli. *Nature*, 354(6349):161–164, November 1991. ISSN 0028-0836, 1476-4687. doi:10.1038/354161a0. URL `http://www.nature.com/articles/354161a0`.

[90] Fangwei Si, Guillaume Le Treut, John T. Sauls, Stephen Vadia, Petra Anne Levin, and Suckjoon Jun. Mechanistic Origin of Cell-Size Control and Homeostasis in Bacteria. *Current Biology*, 29(11):1760–1770.e7, June 2019. ISSN

09609822. doi:10.1016/j.cub.2019.04.062. URL https://linkinghub.elsevier.com/retrieve/pii/S0960982219304919.

[91] Bill Söderström, Alexander Badrutdinov, Helena Chan, and Ulf Skoglund. Cell shape-independent FtsZ dynamics in synthetically remodeled bacterial cells. *Nature Communications*, 9(1):4323, 2018.

[92] Jaana Männik, Bryant E Walker, and Jaan Männik. Cell cycle-dependent regulation of ftsz in escherichia coli in slow growth conditions. *Molecular Microbiology*, 110(6):1030–1044, 2018.

[93] Karthik Sekar, Roberto Rusconi, John T Sauls, Tobias Fuhrer, Elad Noor, Jen Nguyen, Vicente I Fernandez, Marieke F Buffing, Michael Berney, Suckjoon Jun, et al. Synthesis and degradation of ftsz quantitatively predict the first cell division in starved bacteria. *Molecular Systems Biology*, 14(11):e8623, 2018.

[94] Suckjoon Jun and Sattar Taheri-Araghi. Cell-size maintenance: universal strategy revealed. *Trends in Microbiology*, 23(1):4–6, January 2015. ISSN 0966842X. doi:10.1016/j.tim.2014.12.001. URL https://linkinghub.elsevier.com/retrieve/pii/S0966842X14002455.

[95] Parth Pratim Pandey and Sanjay Jain. Analytic derivation of bacterial growth laws from a simple model of intracellular chemical dynamics. *Theory in Biosciences*, 135 (3):121–130, September 2016. ISSN 1431-7613, 1611-7530. doi:10.1007/s12064-016-0227-9. URL http://link.springer.com/10.1007/s12064-016-0227-9.

[96] François Bertaux, Julius Von Kügelgen, Samuel Marguerat, and Vahid Shahrezaei. A bacterial size law revealed by a coarse-grained model of cell physiology. *bioRxiv*, page 078998, 2020.

[97] Ch E Helmstetter. Timing of synthetic activities in the cell cycle. *Escherichia coli and Salmonella: cellular and molecular biology*, 2:1627–1639, 1996.

[98] Manlu Zhu, Xiongfeng Dai, Weilun Guo, Zengxiang Ge, Mingxuan Yang, Haikuan Wang, and Yi-Ping Wang. Manipulating the Bacterial Cell Cycle and Cell Size by Titrating the Expression of Ribonucleotide Reductase. *mBio*, 8(6):mBio.01741–17, e01741–17, December 2017. ISSN 2150-7511. doi:10.1128/mBio.01741-17. URL `https://mbio.asm.org/content/8/6/e01741-17`.

[99] Benjamin Volkmer and Matthias Heinemann. Condition-dependent cell volume and concentration of escherichia coli to facilitate data conversion for systems biology modeling. *PloS one*, 6(7):e23126, 2011.

[100] Akeisha MT Belgrave and Charles W Wolgemuth. Elasticity and biochemistry of growth relate replication rate to cell length and cross-link density in rod-shaped bacteria. *Biophysical journal*, 104(12):2607–2611, 2013.

[101] Alexandre Colavin, Handuo Shi, and Kerwyn Casey Huang. Rodz modulates geometric localization of the bacterial actin mreb to regulate cell shape. *Nature communications*, 9(1):1280, 2018.

[102] Handuo Shi, Benjamin P Bratton, Zemer Gitai, and Kerwyn Casey Huang. How to build a bacterial cell: Mreb as the foreman of e. coli construction. *Cell*, 172(6): 1294–1305, 2018.

[103] Arieh Zaritsky. On dimensional determination of rod-shaped bacteria. *Journal of Theoretical Biology*, 54(2):243–248, 1975.

[104] Arieh Zaritsky. Cell-shape homeostasis in escherichia coli is driven by growth, division, and nucleoid complexity. *Biophysical Journal*, 109(2):178–181, 2015.

[105] WD Donachie, KJ Begg, and M Vicente. Cell length, cell growth and cell division. *Nature*, 264(5584):328, 1976.

[106] David W Adams and Jeff Errington. Bacterial cell division: assembly, maintenance and disassembly of the z ring. *Nature Reviews Microbiology*, 7(9):642–653, 2009.

[107] Samuel Marguerat and Jürg Bähler. Coordinating genome expression with cell size. *Trends in Genetics*, 28(11):560–565, 2012.

[108] Handuo Shi, Alexandre Colavin, Marty Bigos, Carolina Tropini, Russell D Monds, and Kerwyn Casey Huang. Deep phenotypic mapping of bacterial cytoskeletal mutants reveals physiological robustness to cell size. *Current Biology*, 27(22):3419–3429, 2017.

[109] Bill Söderström, Alexander Badrutdinov, Helena Chan, and Ulf Skoglund. Cell shape-independent ftsz dynamics in synthetically remodeled bacterial cells. *Nature Communications*, 9(1):4323, 2018.

[110] Harold P Erickson, David E Anderson, and Masaki Osawa. Ftsz in bacterial cytokinesis: cytoskeleton and force generator all in one. *Microbiol. Mol. Biol. Rev.*, 74(4):504–528, 2010.

[111] Lakshmi-Prasad Potluri, Miguel A de Pedro, and Kevin D Young. Escherichia coli low-molecular-weight penicillin-binding proteins help orient septal ftsz, and their absence leads to asymmetric cell division and branching. *Molecular Microbiology*, 84(2):203–224, 2012.

[112] Hai Zheng, Po-Yi Ho, Meiling Jiang, Bin Tang, Weirong Liu, Dengjin Li, Xuefeng Yu, Nancy E Kleckner, Ariel Amir, and Chenli Liu. Interrogating the escherichia coli cell cycle by cell dimension perturbations. *Proceedings of the National Academy of Sciences*, 113(52):15000–15005, 2016.

[113] Michaela E Sharpe, Philippe M Hauser, Robert G Sharpe, and Jeffery Errington. Bacillus subtilis cell cycle as studied by fluorescence microscopy: constancy of cell length at initiation of dna replication and evidence for active nucleoid partitioning. *Journal of bacteriology*, 180(3):547–555, 1998.

[114] Richard B Weart, Amy H Lee, An-Chun Chien, Daniel P Haeusser, Norbert S Hill,

and Petra Anne Levin. A metabolic sensor governing cell size in bacteria. *Cell*, 130 (2):335–347, 2007.

[115] Nikola Ojkic, Elin Lilja, Susana Direito, Angela Dawson, Rosalind J Allen, and Bartlomiej Waclaw. A roadblock-and-kill mechanism of action model for the dna-targeting antibiotic ciprofloxacin. *Antimicrobial Agents and Chemotherapy*, 64(9), 2020.

[116] Bella Ilkanaiv, Daniel B Kearns, Gil Ariel, and Avraham Be'er. Effect of cell aspect ratio on swarming bacteria. *Physical Review Letters*, 118(15):158002, 2017.

[117] Hannah Jeckel, Eric Jelli, Raimo Hartmann, Praveen K Singh, Rachel Mok, Jan Frederik Totz, Lucia Vidakovic, Bruno Eckhardt, Jörn Dunkel, and Knut Drescher. Learning the space-time phase diagram of bacterial swarm expansion. *Proceedings of the National Academy of Sciences*, 116(5):1489–1494, 2019.

[118] WHO. No time to wait: securing the future from drug-resistant infections, 2019.

[119] Michael A Kohanski, Daniel J Dwyer, and James J Collins. How antibiotics kill bacteria: from targets to networks. *Nature Reviews Microbiology*, 8(6):423–435, 2010.

[120] Fernando Baquero and Bruce R Levin. Proximate and ultimate causes of the bactericidal action of antibiotics. *Nature Reviews Microbiology*, pages 1–10, 2020.

[121] Jessica MA Blair, Mark A Webber, Alison J Baylay, David O Ogbolu, and Laura JV Piddock. Molecular mechanisms of antibiotic resistance. *Nature Reviews Microbiology*, 13(1):42–51, 2015.

[122] João Anes, Matthew P McCusker, Séamus Fanning, and Marta Martins. The ins and outs of rnd efflux pumps in escherichia coli. *Frontiers in microbiology*, 6:587, 2015.

[123] Sushovan Dam, Jean-Marie Pages, and Muriel Masi. Stress responses, outer membrane permeability control and antimicrobial resistance in enterobacteriaceae. *Microbiology*, 164(3):260–267, 2018.

[124] Anne H Delcour. Outer membrane permeability and antibiotic resistance. *Biochimica et Biophysica Acta (BBA)-Proteins and Proteomics*, 1794(5):808–816, 2009.

[125] Christian JH Von Wintersdorff, John Penders, Julius M Van Niekerk, Nathan D Mills, Snehali Majumder, Lieke B Van Alphen, Paul HM Savelkoul, and Petra FG Wolffs. Dissemination of antimicrobial resistance in microbial ecosystems through horizontal gene transfer. *Frontiers in microbiology*, 7:173, 2016.

[126] Jessica MA Blair, Grace E Richmond, and Laura JV Piddock. Multidrug efflux pumps in gram-negative bacteria and their role in antibiotic resistance. *Future microbiology*, 9(10):1165–1177, 2014.

[127] Abu Amar M Al Mamun, Mary-Jane Lombardo, Chandan Shee, Andreas M Lisewski, Caleb Gonzalez, Dongxu Lin, Ralf B Nehring, Claude Saint-Ruf, Janet L Gibson, Ryan L Frisch, et al. Identity and function of a large gene network underlying mutagenic repair of dna breaks. *Science*, 338(6112):1344–1348, 2012.

[128] Karen Bush and Patricia A Bradford. Interplay between $\beta$-lactamases and new $\beta$-lactamase inhibitors. *Nature Reviews Microbiology*, 17(5):295–306, 2019.

[129] Zhizhong Yao, Daniel Kahne, and Roy Kishony. Distinct single-cell morphological dynamics under beta-lactam antibiotics. *Molecular Cell*, 48(5):705–712, 2012.

[130] Leigh G Monahan, Lynne Turnbull, Sarah R Osvath, Debra Birch, Ian G Charles, and Cynthia B Whitchurch. Rapid conversion of pseudomonas aeruginosa to a spherical cell morphotype facilitates tolerance to carbapenems and penicillins but increases susceptibility to antimicrobial peptides. *Antimicrobial Agents and Chemotherapy*, 58(4):1956–1962, 2014.

[131] Katarzyna M Mickiewicz, Yoshikazu Kawai, Lauren Drage, Margarida C Gomes, Frances Davison, Robert Pickard, Judith Hall, Serge Mostowy, Phillip D Aldridge, and Jeff Errington. Possible role of l-form switching in recurrent urinary tract infection. *Nature communications*, 10(1):1–9, 2019.

[132] Shiladitya Banerjee, Klevin Lo, Nikola Ojkic, Roisin Stephens, Norbert F Scherer, and Aaron R Dinner. Mechanical feedback promotes bacterial adaptation to antibiotics. *Nature Physics*, 17(3):403–409, 2021.

[133] Anne Lamsa, Javier Lopez-Garrido, Diana Quach, Eammon P Riley, Joe Pogliano, and Kit Pogliano. Rapid inhibition profiling in bacillus subtilis to identify the mechanism of action of new antimicrobials. *ACS chemical biology*, 11(8):2222–2231, 2016.

[134] Htut Htut Htoo, Lauren Brumage, Vorrapon Chaikeeratisak, Hannah Tsunemoto, Joseph Sugie, Chanwit Tribuddharat, Joe Pogliano, and Poochit Nonejuie. Bacterial cytological profiling as a tool to study mechanisms of action of antibiotics that are active against acinetobacter baumannii. *Antimicrobial agents and chemotherapy*, 63(4), 2019.

[135] Matthew B Smith, Hongsheng Li, Tian Shen, Xiaolei Huang, Eddy Yusuf, and Dimitrios Vavylonis. Segmentation and tracking of cytoskeletal filaments using open active contours. *Cytoskeleton*, 67(11):693–705, 2010.

[136] Nikola Ojkic and Shiladitya Banerjee. Bacterial cell shape control by nutrient-dependent synthesis of cell division inhibitors. *Biophysical Journal*, 2021.

[137] Handuo Shi, Yan Hu, Pascal D Odermatt, Carlos G Gonzalez, Lichao Zhang, Joshua E Elias, Fred Chang, and Kerwyn Casey Huang. Precise regulation of the relative rates of surface area and volume synthesis in bacterial cells growing in dynamic environments. *Nature communications*, 12(1):1–13, 2021.

[138] L Pasquina-Lemonche, J Burns, RD Turner, S Kumar, R Tank, N Mullin, JS Wilson, B Chakrabarti, PA Bullough, SJ Foster, et al. The architecture of the gram-positive bacterial cell wall. *Nature*, 582(7811):294–297, 2020.

[139] Nikola Ojkic, Diana Serbanescu, and Shiladitya Banerjee. Antibiotic resistance via bacterial cell shape-shifting. *bioRxiv*, 2021.

[140] S Andreas Angermayr, Guillaume Chevereau, and Tobias Bollenbach. Growth-mediated negative feedback shapes quantitative antibiotic response. *bioRxiv*, pages 2020–12, 2021.

[141] Philip Greulich, Matthew Scott, Martin R Evans, and Rosalind J Allen. Growth-dependent bacterial susceptibility to ribosome-targeting antibiotics. *Molecular systems biology*, 11(3):796, 2015.

[142] Jacques Monod. The growth of bacterial cultures. *Annual Review of Microbiology*, 3(1):371–394, 1949.

[143] Johan Elf, Karin Nilsson, Tanel Tenson, and M\textbackslasha ans Ehrenberg. Bistable bacterial growth rate in response to antibiotics with low membrane permeability. *Physical Review Letters*, 97(25):258104, 2006.

[144] P. Greulich, M. Scott, M. R. Evans, and R. J. Allen. Growth-dependent bacterial susceptibility to ribosome-targeting antibiotics. *Molecular Systems Biology*, 11(3): 796–796, March 2015. ISSN 1744-4292. doi:10.15252/msb.20145949. URL `http://msb.embopress.org/cgi/doi/10.15252/msb.20145949`.

[145] Leigh K. Harris and Julie A. Theriot. Surface Area to Volume Ratio: A Natural Variable for Bacterial Morphogenesis. *Trends in Microbiology*, 26(10):815–832, October 2018. ISSN 0966842X. doi:10.1016/j.tim.2018.04.008. URL `https://linkinghub.elsevier.com/retrieve/pii/S0966842X18301021`.

[146] Daan H De Groot, Julia Lischke, Riccardo Muolo, Robert Planqué, Frank J Bruggeman, and Bas Teusink. The common message of constraint-based optimization approaches: overflow metabolism is caused by two growth-limiting constraints. *Cellular and Molecular Life Sciences*, 77(3):441–453, 2020.

[147] Matteo Mori, Terence Hwa, Olivier C. Martin, Andrea De Martino, and Enzo Marinari. Constrained Allocation Flux Balance Analysis. *PLOS Computational Biology*, 12(6):e1004913, June 2016. ISSN 1553-7358. doi:10.1371/journal.pcbi.1004913. URL `https://dx.plos.org/10.1371/journal.pcbi.1004913`.

[148] Markus Basan, Sheng Hui, Hiroyuki Okano, Zhongge Zhang, Yang Shen, James R. Williamson, and Terence Hwa. Overflow metabolism in Escherichia coli results from efficient proteome allocation. *Nature*, 528(7580):99–104, December 2015. ISSN 0028-0836, 1476-4687. doi:10.1038/nature15765. URL `http://www.nature.com/articles/nature15765`.

[149] Bastian Niebel, Simeon Leupold, and Matthias Heinemann. An upper limit on Gibbs energy dissipation governs cellular metabolism. *Nature Metabolism*, 1(1): 125–132, January 2019. ISSN 2522-5812. doi:10.1038/s42255-018-0006-7. URL `http://www.nature.com/articles/s42255-018-0006-7`.

[150] Tobias Bollenbach, Selwyn Quan, Remy Chait, and Roy Kishony. Nonoptimal Microbial Response to Antibiotics Underlies Suppressive Drug Interactions. *Cell*, 139(4):707–718, November 2009. ISSN 00928674. doi:10.1016/j.cell.2009.10.025. URL `https://linkinghub.elsevier.com/retrieve/pii/S0092867409013154`.

[151] Ana Rita Brochado, Anja Telzerow, Jacob Bobonis, Manuel Banzhaf, André Mateus, Joel Selkrig, Emily Huth, Stefan Bassler, Jordi Zamarreño Beas, Matylda Zietek, and others. Species-specific activity of antibacterial drug combinations. *Nature*, 559(7713):259, 2018.

[152] Guillaume Chevereau, Marta Dravecká, Tugce Batur, Aysegul Guvenek, Dilay Hazal Ayhan, Erdal Toprak, and Tobias Bollenbach. Quantifying the Determinants of Evolutionary Dynamics Leading to Drug Resistance. *PLOS Biology*, 13 (11):e1002299, November 2015. ISSN 1545-7885. doi:10.1371/journal.pbio.1002299. URL `https://dx.plos.org/10.1371/journal.pbio.1002299`.

[153] Jehangir Cama, Margaritis Voliotis, Jeremy Metz, Ashley Smith, Jari Iannucci, Ulrich F Keyser, Krasimira Tsaneva-Atanasova, and Stefano Pagliara. Single-cell microfluidics facilitates the rapid quantification of antibiotic accumulation in gram-negative bacteria. *Lab on a Chip*, 20(15):2765–2775, 2020.

[154] FN Chang and Joel G Flaks. Binding of dihydrostreptomycin to escherichia coli ribosomes: characteristics and equilibrium of the reaction. *Antimicrobial Agents and Chemotherapy*, 2(4):294–307, 1972.

[155] Kristin A Sannes-Lowery, Richard H Griffey, and Steven A Hofstadler. Measuring dissociation constants of rna and aminoglycoside antibiotics by electrospray ionization mass spectrometry. *Analytical Biochemistry*, 280(2):264–271, 2000.

[156] Arthur Abelian, Andrew P Walsh, Georg Lentzen, Fareed Aboul-Ela, and Michael J Gait. Targeting the a site rna of the escherichia coli ribosomal 30 s subunit by 2-o-methyl oligoribonucleotides: a quantitative equilibrium dialysis binding assay and differential effects of aminoglycoside antibiotics. *Biochemical Journal*, 383(2): 201–208, 2004.

[157] Shingo Suzuki, Takaaki Horinouchi, and Chikara Furusawa. Prediction of antibiotic resistance by gene expression profiles. *Nature communications*, 5(1):1–12, 2014.

[158] Henni-Karoliina Ropponen, Robert Richter, Anna KH Hirsch, and Claus-Michael Lehr. Mastering the gram-negative bacterial barrier–chemical approaches to increase bacterial bioavailability of antibiotics. *Advanced Drug Delivery Reviews*, 2021.

[159] Antoine Delhaye, Jean-François Collet, and Géraldine Laloux. Fine-tuning of the cpx envelope stress response is required for cell wall homeostasis in escherichia coli. *MBio*, 7(1), 2016.

[160] Eric Batchelor, Don Walthers, Linda J Kenney, and Mark Goulian. The escherichia coli cpxa-cpxr envelope stress response system regulates expression of the porins ompf and ompc. *Journal of bacteriology*, 187(16):5723–5731, 2005.

[161] Dijun Du, Xuan Wang-Kan, Arthur Neuberger, Hendrik W van Veen, Klaas M Pos, Laura JV Piddock, and Ben F Luisi. Multidrug efflux pumps: structure, function and regulation. *Nature Reviews Microbiology*, 16(9):523–539, 2018.

[162] Imane El Meouche and Mary J Dunlop. Heterogeneity in efflux pump expression predisposes antibiotic-resistant cells to mutation. *Science*, 362(6415):686–690, 2018.

[163] Allison J Lopatkin, Sarah C Bening, Abigail L Manson, Jonathan M Stokes, Michael A Kohanski, Ahmed H Badran, Ashlee M Earl, Nicole J Cheney, Jason H Yang, and James J Collins. Clinically relevant mutations in core metabolic genes confer antibiotic resistance. *Science*, 371(6531), 2021.

[164] Chen Hou, Wenyun Zuo, Melanie E Moses, William H Woodruff, James H Brown, and Geoffrey B West. Energy uptake and allocation during ontogeny. *science*, 322 (5902):736–739, 2008.

[165] Shiladitya Banerjee, Norbert F Scherer, and Aaron R Dinner. Shape dynamics of growing cell walls. *Soft Matter*, 12(14):3442–3450, 2016.

[166] Saman Hussain, Carl N Wivagg, Piotr Szwedziak, Felix Wong, Kaitlin Schaefer, Thierry Izoré, Lars D Renner, Matthew J Holmes, Yingjie Sun, Alexandre W Bisson-Filho, et al. Mreb filaments align along greatest principal membrane curvature to orient cell wall synthesis. *Elife*, 7:e32471, 2018.

[167] Gregory Stephanopoulos. Synthetic biology and metabolic engineering. *ACS synthetic biology*, 1(11):514–525, 2012.

[168] Gaurav Misra, Enrique R Rojas, Ajay Gopinathan, and Kerwyn Casey Huang. Mechanical consequences of cell-wall turnover in the elongation of a gram-positive bacterium. *Biophysical journal*, 104(11):2342–2352, 2013.

[169] Matteo Mori, Severin Schink, David W Erickson, Ulrich Gerland, and Terence Hwa. Quantifying the benefit of a proteome reserve in fluctuating environments. *Nature communications*, 8(1):1–8, 2017.

[170] Enrique Rojas, Julie A Theriot, and Kerwyn Casey Huang. Response of escherichia coli growth rate to osmotic shock. *Proceedings of the National Academy of Sciences*, 111(21):7807–7812, 2014.

[171] Pradeep Kumar and Albert Libchaber. Pressure and temperature dependence of growth and morphology of escherichia coli: experiments and stochastic model. *Biophysical journal*, 105(3):783–793, 2013.

[172] Fangwei Si, Bo Li, William Margolin, and Sean X Sun. Bacterial growth and form under mechanical compression. *Scientific reports*, 5(1):1–11, 2015.

[173] Wei-Hsiang Lin and Christine Jacobs-Wagner. Connecting single-cell atp dynamics to overflow metabolism, cell growth and the cell cycle in escherichia coli. *Cell Growth and the Cell Cycle in Escherichia coli*.

[174] François Bertaux, Julius Von Kügelgen, Samuel Marguerat, and Vahid Shahrezaei. A bacterial size law revealed by a coarse-grained model of cell physiology. *PLoS computational biology*, 16(9):e1008245, 2020.

[175] Markus Basan, Tomoya Honda, Dimitris Christodoulou, Manuel Hörl, Yu-Fang Chang, Emanuele Leoncini, Avik Mukherjee, Hiroyuki Okano, Brian R Taylor,

Josh M Silverman, et al. A universal trade-off between growth and lag in fluctuating environments. *Nature*, 584(7821):470–474, 2020.

[176] Somenath Bakshi, Emanuele Leoncini, Charles Baker, Silvia J Cañas-Duarte, Burak Okumus, and Johan Paulsson. Tracking bacterial lineages in complex and dynamic environments with applications for growth control and persistence. *Nature Microbiology*, 6(6):783–791, 2021.

[177] Jen Nguyen, Vicente Fernandez, Sammy Pontrelli, Uwe Sauer, Martin Ackermann, and Roman Stocker. A distinct growth physiology enhances bacterial growth under rapid nutrient fluctuations. *BioRxiv*, 2020.